# Biomimetic Electrospun Fibers for Peripheral Nervous System Repair

by

Michelle K. Leach

A dissertation submitted in partial fulfillment
of the requirements for the degree of
Doctor of Philosophy
(Biomedical Engineering)
in the University of Michigan
2013

Doctoral Committee:

Assistant Professor Joseph M. Corey, Chair
Associate Professor R. Keith Duncan
Associate Professor Andrew J. Putnam
Associate Professor Jan P. Stegemann

Dedication

To my parents, who nurtured and encouraged my education from the beginning.

Acknowledgements

This dissertation would not have been possible without the help of many of my colleagues and collaborators. I would especially like to thank my advisor, Dr. Joseph Corey, for his mentorship and support; Dr. Duncan, Dr. Putnam, and Dr. Stegemann for their service and insight as committee members; Dr. Lynda Yang for her helpful collaboration, and Dr. Zhangqi Feng for his mentorship. I would also like to thank the staff at the VA and the University of Michigan who facilitated this research, including Sherry Wagar, Len Cooke, Chris Edwards, and Judy Poore.

I would like to acknowledge the many undergraduate students who have worked in the Nanoscale Neurology lab. It has been a pleasure watching you grow into researchers. I would especially like to thank Tara Regan, Samuel Tuck, Eric Franz, and Joel Goodman, whose help in carrying out these experiments has been invaluable. Other students who assisted over the years and to whom I am indebted include Arjun Rastogi, Shayaan Khanna, Amber Chacon-Saavedra, Brian Kulick, Spencer Ferris, Matthias Kirsch, and Matt Johnson. I would like to acknowledge the Undergraduate Research Opportunity Program for supporting these students.

I would also like to thank my husband, Youssef Naim, for his support and encouragement during this time. Finally, I am grateful to all my friends and family for their love and support during my graduate experience.

Table of Contents

List of figures

List of tables

Abstract

Endogenous peripheral nerve regeneration is a slow and error-prone process, and injury to the peripheral nervous system is a significant cause of permanent disability. One promising approach to improving these outcomes is the use of artificial nerve conduits. The primary goal of this dissertation was to develop an artificial nerve conduit that outperformed the current gold standard, the autograft. The design approach was to mimic the internal microenvironment of native nerve physically and chemically, using aligned electrospun fibers modified with polypeptides to accelerate growth of regenerating neurites. In order to evaluate this candidate material however, it was necessary to develop a sufficiently rigorous *in vitro* system to partially predict how nanofibers could influence regenerating neurons *in vivo.* Three steps to this system process include electrospinning nanofibers, culturing neurons nanofibers, and assessing neuronal behavior, the first and third of which remained inefficient and irreproducible. Critical variables of electrospinning poly-L-lactide (PLLA) nanofibers were systematically investigated. A protocol to electrospin highly aligned nanofibers reproducibly was developed. We found that the distance between the spinneret tip and collector, decreasing solvent volatility, and concentrating the electric field with an aluminum sheet on the spinneret greatly improved density and alignment of electrospun nanofibers. To quantify the developmental response of neurons to nanofiber topography, a process was developed to analyze microscopic images of neurons using

MetaMorph software and a custom-designed algorithm developed in MATLAB. The system was verified against analysis by hand and increased the speed of morphological analysis of neurons from 2 weeks to less than a day, roughly 90%. The peptide fragment IKVAV, when bound to nanofibers, was found to increase the speed of neurite growth *in vitro* compared to unbound nanofibers. As a result, IKVAV-bound nanofibers were incorporated into conduits and implanted into a gap in the sciatic nerve of Lewis rats. IKVAV-modified fibers supported regeneration, producing detectable nerve conduction after only six weeks of implantation, but underperformed autografts. Together, these results show that electrospun fibers can be reproducibly aligned, covalently bound, and used to promote peripheral nerve regeneration *in vivo*.

# Chapter 1. Background and overview

## 1.1 Executive Summary

Endogenous neural regeneration is a slow and error-prone process. As a result, injury to the peripheral nervous system is a significant cause of morbidity and permanent disability. Currently, the standard and most common clinical treatment is direct surgical repair of the damaged nerve ends or, in cases where an injured section of nerve must be replaced, an autologous nerve graft. Even under optimal repair conditions, severely injured nerves rarely reach complete functional recovery. Additionally, there is a shortage of available nerve for autologous repair. One promising approach to improving these outcomes is the use of artificial nerve conduits. These constructs can serve as scaffolds to guide and enhance neural regeneration. Additionally, scaffolds may be chemically, physically, or biologically modified to further enhance nerve growth. Artificial nerve conduits can also be manufactured at any length to accommodate the full range of possible injuries.

The primary goal of this dissertation was to develop an artificial nerve conduit that outperformed the current gold standard – the autograft. The design approach was to mimic the internal microenvironment of native nerve physically and chemically. This approach was based on the fact that regenerating neurites are heavily dependent on physical and chemical cues presented by the nerve structure for direction. In fact, the

nerve injuries most likely to recover are those where the structure of the nerve has not been damaged, as in the case of crush or purely ischemic injuries. The main hypothesis is that conduits which more closely mimic native nerve will support the most regeneration.

In order to evaluate candidate materials for the artificial nerve conduit, it was necessary to develop a system with which to investigate peripheral nerve regeneration *in vitro*. Electrospun nanofibers have been repeatedly shown to support and direct the outgrowth of neurites *in vitro*. Therefore, electrospun fibers were chosen as the platform on which to develop the conduit and experimental system. The system was verified and used to select candidate materials for further study *in vivo*. The results to date of this *in vivo* work are presented, along with recommendations for further research.

Experimental system development

*In vivo*, the nanotopography of peripheral nerve is extremely aligned, with axon tracts running in parallel to one another. In order to replicate this environment, it was essential to maximize the extent of nanofiber alignment. Electrospinning produces nanofibers through an inherently unstable process. It is the whipping motion of the polymer stream which creates the small fiber diameter. This whipping motion unfortunately makes orderly fiber collection a challenge. To optimize fiber alignment, a thorough investigation of several parameters of the electrospinning process, including solution composition, spinneret-to-collector distance, and plate-to-spinneret distance, was conducted. The results were analyzed to develop an electrospinning protocol which reproducibly results in highly aligned fiber bundles.

Primary motor neurons from rat E15 embryos were selected as the cell type for the *in vitro* system because these cells most closely mimic the cells of peripheral nerve *in vivo*. Culture was carried out in a defined, serum-free media to eliminate variables introduced by inconsistencies in normal serum composition. Glial cells were excluded from the motor neuron culture to mimic the Schwann cell depleted environment characteristic of Wallerian degeneration *in vivo*. A low density culture was chosen both for ease of data analysis and to mimic the neuron-free territory regenerating neurites encounter *in vivo*. An automated technique to characterize cell morphology was also developed that minimized the time needed to complete meaningful data analysis.

Experimental system verification

The suitability of any experimental system must be validated prior to using the model to conduct experiments. We defined a valid system as one which supported the normal outgrowth and maturation of neuronal cells. The behavior of primary neurons, as well as glia, was characterized when cultured in defined media on the highly aligned electrospun fibers. These cell types were found to mature and migrate according to patterns observed *in vivo* and in prior *in vitro* studies. Thus, the system was considered a high-quality model of the natural environment. Additionally, the automated detection and analysis of neuronal morphology was validated by comparing the results to a manual hand count of the same data.

*In vitro* evaluation of candidate materials and *in vivo* results to date

Candidate scaffolds were tested using the developed *in vitro* system and method of analysis to select suitable materials for *in vivo* testing. The most promising was selected for further evaluation *in vivo*. The peptide sequence IKVAV is a laminin binding domain known to induce neurite outgrowth. Electrospun fibers covalently modified with IKVAV supported the longest outgrowth of neurites *in vitro* of all the materials tested. Therefore, several sheets of IKVAV-bound fibers were stacked in a polysulfone tube conduit and implanted across a 1.2 cm gap in rat sciatic nerve. An autograft served as the positive control and an empty conduit and a conduit with unmodified fibers served as negative controls. At six weeks, regeneration was evaluated by nerve conduction velocity measurements. The conduits were then explanted and analyzed by standard histological methods.

Results and conclusion

The system of experimental investigation was determined to be a good *in vitro* model with which to evaluate candidate materials for artificial nerve conduits. Partial regeneration through the conduit with IKVAV-bound fibers was evident at six weeks and a preliminary nerve conduction velocity was recorded. Histological investigation revealed numerous axons present in the conduit, migrating parallel to the fibers. A nerve conduction velocity was observed on two autograft control animals, as were a large number of axons. Neither the unbound fibers nor the empty conduit supported any regeneration, resulting only in fibrous scar tissue and granulation tissue, respectively. Longer duration *in vivo* experiments are currently underway.

While the IKVAV-bound fibers supported some regeneration, the number of regenerating axons was far lower than those in the autograft across a gap of the same size. However, the IKVAV-fibers vastly out-performed the non-bound fibers. So there may be some application for IKVAV-bound fiber nerve conduits in situations where there is insufficient donor nerve available for an autograft, as is the case with large gaps.

## 1.2 Peripheral nerve injury

### 1.2.1 Incidence and prognosis

Injury to a peripheral nerve is common and devastating; a survey found the incidence of major nerve injury to be 2-3% of those patients admitted with multiple traumas [1]. Regeneration occurs over weeks to years and is often incomplete (axons do not reach targets) or aberrant (axons reach the wrong targets) [2]. Failed regeneration is defined as partial or complete loss of motor function and/or sensation. It is difficult to predict the regeneration outcome immediately following injury, but it is generally held that complete transection is more serious than partial transection [3] or crush injuries and that the likelihood of recovery is decreased when the injury site is proximal rather than distal [4].

### 1.2.2 Regeneration

Following injury, neurons in the peripheral nervous system (PNS) begin to regenerate axons. Different processes occur in the proximal and distal stumps of the injured nerve. Immediately following injury the severed axons in the proximal stump die back to at least the first node of Ranvier [5]. However, dieback may continue as far back

as the cell body itself – in the case of the leg, this distance can exceed 1 m [5]. In the distal stump, a process known as Wallerian degeneration occurs. In this process, the distal ends of the severed axons begin to lose cytoskeletal and membrane integrity. Schwann cells (SC) begin to break down the axonal debris as well as secrete chemoattractants to draw macrophages from the circulation into the injury site; the macrophages then break down myelin components and other debris, including the distal remains of the severed axons [6]. Meanwhile, in the proximal stump, the severed axons sprout and begin to lengthen and migrate distally. This migration is very slow, approximately 1 mm/day [7]. SC in the distal stump subsequently proliferate and begin secreting growth factors, such as GDNF [8], BDNF [9] and NGF [10], and express adhesion molecules, including laminin, the neu receptors[11] and the low-affinity nerve growth factor receptor p75 [10, 12]. The SC, having proliferated, align to form microscopic conduits resembling bands when viewed with a light microscope. These bands of Büngner form along the length of the distal stump. The growth cones of the regenerating axons eventually encounter these aligned bands of SC and then follow them closely as they continue to migrate towards their targets [13].

### 1.2.3 Surgical intervention

Peripheral nerve injuries require surgical intervention when there is a loss of continuity (as in transection) or when the endoneurial tubes have been completely destroyed (as in extreme or prolonged crush [14]). Transected nerves must be sutured together by the surgeon [15]. A nerve graft must be used in cases where a section of nerve is missing or destroyed. When the gap is large enough that the nerve stumps cannot be approximated to close the gap without putting tension on the nerve, an

alternative is needed, as the increased tension would strangulate the nerve [16]. A variety of approaches are typically used by surgeons to bridge the gap.

One approach is for the surgeon to perform an autograft by bridging the gap with a portion of sensory nerve. Usually, a pure sensory nerve is used, such as the sural nerve from the patient's foot [17]. This approach is limited by the size (diameter) and amount of donor nerve (length) available. It also unavoidably results in a loss of sensation in one or both feet, which is undesirable and may become painful [17]. Additionally, donor segments are only taken from sensory nerves (as loss of sensation is preferable to loss of movement). This complicates the repair of motor or mixed motor/sensory nerves, because the SC in sensory nerves and the growth factors they secrete differ from those in motor nerves [18]. Thus, sensory neurons tend to regenerate more successfully through autografts than motor neurons.

An alternative approach is for the surgeon to perform an allograft, bridging the gap with a section of cadaver nerve [15]. Cadaveric allografts offer the advantage in that they can be selected to solve the problems of insufficient diameter and length, a significant limitation of autografts. Additionally, when decellularized, cadaver grafts do not require immunosuppression like other allografts. These properties make such grafts very desirable, leading to their becoming more widely used. However, since they lack SC and growth factors, cadaveric allografts continue to underperform autografts [19]. The remaining alternative is the use of an artificial graft.

### 1.2.4 Gap lengths in real clinical situations

In considering desirable design parameters for artificial grafts, it becomes very important to think of the lengths of gaps that need to be spanned clinically. While most research in nerve regeneration centers on crossing gaps that are 1, 1.5, 1.8, or 2 cm in length in experimental rodent models, many surgeons frequently deal with much longer gaps in the operating room. One such set of clinical data arises from nerve gaps in the head that otolaryngologists (ear, nose, and throat specialists) must address in the operating room. Conversations between our lab and physicians in the Department of Otolaryngology at the University of Michigan illustrate this significant challenge. For example, facial nerve repairs can have gaps as short as 2 cm, but may be as long as 8 cm [20, 21]. Gaps used to repair the accessory or hypoglossal nerves after tumor resection can be 6 to 12 cm long [20]. For major temporal bone lesions, lengths of grafts may range from 10 to 15 cm [22], and nerve reconstruction following parotid tumor removal may need even longer grafts. This precludes the use of autografts, as insufficient donor material is available [22]. These data suggest that nerve guides used in actual clinical applications need to be capable of promoting neurite growth over very long distances.

### 1.2.5 Artificial nerve conduits

Artificial nerve conduits generally take the form of a flexible tube used to bridge the two ends of a severed nerve. They can be composed of biological and/or synthetic materials. Common biologically-derived materials include arterial [23] or venous [24] segments or muscle tissue [25]. Synthetic conduits composed of simple silicone tubing

have been investigated extensively [26, 27]. The use of silicone and other non-resorbable materials has been replaced by the use of synthetic biodegradable polymers such as poly-lactic acid (PLLA) [28], poly-glycolic acid (PLGA) [29] and poly-caprolactone (PCL) [30]. Toward making the conduits resemble the extracellular microenvironment of neurons, the lumens of artificial nerve conduits have been filled with saline [27], collagen [31] and other extracellular matrix components, such as collagen, fibronectin and laminin [32]. However, all these variations still underperform the autograft.

The conduits that perform most similarly to autografts are those which have been pre-loaded with SC prior to implantation [33, 34]. Despite their robust performance, a SC loaded conduit is not feasible for clinical use in humans. Growing up a sufficient number of autologous SC would take several weeks, delaying surgical repair, and the use of donor SC would require immunosuppression, the of which generally outweigh the benefits [35].

Since the use of SC is essentially precluded for the reasons above, recent designs of artificial nerve conduits have been devised to contain components that resemble the optimal extracellular microenviroment of regenerating axons in peripheral nerve. Hydrogels [36] can include Schwann cells, growth factors, and ECM proteins [37-41]. Collagen [40], chitosan [42], and agarose [43] are all examples of hydrogels studied for neural tissue engineering. Polymer fibers and foam scaffolds have also been investigated [44]. Artificial polymers are increasingly finding their way into implanted medical devices due to their excellent biocompatibility, strength, and tailored degradability.

### 1.2.6 Nanotopographical features in nerve guidance conduits

A relatively recent component included in nerve guidance conduits are nano- and microtopographical features. Numerous studies have demonstrated the ability of topographical features to direct the outgrowth of regenerating neurites [28, 45-48]. Common nanotopographical features include aligned electrospun polymer filaments [28, 45, 49], fibrillar extracellular matrix components [50] and nano-oriented hydrogels [51]. The inclusion of nanotopographical guidance in conduits is particularly relevant when the role of SC in regeneration is considered. Schwann cells guide regenerating neurites by providing chemical signals, as discussed above, but also topographically, through the formation of the bands of Büngner. In the evolution of nerve conduit design, the chemical guidance cues provided by Schwann cells have been replaced by adding growth factors and other proteins to the conduit. By additionally including nanotopographical features, the role of SC in regeneration can be further simulated.

Electrospun nanofibers have been repeatedly shown to support and direct the outgrowth of neurites *in vitro*. Previous work in our laboratory showed that rat dorsal root ganglia and motor neurons extend neurites that follow the alignment of PLLA electrospun fibers [28, 45]. Others have shown this to be true of chick dorsal root ganglia neurons on PLLA fibers as well [48]. Composite electrospun fibers composed of polycaprolactone and gelatin enhanced the differentiation of nerve stem cells [52]. Bellamkonda reported the successful bridging of a 17 mm gap in rats using electrospun fibers [47]. These are promising indications that electrospun fibers have a place in nerve conduits designed to bridge larger gaps. Therefore, electrospun fibers were chosen as the platform on which to develop our conduit and experimental system.

## 1.3 Electrospinning

### 1.3.1 Electrospinning technique

Electrospinning is a process in which a charged polymer jet is collected on a grounded collector; a rapidly rotating collector results in aligned nanofibers while stationary collectors result in randomly oriented fiber mats. The polymer jet is formed when an applied electrostatic charge overcomes the surface tension of the solution. There is a minimum concentration for a given polymer, termed the critical entanglement concentration, below which a stable jet cannot be achieved and no nanofibers will form - although nanoparticles may be achieved (electrospray). An electrospinning jet has two domains, a streaming segment and a whipping segment. While the whipping segment is usually invisible to the naked eye, the streaming segment is often visible under appropriate lighting conditions. Observing the length, thickness, consistency and movement of the stream is useful to predict the alignment and morphology of the nanofibers being formed. A short, non-uniform, inconsistent, and/or oscillating stream is indicative of a variety of problems, including poor fiber alignment, beading, splattering, and curlicue or wavy patterns. The stream can be optimized by adjusting the composition of the solution and the configuration of the electrospinning apparatus. While significant research has been dedicated to determining the process parameters which produce fibers with a uniform cross-section, little effort has been made towards obtaining highly aligned bundles of fibers consistently and reproducibly. In Chapter 2, a detailed study of critical variables, resulting in a process for reproducibly obtaining highly aligned poly-L-lactic acid (PLLA) fibers is presented.

### 1.3.2 Electrospun fiber applications

Electrospun fibers have a multitude of applications in biomedical research. Electrospun fibers have been shown to orient a wide range of cell types, including chondrocytes [53], fibroblasts [54], muscle [55], endothelium [56] and osteoblasts [57]. Recently, electrospun fibers have been shown to improve the differentiation of stem cells to neurons when combined with a genetic program [58]. This effect has also been observed with osteogenic differentiation of mesenchymal stem cells [59]. Interestingly, fiber diameter has also been shown to influence which lineage embryonic stem cells differentiate towards in the absence of any applied morphogens [60] and oligodendrocyte precursors will differentiate and began to wrap electrospun fibers with diameters that resemble those of axons [61]. Electrospun fiber mats are also being investigated for use as drug eluting materials and wound dressings [62]. New applications for electrospun fibers continue to be investigated.

Why are electrospun fibers so widely used? The versatility of electrospinning is the key. Any medium to high molecular weight polymer can be electrospun, and low molecular weight polymers or even non-polymer substances can be electrospun through the use of a small amount of carrier polymer. Natural or synthetic, water soluble or not, the material possibilities are endless. This allows researchers to tailor the fibers to their own particular research needs. The morphology of the fiber is also malleable. Many diameters, porosities, surface textures and densities are possible. The fibers are also easy to modify with surface ligands. In short, electrospinning allows a high degree of control using economical equipment.

## 1.4 Extracellular matrix proteins

The extracellular matrix (ECM), an organized network of fibrils formed through polymerization of glycoproteins, is critical for cell function, tissue architecture, and tissue remodeling during development or after injury [63, 64]. During nervous system development, numerous ECM molecules are present, including laminin, fibronectin, vitronectin, collagens, proteoglycans, tenascin, agrin, and thrombospondin [64]. Laminin in particular is important for neurite outgrowth, and several unique laminin isoforms are expressed only in neuronal tissues [65]. Laminin, produced in part by Schwann cells, is a constituent of the basal lamina in peripheral nerve [66]. Schwann cell production of laminin is increased dramatically distal to an injury [67]. Laminin (and other ECM proteins) contain peptide sequences, or domains, that bind to integrins, cell surface receptors on neurons that help to control cell signaling and behavior. Laminin contains numerous binding domains, including IKVAV [68] and LQVQLSIR [69] that promote neurite growth directly, as well as YIGSR and RGD that promote cell attachment [70]. IKVAV alone can mimic the ability of laminin to promote neurite outgrowth [71]. Both motor neurons [72] and dorsal root ganglia (DRG) sensory neurons [73] adhere and extend neurites on laminin.

Laminin is a potent stimulator of neurite outgrowth [74] possessing several integrin binding domains that stimulate neurite growth, including the peptide sequence IKVAV [65]. Indeed, laminin promotes outgrowth of motor neurons and results in longer neurite growth on aligned electrospun nanofibers. However, laminin that is merely coated on nanofiber scaffolds will likely desorb from the fibers following implantation.

Individual peptide sequences covalently bound to the fiber surface may prevent desorption and limit cleaving by native proteases.

## 1.5 *In vitro* systems of evaluation

Despite over 30 years of investigation of artificial nerve conduits, no standard experimental system exists with which to evaluate candidate materials for inclusion in their design and construction. Considerations for doing so are described below.

### 1.5.1 Cell type

A variety of culture systems have been used to evaluate candidate materials *in vitro*. Tumor-derived cell lines of human (e.g., SH-SY5Y) or animal (e.g., PC12) origin are frequently used to evaluate cell interactions with candidate materials [32, 75, 76]. However, while transformed cell lines are easy to manipulate, these cell lines are increasingly being shown to not respond in the same manner as primary cells [77, 78]. Neuroblastoma cells extend neurites which do not resemble true axons or dendrites either morphologically or immunohistochemically [79]. These cells also adhere to surfaces in the absence of the surface coatings normally required by primary neurons for attachment [45, 80]. Therefore, the utility of employing these cell lines to predict the results of regeneration *in vivo* is limited, because these differences make transformed neuroblasts non-predictive of real neurons. Therefore, the use of primary neurons to evaluate nerve conduits *in vitro* is much more relevant for this type of work [28]. Indeed, many have used dorsal root ganglia sensory neurons *in vitro* [45, 47, 48]. However, the use of primary motor neurons is uncommon [81, 82]. Since peripheral nerves may be composed of sensory neurons, motor neurons or both, *in vitro* testing of proposed

guidance channel components with both DRG and motor neurons should be more predictive of behavior *in vivo*.

### 1.5.2 Culture media

The selection of an appropriate culture media and additives is extremely important to maximize normal cell behavior *in vitro*. For example, while adding serum to media to supply it with cell-sustaining trophic factors is convenient, it has long been known that variability exists between batches of commercially available serums, as a great number of unknown growth factors [83, 84] and/or contaminants may be present [85]. Additionally, serum can be toxic to neurons, requiring neuron culture at higher density to ensure autotrophic support, and therefore limiting the ability of the investigator to study the effects of the materials on individual neurons, which requires low-density culture [86]. The use of a defined, serum-free media is preferred to reduce experimental variability and to ensure consistency of cellular behavior. Specifically, Neurobasal (Invitrogen) and b27 (Gibco) have become the standard media system for the culture of low density primary neurons [86, 87]. The *in vitro* experiments described in the chapters to follow were all conducted using serum-free media and primary cells.

### 1.5.3 Method of analysis

A variety of methods exist in the literature by which to describe the growth of neurons *in vitro*. In the case of transformed cells, there may be simply a notation that the cells ‘were differentiated’, indicating that neurites were present, with little attempts at further description. Others may define a neurite as a process with some minimum length, or choose to instead focus on the major (longest) neurite, which is often

declared ‘the axon’ regardless of any other indication that it is such. In order to facilitate comparison of results between studies, it would be beneficial for researchers to adopt a standard method of quantifying neuronal growth.

Following plating *in vitro*, neurons pass through a series of morphological stages as they adhere and mature, which were first described by Dotti and colleagues [88]. It has since been shown that other neuronal cell types, including motor neurons [81], pass through these stages as well [89]. These morphological stage transitions can be monitored as a function of time to evaluate the relative health and development of neuronal cultures under different conditions. This type of measurement is easily compared across studies, and is recommended for adoption by other researchers.

While morphological development is usually quite obvious to the experienced eye, it can often be difficult to quantify in a meaningful way. Morphology quantification typically relies on manual image measurement and can therefore be tedious, time consuming and prone to human error. In Chapter 1, the development of an automated process using the image analysis program MetaMorph® to quantify the morphological growth of motor neurons *in vitro* is described. When properly configured, automated image analysis with MetaMorph® is a rapid and reliable alternative to manual measurement and has the potential to accelerate the research process.

## 1.6 Dissertation outline

Previous work in our laboratory has explored primary cell culture on electrospun fibers. Dorsal root ganglia were cultured on electrospun fibers in 2007 and the DRG neurites were shown to follow the direction of fiber alignment [45]. In 2008, our

laboratory was the first to successfully culture primary motor neurons on electrospun fibers [28]. The motor neurons extended neurites in the direction of fiber alignment. In 2010, we discovered that motor neurons not only follow the direction of fiber alignment, but mature sooner on electrospun fibers than on flat glass [81].

However, further timely research was hindered due to our difficulty electrospinning and the tedious method of analysis available to us. Several critical variables of electrospinning were investigated until a protocol to reliably electrospin highly aligned fibers reproducibly was developed. The results of this study are presented in Chapter 2, which was published in Materials and Engineering Part C in 2012 [90]. Furthermore, Chapter 3 describes an automated method of analysis that reduces the time required to obtain quantitative morphological data. Chapter 4 was published in the Journal of Neuroscience Methods in 2011 [91]. Once methods for high-throughput electrospinning of aligned fibers and morphological neuron analysis were developed, we had an experimental system in place which could rapidly evaluate candidate nerve conduit materials and configurations.

Before diving into conduit development, we felt it was important to further validate the use of electrospun fibers in nerve guidance conduits. We had already shown that dorsal root ganglia responded favorably to electrospun fibers by extending neurites in the direction of fiber alignment. But dorsal root ganglia contain Schwann cells which provide many regeneration promoting signals. How would electrospun fibers perform in an environment with reduced Schwann cells? The results from this rigorous test of electrospun fibers further supported our use of electrospun fibers for nerve regeneration

and are presented in Chapter 4. This chapter is currently in press at Minerva Biotechnologica.

In Chapter 5, our newly devised *in vitro* experimental system was taken through a complete design cycle. Three candidate materials were considered. Electrospun PLLA fibers were coated with laminin, blended with laminin or covalently modified with a laminin peptide (IKVAV) and evaluated *in vitro*. The fibers which supported the most robust neurite growth (IKVAV-modified fibers) were selected for further evaluation in a small animal model of peripheral nerve injury. Results to date of this *in vivo* experiment are presented in Chapter 6. Chapter 7 follows with conclusions and recommendations for future research.

# Chapter 2. Critical variables in the alignment of electrospun PLLA nanofibers [90]

Electrospun polymer nanofibers show promise as components of scaffolds for tissue engineering because of their ability to orient regenerating cells. Our research focuses on aligned electrospun fiber scaffolds for nerve regeneration. Critical to this are highly aligned fibers, which are frequently difficult to manufacture reproducibly. Here we show that three variables: the distance between the spinneret tip and collector, the addition of DMF to the solvent, and placement of an aluminum sheet on the spinneret together greatly improve the alignment of electrospun poly-L-lactide (PLLA) nanofibers. We identified the most important variable as tip-to-collector distance. Nanofiber alignment was maximal at 30 cm compared to shorter distances. A solvent composition of DMF:chloroform (1:9 v/v) improved nanofiber uniformity and was integral to maintaining a uniform stream over the 30 cm tip-to-collector distance. Other ratios caused splattering of the solution or flattening or beading of the fibers and non-uniform fiber diameter. The aluminum sheet helped to stabilize the electric field and improve fiber alignment provided that it was placed at 1 cm behind the tip, while other distances destabilized the stream and worsened alignment. This study demonstrates that control of these variables produces dramatic improvement in reproducibly obtaining high alignment and uniform morphology of electrospun PLLA nanofibers, which are crucial characteristics of electrospun fibers destined for use in peripheral nerve regeneration conduits.

## 2.1 Introduction

Because cells orient along physical cues on the cell-length scale, aligned electrospun fibers can be incorporated in tissue engineering applications where the orientation of cells is desired. Electrospun fibers have been incorporated into scaffolds designed to engineer the tissues that constitute a variety of organs, including bone [92], heart [93], muscle [94], and nerve [28, 45, 47]. Not only do electrospun fibers orient cells, but they have also been shown to contribute to their differentiation, such as in the case of stem cells [95, 96]. Morphologically, electrospun fibers mimic the fibrillar components of the extracellular matrix that underlie cells and support their proliferation and differentiation into tissues. In nerve regeneration applications, where directing neurites is critical to success, the extent of nanofiber alignment in scaffolds may profoundly affect the targeting and speed of regenerating neurites, and therefore the effectiveness of nerve regeneration [28, 45, 48].

Electrospinning is a straightforward procedure used to create micro- or nanoscale fibers from polymer materials. Many polymers, including poly-L-lactic acid (PLLA) [28, 45, 97], polycaprolactone (PCL) [98], polystyrene (PS) [99], or nylon [95, 100] have been electrospun. Common to all electrospinning is the dissolution of a polymer in a volatile solvent that is then loaded in a syringe, which is placed on a pump set at a constant feed rate. A voltage is directly applied to the syringe by a clamp, charged plate, or ring(s) [101, 102] and slowly increased until a steady stream of polymer is obtained between the tip of the syringe and the collector. In recent years, various types of collectors have been used, selected on the basis of the desired orientation of the fibers. For randomly-oriented fibers, the collector is typically a flat,

stationary conductive plate. For uniaxially-aligned fibers, a variety of collectors have been used, including rotating drums or wheels, or parallel plates [98, 100, 103, 104]. Collectors are grounded to facilitate the attraction of the charged stream.

Despite its widespread use as a means for creating fibers, controlling the electrospinning process to orient fibers reproducibly has been difficult. Alignment and fiber morphology can be influenced by controlling rotational velocity of the collector [48], magnitude of the applied voltage [100, 103, 105], the distance between spinneret and collector [97, 106-109], collector geometry [97, 100], solution composition[110], electrostatic repulsion [100] and various modifications to the spinneret [101, 102]. Factors observed to negatively affect fiber uniformity and alignment include wagging and sputtering of the stream [111] and high ambient humidity [112]. High alignment was also observed by adjusting the electric field [106]. It has also been shown that the gauge of the spinneret needle, whether this tip is sharp or blunt or insulated versus non-insulated have a powerful effect on alignment [48].

Beginning with parameters used in our previous studies [28, 45], we altered some of the parameters and found improved fiber alignment and shape. We discovered that increasing the tip-to-collector distance from 5 cm to 30 cm, along with increasing the voltage, dramatically increased alignment of fibers. In an effort to make the electrical field between the spinneret and the collector more uniform, we mounted a square sheet of aluminum on the spinneret needle. Placing this approximately 1 cm behind the tip of the spinneret helped to maximize alignment. Additionally, we found that making the solution less volatile by adding dimethylformamide (DMF) at 10% (v/v) to our standard chloroform solvent also increased uniformity of fiber diameter as well as

alignment. Together, these changes have had a dramatic impact on our ability to produce highly aligned PLLA nanofibers in a reproducible manner.

## 2.2 Methods and materials

The electrospinning apparatus was configured to obtain highly aligned and uniform uniaxial patterned nanofibers. A grounded rotating disc with a diameter of 25.4 cm and a 0.159 cm wide beveled edge was constructed at The University of Michigan (Ann Arbor, MI) and modified by MogulTech (Saline, MI). Five glass cover slips with a diameter of 1.25 cm (Daigger, Vernon Hills, IL) were coated with a thin film of poly-lactic-glycolic acid (PLGA) and taped at even intervals around the beveled edge of the wheel with carbon tape (Electron Microscopy Sciences, Hatfield, PA) for each electrospinning run. The disc collector was rotated at a linear velocity of 8 m/s (600 RPM) by a high torque industrial stirring motor (Caframo Ltd., Wiarton, Ontario, Canada). A wire brush biased at -2 kV was applied to the disc collector.

PLLA (Boehringer Ingelheim, Ridgefield, CT) was dissolved at 4% (w/v) in chloroform:DMF at a ratio of 90:10 (v/v). A 23 gauge blunt needle (Nordson EFD, Westlake, OH) was used to dispense the PLLA solution from a 3 ml polypropylene syringe with an inner diameter of 5 mm (BD, Franklin Lakes, NJ). The tip of the spinneret (blunt needle) was poked through the center of a 10 x 10 cm sheet of aluminum foil. An electrical potential was applied to the spinneret from a high voltage DC power supply, the magnitude of which depended on specific conditions (see below), by directly clamping an alligator clip to the base of the aluminum sheet. Thus the needle was biased through contact with the aluminum sheet. This arrangement avoided

the deleterious effects on the alignment due to variations in the electric field produced by the multiple angled surfaces of the alligator clip. The polymer solution was delivered by a KDS 100 (KD Scientific, Holliston, MA) syringe pump positioned at various distances from the collector and set at a fixed dispensing rate of 0.6 ml/hr. The three critical variables (tip-to-collector distance [Figure 2.1(A)], tip-to-sheet distance [Figure 2.1(B)], and solvent volatility) were adjusted to produce highly aligned and uniform nanofibers. As these parameters were varied, the magnitude of the voltage was adjusted to produce a steady stream at each configuration.

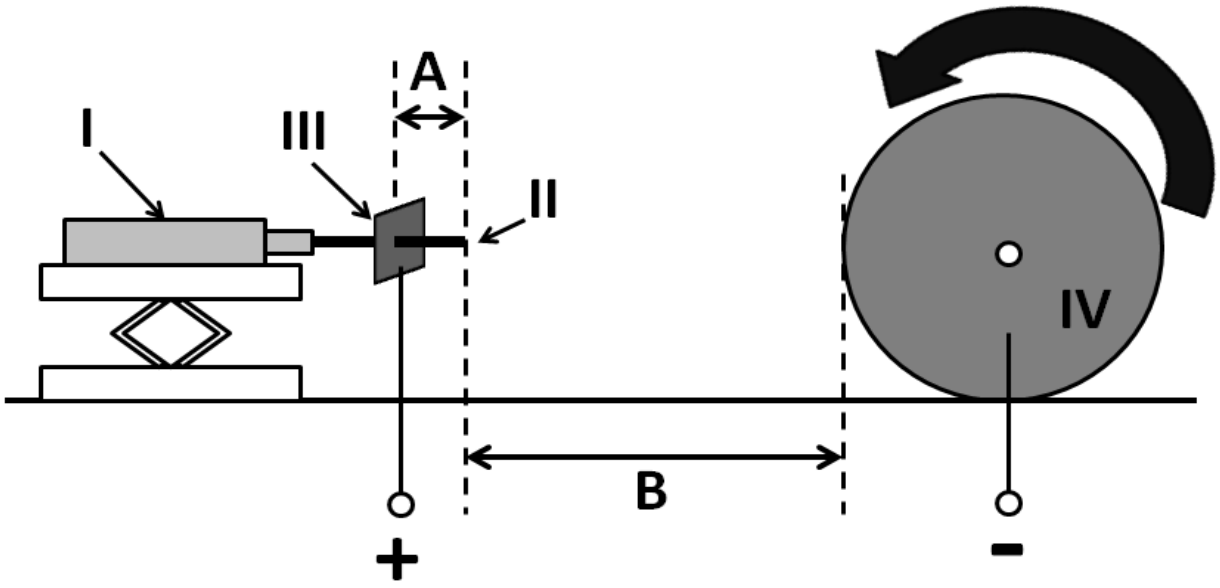


Figure 2.1. Diagram of the electrospinning apparatus.

The syringe pump (I) delivered the polymer solution to the needle (spinneret) tip (II). A 10 x 10 cm aluminum sheet (III) was placed on the spinneret. A high voltage positive charge was applied to the spinneret tip, and thereby to the solution, using an alligator clip fastened to the aluminum sheet. The polymer stream was collected on a rotating disc (IV), to which a negative 2 kV bias was applied by contact with a wire brush. For many of the experiments in this study, the distances between the spinneret tip and the aluminum sheet (A), and between the spinneret tip and collector (B), were systematically varied.

### 2.2.1 Tip-to-collector distance

Various distances between the spinneret and the rotating collector were investigated to determine the effect of tip-to-collector distance on alignment. The voltage applied to the aluminum sheet was adjusted to maintain a steady electrospinning stream at each distance. The syringe tip was initially placed 5 cm away from the grounded rotating disc, where the applied voltage to the tip ranged from 8-10 kV. The syringe pump was then moved back to 10 cm, which required an applied voltage in of 12-15 kV. A 20 cm distance required an applied voltage of 18-20 kV, and a 30 cm working distance required an applied voltage of approximately 22 kV. The rotating disc was maintained at a constant -2kV and 600 RPM throughout.

### 2.2.2 Solvent volatility

The volatility of the solvent was adjusted by changing the relative proportions of chloroform:DMF. PLLA would not dissolve in a mixture of chloroform and DMF, so it was initially dissolved in chloroform alone. DMF was then added in appropriate amounts to obtain ratios (v/v) of 95:5, 90:10, 80:20, and 70:30 chloroform:DMF. These solutions were then electrospun at a tip-to-collector distance of 30 cm with the aluminum sheet placed 1 cm behind the tip of the spinneret.

### 2.2.3 Tip-to-sheet distance

The distance between the tip of the spinneret and the aluminum sheet was systematically varied. The syringe pump was kept at a fixed tip-to-collector distance of 30 cm and a solution of 90:10 (v/v) chloroform:DMF was electrospun. The aluminum

sheet was placed at distances of 0.5, 1, 2, 3, and 5 cm behind the syringe tip with applied voltages of approximately 25 kV, 22 kV, 15 kV, 10-15 kV, and 7-10 kV respectively.

### 2.2.4 Quantification of fiber alignment

Fiber alignment was quantified using Fast Fourier Transform (FFT) analysis of SEM images as described in previous publications [28, 45]. Briefly, images of fibers were taken on an AMRAY 1910 Field Emission Scanning Electron Microscope (FEG-SEM) and analyzed using ImageJ. Regions of 512 x 512 pixels were selected and processed by FFT. MATLAB (MathWorks, Natick, MA) software was then used to average the image intensities from the FFT origin over a full $360^0$ and within a radius of 50 to100 pixels.

Intensity values and corresponding angles were saved to a Microsoft Excel spreadsheet. The average intensities were plotted against the corresponding angles and smoothed by a five point moving average filter, resulting in a curve with two local maxima. At each local maximum, the width of the curve was recorded at half the maximum value, yielding the full width-half max (FWHM). The FWHM is a measure of the extent of alignment, with lower values indicating greater alignment. Statistical analysis of the FWHM was performed using Prism 5 (GraphPad, La Jolla, CA).

## 2.3 Results

Previously, all the electrospinning conducted in our laboratory was performed at a tip-to-collector distance of 5 cm, an applied voltage of 8-10 kV and a solution of 4% PLLA in chloroform [28, 45]. We eventually increased the tip-to-collector distance while

concomitantly increasing the voltage. This increased the density of fibers collected and the consistency of alignment. We also added DMF to the solution to a final volume of 10% DMF and 90% chloroform (v/v). We then placed a 10 x 10 cm square aluminum sheet on the spinneret 1 cm behind the tip to make the electric field more uniform. We systematically investigated how varying the tip-to-collector distance, solution volatility, and tip-to-sheet distance one variable at a time affected fiber alignment and morphology.

Nanofibers were electrospun initially at a tip-to-collector distance of 5 cm. This distance was successively increased to 10 cm, 20 cm, and finally, 30 cm. Images of fibers produced at each distance are depicted in Figure 2.2(A). At a tip-to-collector distance of 5 cm, fiber alignment was substandard, with an average FWHM of 50±4°, which was relatively high in this study. (The lower the FWHM, the more aligned the objects in the sample). The morphology of the fibers was also poor, appearing flat and ribbon-like, as opposed to round in cross-section. This ribbon-like morphology indicated that the solvent had not completely evaporated by the time the fiber was deposited on the collector surface. Doubling the distance to 10 cm improved alignment somewhat, but it was still poor overall, with an average FWHM of 38±1°. Additionally, as at 5 cm, some of the fibers exhibited ribbon-like morphology (data not shown). Doubling the distance again to 20 cm further improved the alignment as can be observed in Figure 2.2(A). The average FWHM at this distance was 20±1°, indicating a significantly improved alignment compared to shorter distances. At 30 cm, there is uniform alignment with an average FWHM of 12±1°, as well as much better uniformity of

diameter, and fibers had circular cross-sections without any ribbon-like fibers. Each increase in distance yielded a statistically significant improvement [Figure 2.2(B)].

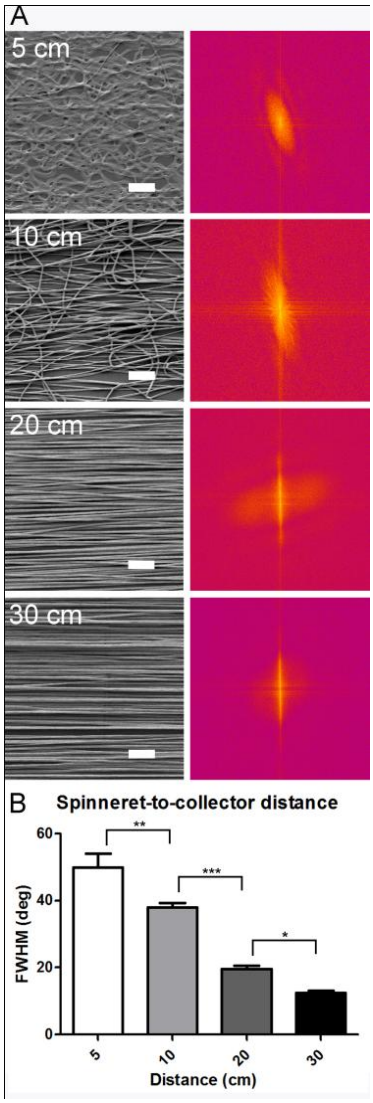


Figure 2.2. Spinneret-to-collector distance.
Increasing the distance between the spinneret and collector resulted in fibers with statistically higher alignment. Samples with a 90:10 chloroform:DMF ratio were electrospun at tip-to-collector of 5 cm, 10 cm, 20 cm, and 30 cm. Note that alignment improves as the distance increases, with the greatest improvement observed qualitatively between 10 and 20 cm. A representative FFT image of a 512 x 512-pixel selection from each SEM image is shown to the right of the corresponding SEM. Image intensities in the FFTs between radii of 50 to 100 pixels were quantified using a MATLAB algorithm and plotted as a function of angle from the point of origin. Once graphed, the widths of the intensity peaks were measured at half the peak height. This measure is called the full width-half max (FWHM). A graph of the average FWHM versus tip-to-collector distance (B) shows significantly higher alignment with greater distances. Using a one-way ANOVA test, these data show that tip-to-collector distance affects fiber alignment significantly to a level of $p<0.0001$. N=13 for each distance tested.*$p<0.05$; **$p<0.01$; ***$p<0.001$.

The fraction of DMF added to chloroform dramatically affects fiber alignment and uniformity. At a chloroform:DMF ratio of 95:5 (v/v), fibers were less uniform in diameter and alignment was less than desired, as seen in Figure 2.3. At a ratio of 90:10, the fibers were highly aligned and had uniform diameters. When the amount of DMF was doubled to a ratio of 80:20, there was less uniformity in diameter and some of the fibers had a ribbon-like morphology, with some bleeding observed between adjacent fibers [Figure 2.3(80:20)]. This is indicative of less evaporation of the solvent from the stream prior to deposition of fibers on the collector. Further increasing DMF to a ratio of 70:30 increased this effect to the point that splatter of the solution was observed [Figure 2.3(70:30)]. Alignment of the deposited fibers also decreased substantially. The beading, ribbons, and splatter observed in samples electrospun using solvent ratios other than 90:10 distort the FFT and obscure the signal produced by the fibers. As a result, alignment was not quantified for these experiments. Addition of the aluminum sheet also improved fiber alignment and uniformity (Figure 2.4). Omission of the aluminum sheet resulted not only in intermediate (submaximal) fiber alignment, but also a lower number of fibers collected because the stream was directed away from the collecting edge to adjacent parts of the apparatus. At 0.5 cm, no stream could be produced, and at 0.75 cm, only an intermittent stream was produced [Figure 2.4(a)]. At 1 cm, the best alignment was observed with an average FWHM of 14±1°. At 2 cm, fibers began to overlap with one another producing an average FWHM value of 21±0.3°. At 3 cm tip-to-sheet distance, fibers appeared similar to those produced at 2 cm, but with somewhat greater overlap. When the aluminum sheet was moved to 5 cm behind

the tip of the spinneret, the overlap increased such that some fibers began to cross the desired direction of alignment in their entirety, increasing the FWHM value to 30±2°.

We also observed that the position of the aluminum sheet affected the length of the stream (visible portion of the stable jet). Moving the sheet beyond 1 cm behind the tip decreased the length of the stream. Positioning the sheet at 1 cm maximized the length of the stream, and as stated before, the stream ceases entirely when the sheet is moved closer to the tip. Figure 2.5 shows a representative example of one of these long stable jets.

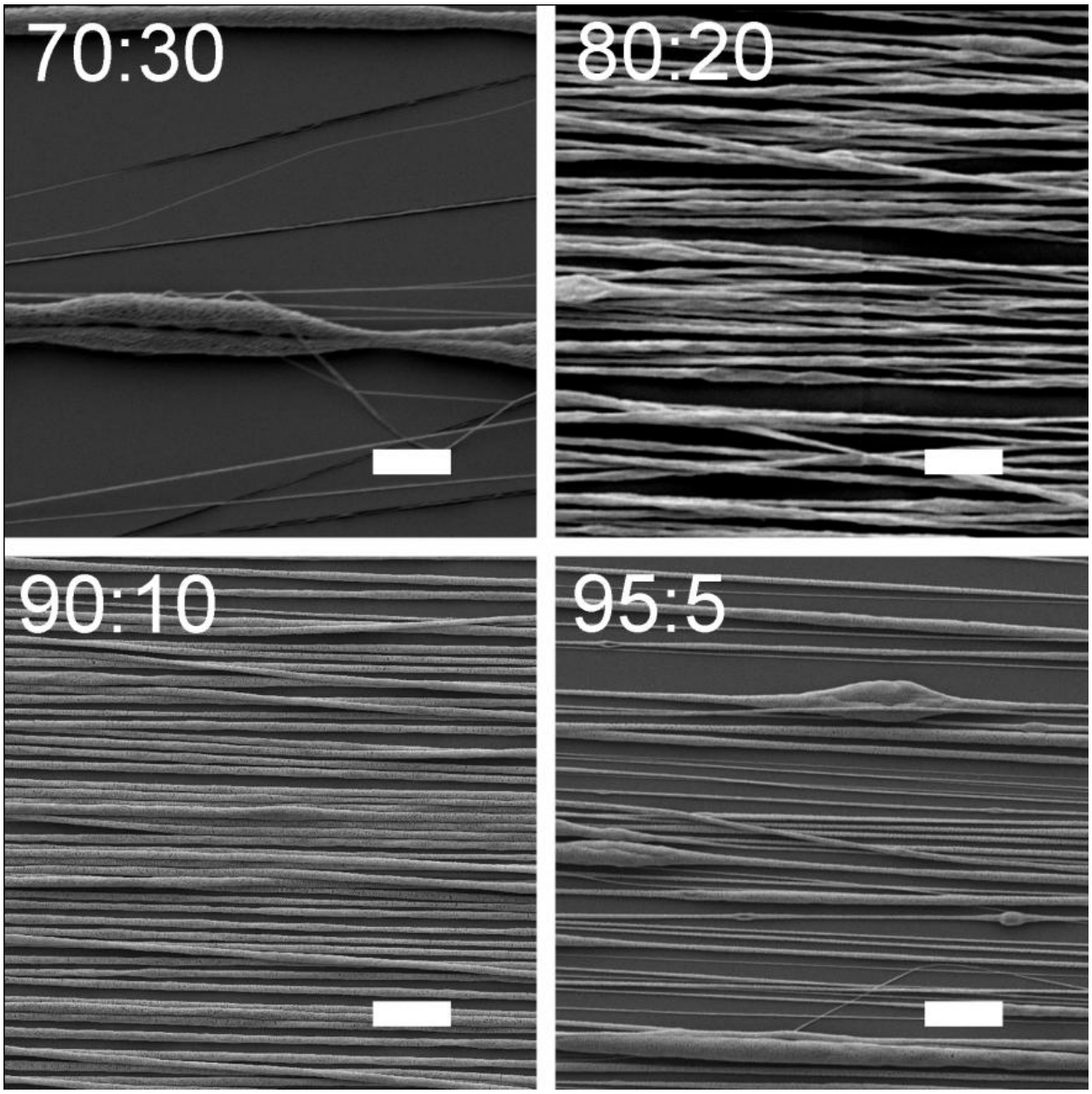


Figure 2.3. Solvent volatility.
Changing the solvent volatility affects the morphology of the electrospun fibers. PLLA was dissolved at 4% (w/v) in varying ratios of chloroform:DMF (v/v) and electrospun with a tip-to-collector distance of 30 cm with the aluminum sheet located 1 cm behind the spinneret. A ratio of 90:10 (v/v) chloroform:DMF produced fibers with the most uniform morphology and highest alignment. A ratio of 80:20 produced fibers with a ribbon-like morphology and some fiber overlap. This effect worsened with a ratio of 70:30, such that fibers were less uniform in diameter, morphology, and alignment. Splattering and bleeding of fibers were also observed at this solvent ratio. A ratio of 95:5 produced fibers that were less uniform in morphology and alignment and with a beaded morphology.

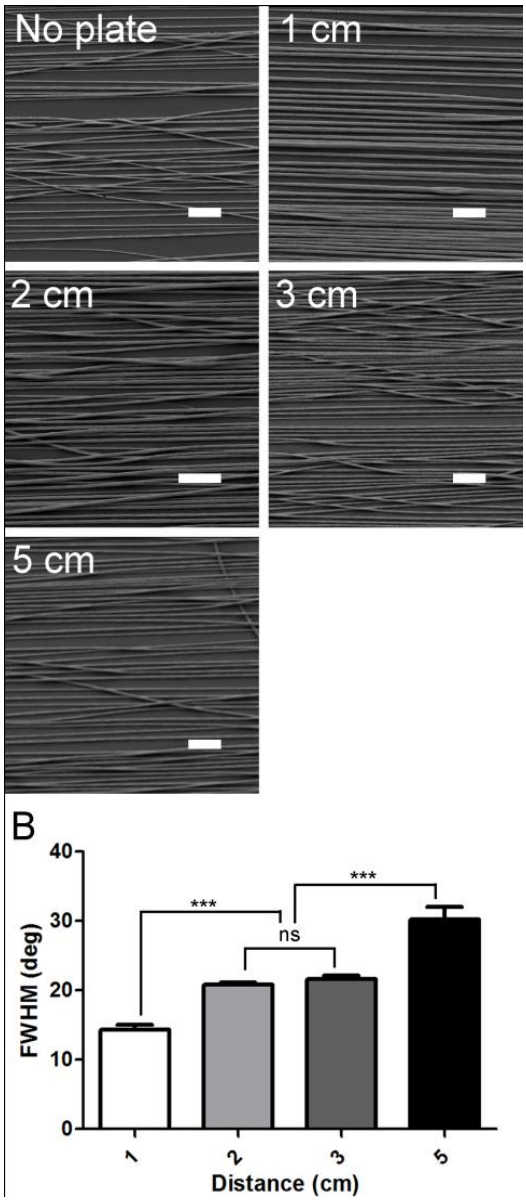


Figure 2.4. Tip-to-sheet distance.
Varying the placement of the aluminum sheet behind the spinneret from 1 cm resulted in fibers with lower alignment. A 23 gauge needle (spinneret) was placed on a syringe containing the polymer solution with a 90:10 chloroform:DMF (v/v) solvent ratio. A 10 x 10 cm aluminum sheet was place on the spinneret by piercing the center of the sheet and moved to different distances behind the tip of the spinneret. All samples shown were electrospun at a tip-to-collector distance of 30 cm. (A.) Fibers with the highest alignment were produced using a tip-to-sheet distance of 1 cm. Omission of the sheet produced inferior fiber alignment. Fibers spun using tip-to-sheet distances of 2 cm, 3 cm, and 5 cm produced progressively worse alignment. B. A plot of full width-half max values versus tip-to-sheet distance shows that distance between the sheet and tip affects fiber alignment significantly to a level of $p<0.0001$, using a one-way ANOVA test. N=10 for each distance tested. ***$p<0.001$.

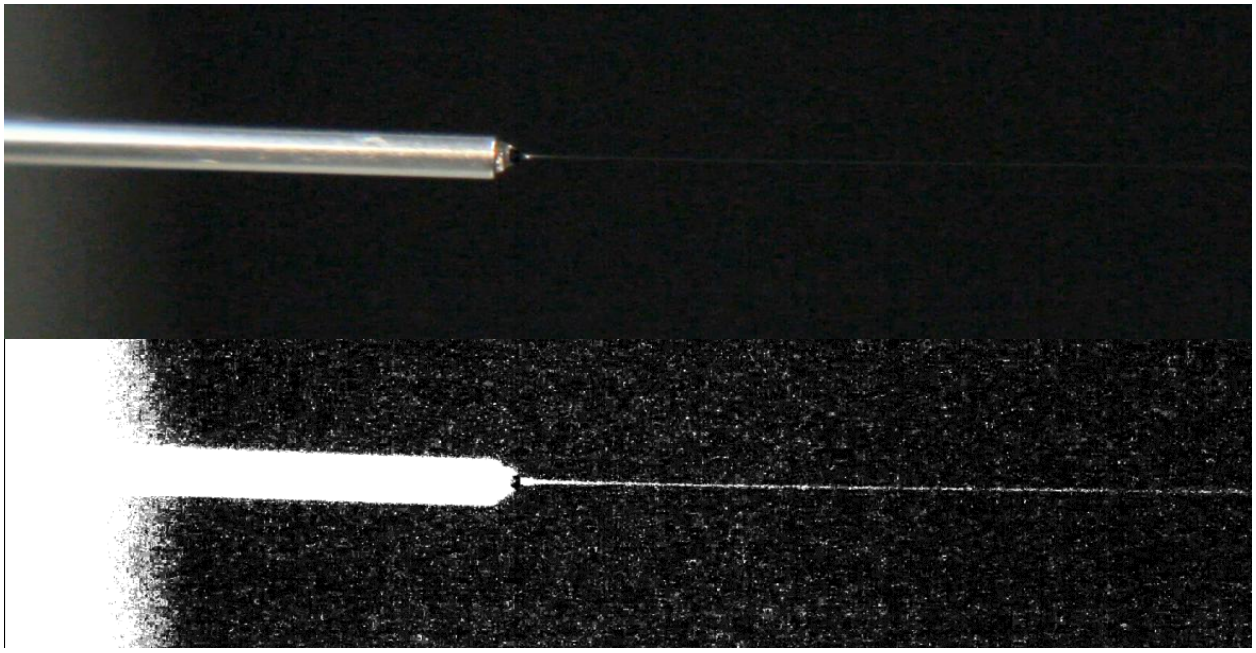

Figure 2.5. Stable jet.
The length and stability of the stable jet was affected by the tip-to-collector distance, solution volatility, and tip-to-plate distance. We observed that fibers with the greatest alignment were produced when the visible stable jet was both long and steady, original image (top) and with high contrast (bottom). Sputtering and wagging of the stable jet produced fibers with a beaded morphology and a lower extent of alignment.

## 2.4 Discussion

In our initial effort to improve nanofiber alignment, we moved the spinneret away from the collector. We began to notice a longer visible stable jet (stream) at greater distances, but we also observed that it was less steady. To stabilize the stream we decreased the volatility of the solution by adding DMF and adjusted the position of the aluminum sheet.

### 2.4.1 Tip-to-collector distance

In order to investigate the effect of increased tip-to-collector distance on alignment, we systematically increased the tip-to-collector distance beyond the 5 cm used in previous publications [28, 45]. Increasing this distance dramatically increased alignment. The maximum tip-to-collector distance that we tested, 30 cm, resulted in fibers with the highest alignment. Previous studies of electrospinning at tip-to-collector distances approaching 30 cm used an electrospinning apparatus oriented in a vertical direction toward a stationary collector [113]. To the best of our knowledge, our study is the first to use a horizontal electrospinning set up at such a distance and the first to demonstrate that 30 cm produces dramatic improvements in alignment. The results of our study showing that alignment increases with increasing distance agree with other recent studies. A study conducted by Afifi and colleagues showed that fibers electrospun at greater tip-to-collector distances were more aligned than those electrospun at shorter distances[97]. As in our study, their electrospinning apparatus was oriented horizontally. However, their maximal tip-to-collector distance was 20 cm with an applied voltage of 10 kV. As the degree of alignment they obtained by

electrospinning was not to their satisfaction, their fibers were then drawn (stretched) 2 to 3 times to maximize the alignment. This additional step of drawing the fibers was not necessary in our experiment.

Increasing the tip-to-collector distance is not the only way of increasing alignment; changing the geometry of the collector can also improve alignment, as shown by Bazbouz and colleagues. In these studies, a pair of parallel discs was used as a (stationary) collector which was positioned 8 cm away from the spinneret. Increasing the distance between the two discs increased alignment of the fibers. Fibers with the greatest alignment were collected at a maximum distance of 6 cm [100]. Additionally, Sundaray and colleagues found that short tip-to-collector distances of 1-3 cm allowed for greater control and stability of the polymer jet and resulted in greater alignment of polystyrene fibers. However, they also found that their highly aligned fibers were flattened at short tip-to-collector distances [114].

### 2.4.2 Solvent Volatility

Decreasing the solvent volatility by the addition of DMF improved not only the alignment of the electrospun fibers, but at lower concentrations had an even greater effect on the uniformity. The study conducted by Afifi and colleagues also used the same 90:10 ratio of a chlorinated methane (dichloromethane) to DMF to produce highly aligned fibers. As we discovered in our study, at tip-to-collector distances of 10 cm and shorter, fibers were wet when contacting the collector resulting in bleeding together and ribbon-like morphology [97].

We hypothesize that the bleeding together and flattening of fibers is due to a less volatile solvent because at short distances there is not enough time for the solvent to evaporate completely. Previous research bears this out. Wannatong and colleagues showed that with less volatile solutions, they obtained beading and ribbons in their fibers. They found from testing a variety of solvents that those with higher boiling points (less volatile) produced a higher incidence of ribbons and beads in the fibers at room temperature[109]. We similarly found that ribbons and splattering occurred in our fibers when electrospun with higher concentrations of DMF. They found that this effect could be corrected by increasing the ambient temperature, which presumably speeds evaporation of solvent from the stream, allowing the fiber to dry completely before reaching the collector [110].

### 2.4.3 Tip-to-sheet distance

The addition of a flat folded sheet of aluminum foil to the spinneret resulted in fibers with higher alignment when the sheet was positioned 1 cm behind the tip of the spinneret. Moving the sheet further back resulted in fibers with lower alignment. When the tip-to-sheet distance was 1 cm, the stream was more stable near the tip of the spinneret. As the tip-to-collector distance was increased, wagging and oscillating of the stream was observed. Our rationale for using the sheet was to make the electric field near the tip of the spinneret more uniform in an attempt to steady the stream.

Other investigators have used conductive rings and concluded that they helped to stabilize the stream. Traversa used a 180 mm diameter copper ring immediately beyond the tip of the spinneret[102]. Buttafoco also used a stainless steel ring between

the tip and the collector [103]. Deitzel and colleagues used three rings, which they aptly termed “electrostatic lenses”, and biased each ring at approximately half of the voltage applied to the spinneret (9kV). By increasing the potential as the stream approached the collector, they were able to stabilize the stream due to the convergence of electric field lines [114].

### 2.4.4 Stream stability

We found that we could predict reasonably well whether or not fibers would be aligned by observing the behavior of the stream (visible portion of the stable jet) during the electrospinning process. When the stream was steadier and longer, we obtained better aligned fibers. The position of the aluminum sheet caused the stream to wag, oscillate or stabilize depending on how far behind the spinneret tip the sheet was placed. Fibers electrospun with long tip-to-sheet distances had the least stable streams and were less aligned, leading us to speculate the existence of a relationship between alignment and the visible stable jet’s length and stability. A study conducted by Qin and colleagues focused on the properties of the polymer stream rather than the fibers produced. They speculated that there was a relationship between the diameter of the jet and the point along its axis where it begins to lose its stability [115]. We suspect that the length and stability of the stable jet is an indicator of the uniformity of the electric field between the tip and the collector. The stability and length of the stable jet and the corresponding effect on fiber alignment remains an interest for further study, with the prospect of improving the reproducibility of aligned fibers.

### 2.4.5 Nerve regeneration conduits and electrospun fibers

With the knowledge gained from this investigation of electrospinning parameters, we gained the ability of produce highly aligned fiber bundles quickly and with high reproducibility. High alignment is a crucial component of nerve guidance channels and reproducibility is essential for rigorous research. The next chapter describes the development of an automated assay to characterize the morphological maturity of motor neurons cultured on these highly aligned fibers.

# Chapter 3. Stages of neuronal morphological development *in vitro* – An automated assay[91]

Following plating *in vitro*, neurons pass through a series of morphological stages as they adhere and mature. These morphological stage transitions can be monitored as a function of time to evaluate the relative health and development of neuronal cultures under different conditions. While morphological development is usually quite obvious to the experienced eye, it can often be difficult to quantify in a meaningful way. Morphology quantification typically relies on manual image measurement and can therefore be tedious, time consuming and prone to human error. Here we report the successful development of an automated process using the commercially available image analysis program MetaMorph® to analyze the morphology and quantify the growth of embryonic spinal motor neurons *in vitro*. Our process relied on the Neurite Outgrowth and Cell Scoring modules included in MetaMorph® and on analyzing the exported data with an algorithm written in MATLAB®. We first adopted a series of stages of motor neuron development *in vitro*. Neurons were classified into these stages directly from the available output of MetaMorph® using the algorithm written in MATLAB®. We validated the results of the automated analysis against a manual analysis of the same images and found no statistically significant difference between the two methods. When properly configured, automated image analysis with MetaMorph® is

a rapid and reliable alternative to manual measurement and has the potential to accelerate the research process.

## 3.1 Introduction

Since the seminal description of neuronal morphology developed by Dotti and Banker in 1988, it has been easier for neuroscientists to qualitatively describe neurons as they acquire a stereotyped neuronal morphology. The study of neuronal morphology remains important to many areas of basic neuroscience, including neuritogenesis [116, 117], development [118, 119], synaptogenesis and plasticity [120-122], as well as axon specification and polarity [89, 123-125]. It is also critical for areas of applied neuroscience, including stem cell transplantation [126, 127] and the study of neuronal response to regeneration scaffolds that rely on novel biomaterials, the focus of our laboratory and that of many others [28, 31, 45-47, 81, 128].

For these and other areas of research that regularly involve monitoring changes in neuronal morphology, quantifying aspects of morphology could be extremely beneficial. However, while qualitative recognition of neuronal morphology can be straightforward to the experienced investigator, quantitative analysis is extremely tedious and time consuming. Meaningful measurements necessitate sampling a multitude of cells, requiring hundreds, if not thousands, of measurements. Taken by hand, such measurements are tedious and time consuming, and represent a significant bottleneck in the progress of research. In the interest of timely advancement, researchers may feel compelled to limit the number of measurements per cell or the number of cells examined, which in turn may limit valuable knowledge or statistical

power. We experienced the time consuming nature of manual measurements in one of our recent studies, in which well over one hundred hours were spent determining neurite length, number of neurites, possession of a major neurite and the developmental stage of embryonic spinal motor neurons *in vitro*[81]. Following this experience, we began to search for a suitable alternative to manual measurement.

There is a nearly fifty year history of using computer aided image analysis to investigate neuronal morphology (Glaser, 1965). Key subtasks of the process include thresholding, segmentation, tree analysis and quantification. Thresholding is the task of determining the area of the image that contains the neuron(s) – the remainder of the image is discarded as background. Segmentation is the process of subdividing that area, which involves not only separating individual neurons from their neighbors, but breaking individual neurons down into their constituent parts (nucleus, soma and processes). Tree analysis at its simplest involves classifying process segments as primary, secondary, tertiary, etc. branches. Quantification merely involves gathering meaningful data from each individual segment; typical measures include area of soma and process number and length. A variety of commercial and freeware tools exist that perform some or all of these tasks; for an excellent review of this topic and existing software tools, see Meijering (2010)[129].

For this investigation, MetaMorph® was our software tool of choice. MetaMorph® has been used before to identify neurons and quantify neuronal morphology [130, 131], as have other software packages such as Neuromantic® [132], NeuronJ [133] and HCA-Vision [134]. Our selection of MetaMorph® (as opposed to one of the many other image processing tools available) was motivated simply by the fact

that we already had access to the software. Within MetaMorph®, we used the Neurite Outgrowth and Cell Scoring modules to quantify the morphology of immunostained neurons from fluorescent images. The Neurite Outgrowth module accomplishes the four main subtasks discussed above (thresholding, segmentation, tree analysis and quantification) and the Cell Scoring module eliminates data from any non-neuronal cells that may be present in the image. We found that MetaMorph® has a fairly intuitive user interface, even for those with no prior image processing experience. The output from MetaMorph® is suitable for further automated post-processing. After obtaining data from these MetaMorph modules, we used an algorithm implemented in MATLAB® to sort the cells by morphological stage. We compared this data to a manual count of the same images and found no statistically significant difference between the two. In this manuscript, we demonstrate a method of automated image analysis with MetaMorph® that, when properly configured, can be a rapid and reliable alternative to manual measurement. This technique represents a low-cost, high-throughput method to determine morphological changes in neuronal development in culture.

## 3.2 Materials and methods

### 3.2.1 Cell culture, immunocytochemistry and image capture

As the image processing methods presented here are applicable to any low-density preparation of neuronal cells, we refer the interested reader to previous publications [28, 81, 135, 136] for a detailed description of culture technique. Briefly, neurons were obtained from E15 Sprague-Dawley rat embryos and plated on glass at a density of 25 cells $mm^{-2}$ in Neurobasal media (Gibco) supplemented with B27 and other

additives [28, 135, 136]. Glass substrates were pre-coated with 100 ug $ml^{-1}$ poly(-L-lysine) for 1 hour prior to plating. Cells were fixed at 3, 6, 12, 24, 36, 48 and 96 hours post-plating in 4% paraformaldehyde for 30 minutes at room temperature. Fixed samples were stained with the neuronal marker primary anti-β-tubulin (Tuj-1) (1:500) (BD Biosciences, San Jose, CA) overnight at room temperature and then labeled with FITC-conjugated goat anti-rabbit secondary (1:200) (Sigma-Aldrich, St. Louis, MO) for four hours at room temperature. The samples were mounted on slides with Prolong Gold (Invitrogen, Carlsbad, CA) containing the nuclear counter-stain DAPI. Images were acquired on a Nikon Diaphot wide field fluorescence microscope at 20X magnification with a Hamamatsu ORCA CCD camera with Compix Simple PCI and saved as 24 bit multi-channel false-colored TIFF images. At least eight fields per time point were analyzed, resulting in a total of approximately 1000 neurons analyzed. Each time point consisted of data from at least two separate trials.

### 3.2.2 Developmental stages defined

Motor neuron maturation was divided into four stages based on patterns of growth observed in previous studies [81, 88]. Stage zero was defined as a round cell body with no outgrowth or small processes with length less than 10% of the diameter of the cell (d). Stage one cells possess lamellipodial or small process outgrowth with process length greater than 10% of d but not longer than d. Stage two cells possess at least one neurite (a process with length > d) but no axon. Stage three cells possess an axon (length > 2d) and may or may not have other processes.

### 3.2.3 Manual cell scoring

To compare with the automated process, identical photomicrographs of neurons were analyzed by hand using NIH ImageJ. Cells were classified by the developmental stages described in section 3.2.2 above. In the interests of speed, a visual analysis was used to assign every neuron a stage number. In cases where the stage of a neuron was not immediately apparent or borderline, the measuring tool in Image J was used to make the determination.

### 3.2.4 Automated image analysis

#### 3.2.4.1 Overview

A flowchart (Figure 3.1) illustrates the image analysis process. Three programs are used in the process: MetaMorph® (Molecular Devices, Downingtown, PA), Microsoft Excel and MATLAB® (MathWorks, Inc., Natick, MA). Within MetaMorph®, two modules are utilized: Neurite Outgrowth (OG) and Cell Scoring (CS). MetaMorph® automatically exports the data from these modules directly into Excel worksheets through a DDE (dynamic data exchange). A custom algorithm implemented in MATLAB® then imports the Excel spreadsheets, removes data from ‘negative’ (non-neuronal) cells and then assigns each ‘positive’ cell (neuron) a developmental stage number based on the measurements made by MetaMorph®.

#### 3.2.4.2 Strategy

Before automation of the analysis, the user must tailor the settings within the MetaMorph® modules according to the characteristics of the images to be analyzed.

Intensity above background, cell body size and neurite outgrowth length can vary between experiments and time points within the same experiment, so in order to achieve accurate results, the user must process 2-3 representative images manually in MetaMorph®, checking to see if the settings give accurate and reliable results. Once the user is satisfied with the module settings, the ‘journal’ function in MetaMorph® can be configured to automatically analyze the remainder of the images. The user simply hits a ‘record journal’ button, processes one image, stops recording and then instructs the journal to run the recorded steps on every image in a specified directory. MetaMorph® completes the analysis and exports the data into Excel spreadsheets without further user intervention.

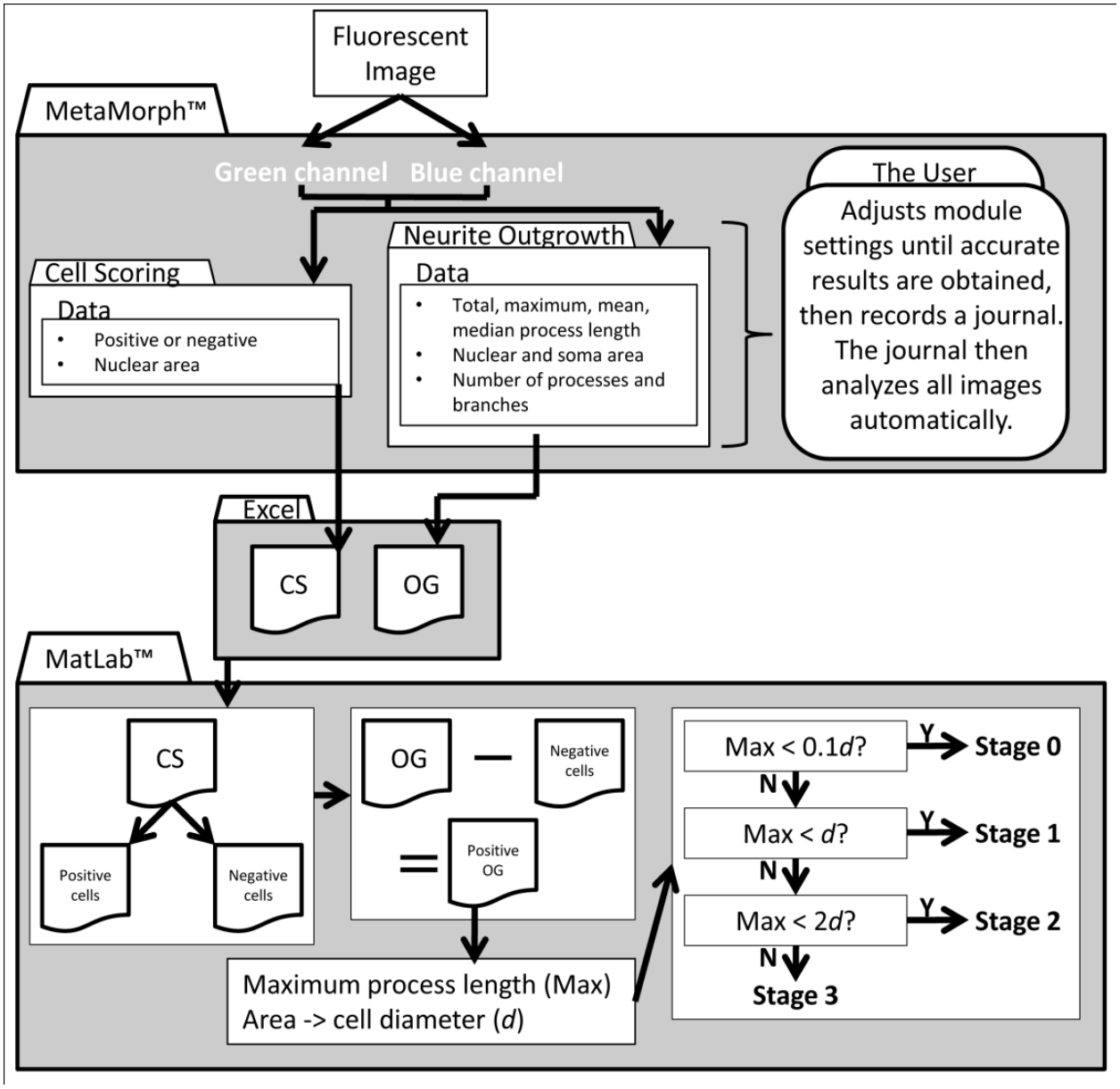


Figure 3.1. Flowchart of the automated image analysis process.
A representative fluorescent image is initially loaded into MetaMorph® and the user determines the appropriate settings for the neurite outgrowth (OG) and cell scoring (CS) modules. The 'journal' function in MetaMorph® then analyzes all the images and exports the data into Excel spreadsheets. The spreadsheets are then imported into MATLAB® and processed by an algorithm that removes negative cell data (non-neurons) and then assigns the positive cells (neurons) a developmental stage based on the length of the longest process (Max) compared to the cell diameter (d).

### 3.2.5 MetaMorph®

#### 3.2.5.1 Pre-processing

The images were opened in MetaMorph® and separated into 8 bit single channel images. The blue channel was used to visualize the DAPI stained nuclei and the green channel visualized the Tuj-1 stained cell bodies and processes. The red channel contained no information and was discarded at this point. Since MetaMorph® modules require 16 bit input, the 8 bit images were converted to 16 bit using the 'multiply arithmetic process' step available in MetaMorph® for such conversions. A DDE (dynamic data exchange) log was opened to allow the MetaMorph® modules to export data directly into Excel® spreadsheets.

#### 3.2.5.2 Basic operations used to determine module settings

Measuring lengths

Lengths were measured using the straight line measuring tool to draw a line across the object of interest (measuring tool results are displayed in the status bar at the bottom of the screen).

Intensity above local background

To find the intensity above background, we visually located the faintest cell in the image and zoomed in until individual pixels could be identified. The mouse pointer was used to measure the intensity of the least bright pixel within the cell body and a low intensity pixel in the background adjacent to the cell body. The two intensity values were

subtracted and the result entered into the dialog box as intensity above local background.

Area calculation

To find the minimum area, we located the smallest motor neuron in the image and calculated the area by measuring the radius with the line measuring tool.

#### 3.2.5.3 Neurite Outgrowth (OG) module

The OG module measures the processes of each cell and exports total process outgrowth, mean processes length, maximum processes length, nuclear area and soma area. The OG dialog box (Figure 3.2 right) contains three subsections: Cell Bodies, Nuclear Stain and Outgrowths. In the Cell Bodies subsection, there are three settings: approximate max width, intensity above local background and minimum area. A document located in the MetaMorph® help section (document ID T20029) describes how to create the three settings for the OG dialog box, which is described in detail in Section 3.2.5.2 above. In the Nuclear Stain subsection, the optional box was checked and the 16 bit blue channel image was selected. Approximate min width, approximate max width and the intensity above local background were calculated for the nuclei as described in Section 3.2.5.2. For the Outgrowth subsection, maximum width and intensity above background were also calculated as in Section 3.2.5.2. The minimum cell growth to log as significant was found by locating the shortest neurite in the image and measuring it manually. Once all the settings were defined, the apply tab was clicked to process the image. At this point, MetaMorph® created an Excel spreadsheet and exported the OG module results into it through the DDE.

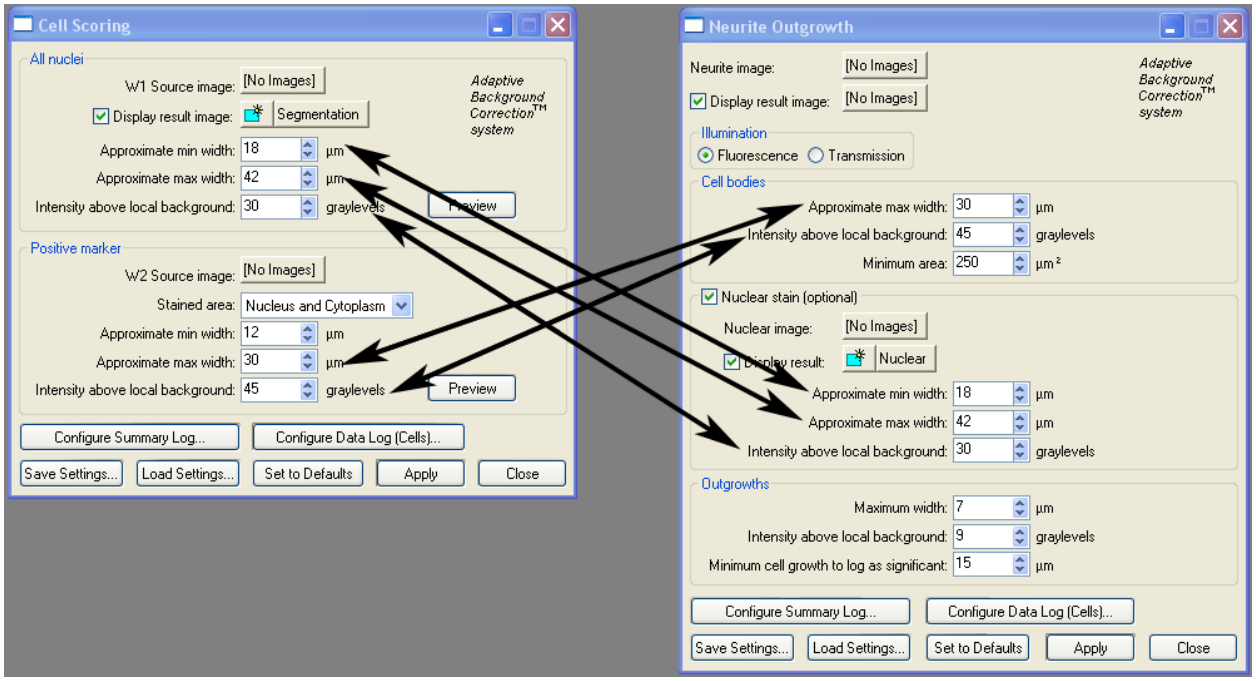


Figure 3.2. Dialog boxes.
The Cell Scoring (left) and Neurite Outgrowth (right) module dialog boxes. Arrows indicate the fields in the Cell Scoring box that must match the values used in the Neurite Outgrowth module.

#### 3.2.5.4 Cell Scoring (CS) module

The CS module identifies any non-neuronal cells in the images. The CS module identifies ‘positive’ cells (neurons) by the co-localization of a nucleus in the blue channel and Tuj-1 staining in the green channel. Nuclei without Tuj-1 staining are classified as ‘negative’ (non-neuronal) cells. The CS module dialog box (Figure 3.2 left) contains two subsections: All Nuclei and Positive Marker. In the All Nuclei subsection, the blue channel image was entered as the W1 Source. The green channel image was entered as the W2 Source in the Positive Marker subsection. Based on our choice of antibody (Tuj-1), the stained area option selected was ‘nucleus and cytoplasm’. The numbers entered into the CS dialog box exactly matched the numbers entered into the OG box (arrows in Figure 3.2). The value unique to the CS dialog box (approximate min width) was calculated as described in Section 3.2.5.2. Once all the settings were defined, the apply tab was clicked to process the image. MetaMorph® then created a second Excel spreadsheet and exported the CS module results into it through the DDE.

### 3.2.6 Excel

No operations were performed in Excel. MetaMorph® simply conveniently outputs data from the OG and CS modules through a DDE into Excel for saving.

### 3.2.7 MATLAB®

The Excel spreadsheets containing the data from MetaMorph® were imported into MATLAB® for stage determination with the following code:

```
[CS, CSTXT, CSraw] = xlsread(uigetfile('*.xls','Select the Cell Scoring file'));
[OG, OGTXT, OGraw] = xlsread(uigetfile('*.xls','Select the Outgrowth file'));
numberCells = size(CS);
```

While MetaMorph® does assign every analyzed cell a numerical label, the CS and OG modules unfortunately number the cells differently, so a secondary step was necessary to match the ‘negative’ cells identified by the CS module to their equivalent OG cells to exclude them from further analysis. Since the same values were input into each module dialog box, the nuclear areas of the negative cells were calculated identically by both modules. The negative cell nuclear areas were then matched to their equivalents in the OG data and the corresponding negative cell data eliminated as follows:

```
for i = 1 : numberCells
   if strcmp( 'Negative', CSTXT( i, 9 ))
      for j = 1 : numberCells
         if CS( i-1, 10 ) == OG( j, 15 )
            OG( j, : ) = NaN;
            break
         end
      end
   end
end
MaxProc = OG(~isnan(OG( : ,12 )), 12 ); area = OG(~isnan(OG( : ,15 )), 15 );
```

Once all the data from the negative cells was eliminated, the diameter of the remaining positive cell bodies was approximated in MATLAB® by modeling each cell as

a circle with area equal to the soma area found by the OG module. The cells were then staged according to the definitions described in Section 3.2.2 by comparing the diameter to the length of the longest process (MaxProc).

```
Diameter = 2*sqrt(area / 3.14); numberNeurons = size( MaxProc );
for i = 1 : numberNeurons
   if MaxProc( i ) == 0 || MaxProc( i ) <= 0.1*Diameter( i )
      S(i) = 0;
   elseif MaxProc( i ) <= Diameter( i ) && MaxProc( i ) > 0.1*Diameter( i )
      S(i) = 1;
   elseif MaxProc( i ) > Diameter( i ) && MaxProc( i ) < 2*Diameter( i )
      S(i) = 2;
   else
      S(i) = 3;
   end
end
```

The resulting variable (S) is a 1 x N matrix where N is the number of neurons present in the analyzed images; S(i) evaluates to the stage number of the i-th neuron.

### 3.2.8 Statistics

Statistical analysis for our comparison study was performed in Prism 5.0 (GraphPad, La Jolla, CA) using a Chi-square analysis. P-values less than 0.05 were considered statistically significant.

## 3.3 Results and Discussion

This method satisfies our requirement for an automated analysis system that performs at least as well as a manual count in significantly less time. A comparison between the output of the staging algorithm and the results of a manual count are depicted in Figure 3.3. No significant differences were observed in these data. We were able to define one set of settings for the OG and CS modules that produced

accurate and reliable results for neurons at all time points. Additionally, MetaMorph® supplied us with a substantially greater amount of data compared to our manual count. MetaMorph® measures and exports the number of processes, total outgrowth length, maximum process length, mean process length, nuclear area and soma area for every cell, which is then used to determine the stage number. Our manual count determined only the stage number of the cell – no manual measurements were collected. Furthermore, MetaMorph® determined all these variables in the course of a single afternoon. Our manual count took three times as long to collect only a fraction of the same data. Based on previous experience, we estimate that manually taking all the measurements MetaMorph® made would have required more than one hundred work hours.

Previous work in our laboratory [81] employed five (0-4) stages to describe the morphological development of motor neurons. Here, we were only able to characterize four (0-3) stages of morphological development (Figure 3.4). Our previous study differentiated between cells that displayed one versus multiple neurites. We were unable to do so here because MetaMorph® outputs the length of the longest process, the average process length and the number of processes – but not the individual process lengths. This drawback is an example of the somewhat ‘black box’ design of MetaMorph®; while MetaMorph® has clearly acquired the individual process lengths in the course of calculating the mean, there is no way for the user to access this data.

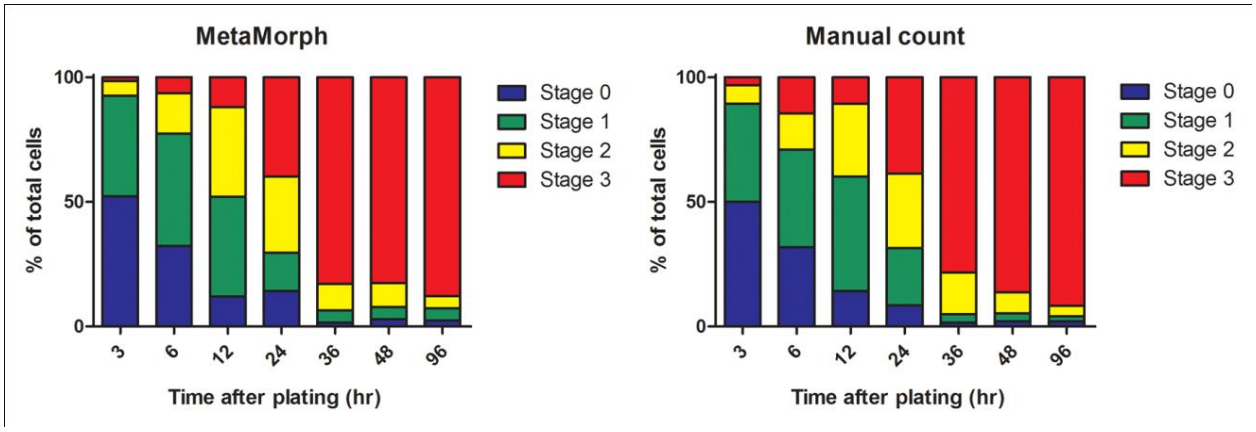


Figure 3.3. Hand count versus automated results.
Comparison of stages of development of motor neurons analyzed at various time points as determined by MetaMorph® (left) and manual measurement (right). A Chi-square analysis found no significant differences between the results of the two methods.

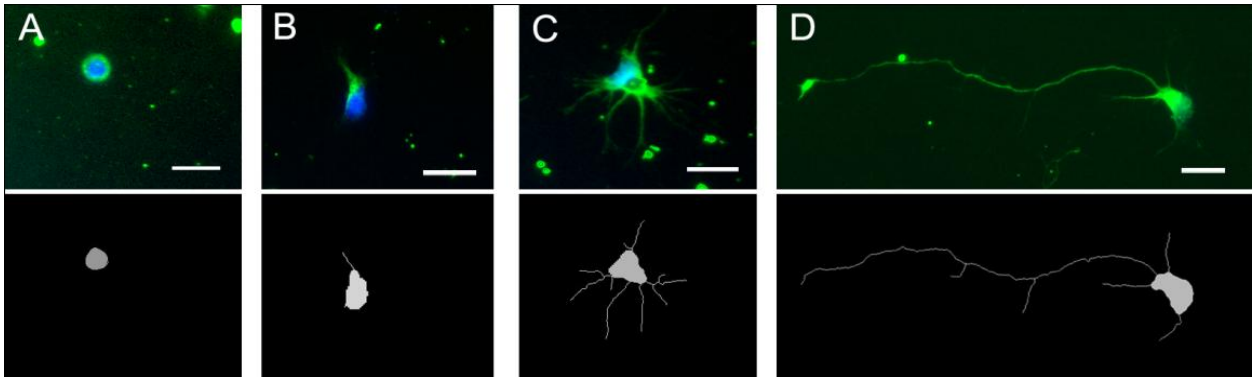


Figure 3.4. Representative stages of motor neuron development.
Representative stages of motor neuron development and corresponding output from the MetaMorph® neurite outgrowth module. Neurons are stained with Tuj-1 (green) and DAPI (blue). A.) Stage 0 – no outgrowth or outgrowth less than 10% of the cell diameter (d); B.) Stage 1 – outgrowth more than 10% of d but less than d; C.) Stage 2 – neurite(s) with length greater than d but less than 2d; and D.) Stage 3 – an axon with length greater than 2d. Scale bars are 20 µm.

This clearly limits the applicability of MetaMorph® to complex morphological investigations where the neurons of interest exhibit very highly branched morphologies. Investigators requiring very specific measurements should evaluate all the software available to be sure the package they choose is capable of providing the level of detail they desire. However, MetaMorph® proved itself to be a suitable solution for our specific goal of quantifying the morphological development of motor neurons following plating. MetaMorph® is a useful tool for detecting simple morphological changes for those with little image processing experience. It would however be extremely valuable if future versions of MetaMorph® allowed researchers access to all the raw data obtained by the Neurite Outgrowth module.

We found that MetaMorph®, when properly configured, could detect and trace all stages of neurons with good fidelity. However, when the settings in the module dialog boxes were not optimized for the images under analysis, substantial inaccuracy was introduced into the data. Specifically, the intensity settings should be optimized according to the procedure described in Section 3.2.5.2 as well as the MetaMorph® Help documentation (document ID T20029) (Figure 3.5). While MetaMorph® enables the automation of the measurement, the user must still be diligent in ascertaining whether the settings continue to be appropriate for every new group of images. It should also be noted that the accuracy of MetaMorph® is dependent not only on the correct settings, but on the quality of the input images. Images suffering from over- or under-exposure or significant non-specific staining may be unsuitable or require additional pre-processing steps, such as further thresholding, before processing with the OG and CS modules.

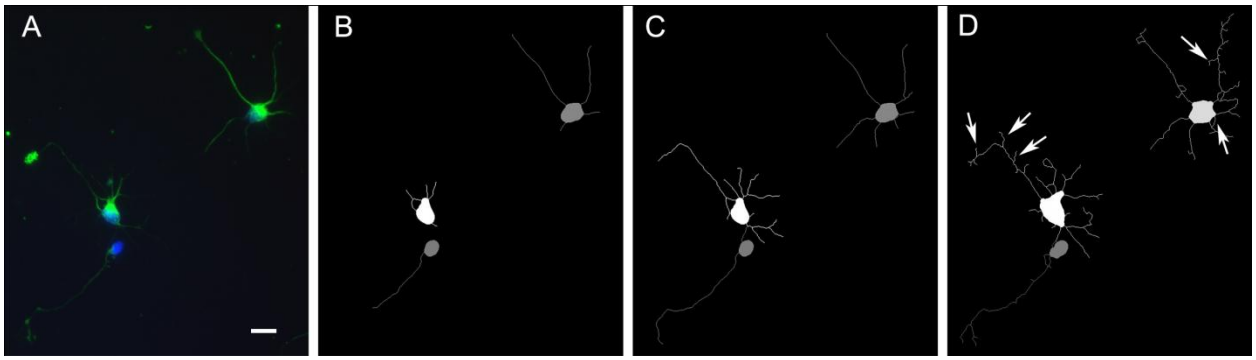


Figure 3.5. Optimization.
An example of how optimization of module settings is crucial to obtaining accurate results. The fluorescent image of neurons stained with Tuj-1 (green) and DAPI (blue) in (A) was processed in MetaMorph®. In (B) the intensity above local background was set too high such that some neurites were not properly traced. In (C) the intensity above local background setting was optimized for the image and good fidelity of neurite tracing was obtained compared to the original image (A). In (D) the intensity above local background was set too low and white arrowheads indicate the position of some traced 'branches' that are not actually present in the original image (A). Scale bar = 20 μm.

The CS module successfully removed non-neuronal cells from further analysis (Figure 3.6). However, if this step had been omitted, data from non-neuronal cells analyzed indiscriminately by the OG module would have been incorrectly classified as stage 0 cells by the staging algorithm in MATLAB®. Additionally, for some cell culture preparations, it may be necessary to run the CS module more than once to remove multiple non-neuronal cell types. The staging algorithm in MATLAB® can be easily adapted to accommodate multiple CS data input files. Depending on the staining, the user may also want to use the Multi-wavelength Cell Scoring (MWCS) module in MetaMorph®. The MWCS module accommodates multi-channel cell sorting. For example, had we employed a second antibody in the red channel, the MWCS can distinguish between cells staining positive for antibody 1 only, antibody 2 only or antibody 1 and 2.

Automated image analysis with MetaMorph® eliminates the manual measurement bottleneck that has previously dictated the pace and limited the productivity of our research process. Additionally, MetaMorph® removes human variability between measurements. While MetaMorph® is suitable for use by those with no previous image processing experience, it is not a turn-key solution to image analysis. It is absolutely essential that the user takes care to tailor the module settings to the particular images under analysis. Incorrect settings or poor image quality can both result in extensive inaccuracy of the results. Furthermore, those with very specific measurement needs should consider other options as the output measures from MetaMorph® are limited and not customizable.

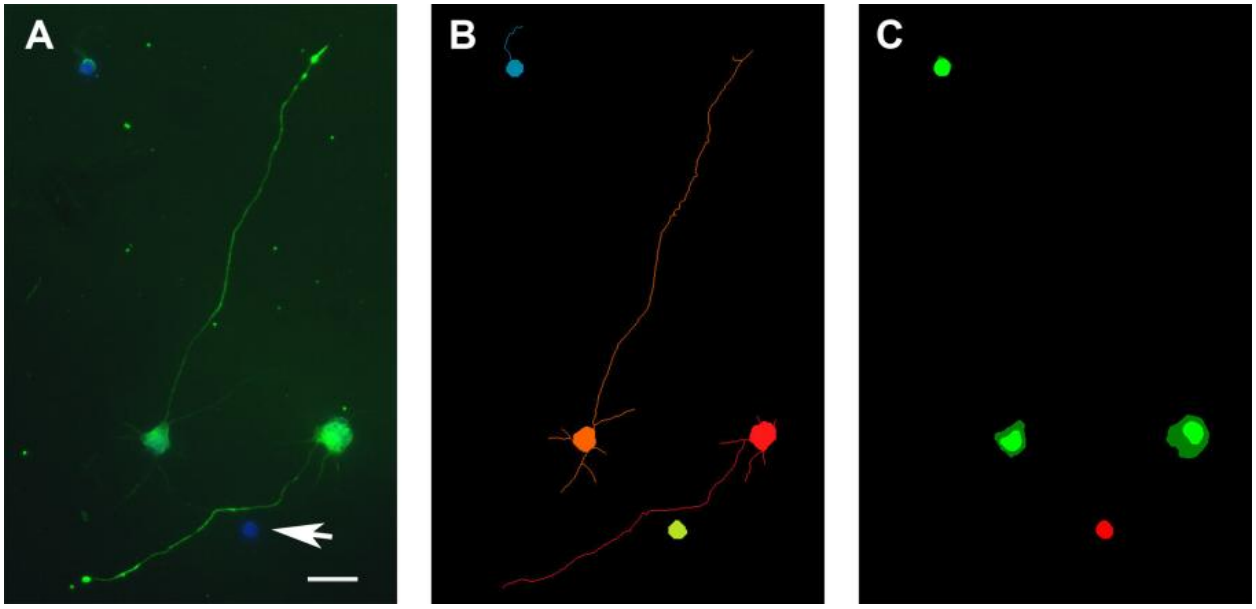


Figure 3.6. Cell scoring.
The cell scoring module in MetaMorph® can be used to analyze a single cell type in a culture with contaminating cells. A.) Fluorescent image of several neurons co-stained with Tuj-1 (green) and DAPI (blue) and a contaminating cell (white arrowhead); B.) output from MetaMorph® neurite outgrowth module – all cells are analyzed; and C.) output from MetaMorph® cell scoring module – the contaminating cell is identified as a negative cell (red) and the neurons are identified as positive (green). Scale bar is 20 µm.

There are a multitude of commercial and independent software tools available for image analysis from which a neuroscientist may choose. Some of these are capable of quite complex branch analysis and image reconstruction for both 2D and/or 3D applications. Excellent reviews by Meijering [129] and Donohue and Ascoli [137] provide an overview of the state of the field. Our decision to develop this methodology using MetaMorph® to perform our image analysis was based solely on the fact that we already had access to both the software and personnel familiar with it. We took advantage of a tool to quantify morphological development of motor neurons in low density culture with software already at hand. Popko and colleagues [133] also demonstrate automated staging of hippocampal neurons, though using data obtained from NeuronJ and post-processed through a JAVA-based algorithm. We encourage other investigators to adapt these methods to their own image processing software of choice, with the hope of allowing more standardization and quantitative result reporting in the field of neuronal morphology.

# Chapter 4. Nanofibers promote Schwann cell migration when proliferation is impaired[138]

Aligned nanofibers topographically direct regenerating neurites in injured peripheral nerve. Schwann cells (SC) are vital to nerve repair and nerve guides seeded with SC promote better regeneration than those without. Because one of the roles of SC in nerve regeneration is topographic guidance, as the bands of Büngner, we hypothesized that nanofibers might similarly facilitate neurite growth if the number of SC was decreased. Aligned nanofibers were electrospun and coated with polylysine. Embryonic day 15 rat dorsal root ganglia (DRG) were cultured on nanofibers for 3 days in defined media, both with and without aphidicolin, which prevented Schwann cell proliferation. The lengths of the longest neurites in each of 10 regions around each DRG were measured. We also measured the position of the SC nucleus farthest along the path of each measured neurite. Total number of SC for each ganglion was counted using an image analysis program. Under normal media conditions, neurite lengths are equal on nanofiber and glass controls. In the presence of aphidicolin, neurite length on nanofibers and glass was also equal. Aphidicolin decreased the number of SC on both nanofibers and glass. Unexpectedly, aphidicolin decreased the distance SC migrated on glass, but had no effect on SC migration on nanofibers. These data suggest that nanofibers may support SC migration even in the setting of reduced Schwann cell number. Even though nanofibers had no effect on neurite length in the setting of

reduced Schwann cells, the ability of nanofibers to support Schwann cell migration suggests they may have an important role in peripheral nerve regeneration scaffolds.

## 4.1 Introduction

It has been clearly established that Schwann cells are critical to peripheral nerve regeneration after injury. Following transection, Schwann cells can be found in both the proximal and distal stumps of the severed nerve, as well as in the intervening space. Regenerating axons proceed from the proximal stump into the gap. While the proximal stump bears much resemblance to intact nerve except near the point of transection, the distal stump is profoundly different. After Wallerian degeneration, in which macrophages remove myelin and axonal debris, Schwann cells proliferate and then extend cytoplasmic processes that act as a scaffold for regenerating axons [139]. In addition to this topographical network called the “bands of Büngner,” Schwann cells exert a chemotactic influence on regenerating axons [140, 141]. Eradication of Schwann cells from nerve grafts by exposure to radiation slows the growth of regenerating axons [142], while irradiating those in the distal stump essentially produces complete regeneration failure [143].

Many nerve guidance channels have been designed to supply the extracellular cues that aid neurite extension and regrowth, including growth factors and/or extracellular matrix (ECM) proteins [37]. However, until recently, topographical cues that further replicate the regenerative microenvironment have not been addressed. The addition of such cues in the form of longitudinally-aligned polymer fibers is a promising new development that may improve regeneration outcomes [47, 144-147]. These fibers

can be produced by electrospinning polymer solutions onto a rapidly rotating wheel [45, 47, 48, 148] or stationary objects [149] that facilitate their alignment. Some of these fibers, possessing diameters from hundreds of nanometers to a few microns, supply topographical information on the cell-length scale, which has a powerful effect via contact guidance for developing and regenerating neurites. When aligned, these fibers have been shown to accelerate neurite growth [45, 80], speed the maturation of neurons [81], and facilitate the development of neuronal precursor cells toward a neuronal phenotype as opposed to a glial phenotype [150, 151]. While neurite growth is increased on aligned nanofibers compared to unaligned nanofibers [45, 47], there have been few comparisons of neurite growth and Schwann cell migration on nanofibers versus planar surfaces [28, 80].

While several studies have demonstrated that elongating neurites and migrating Schwann cells are directed along the nanofibers [45, 47, 48, 148] [149], the interactions among Schwann cells, neurites, and aligned nanofibers have not yet been studied in detail. It is not known whether neurites precede Schwann cell migration on fibers or vice versa. Evidence in the literature is contradictory: on protein-coated microscale fibers, neurites precede Schwann cells [147], but on uncoated nanofibers, migrating Schwann cells lead neurites [47].

The dependence of neurites on Schwann cells may be altered in the presence of nanofibers. Because there are some conditions where Schwann cells are impaired by disease, such as diabetes [152], nanofibers may be a promising regenerative tool. It is also unknown whether neurite migration on nanofibers is impaired when Schwann cell number is reduced. Given the importance of Schwann cells to nerve regeneration, one

would hypothesize that neurite regeneration would suffer if Schwann cells were decreased. However, the affinity of neurites for nanofibers, seen in previous studies, suggests that nanofibers could allow neurites to be less dependent on Schwann cells for outgrowth and directional guidance. If nanofibers were found to improve regeneration in the setting of impaired Schwann cells, it would support their use in nerve guidance channels.

We sought to examine these questions in the present study. First, using embryonic day 15 (E15) rat DRG explants grown in serum-free media, we compared neurite length on polylysine (PLL)-coated glass to that on similarly coated poly-l-lactic acid (PLLA) nanofibers. Second, we measured and compared neurite length to the leading edge of Schwann cell migration. Third, we used aphidicolin, a proliferation inhibitor known to lock cells in S-phase [153-156], to limit the number of Schwann cells and determine if neurite outgrowth would be adversely affected. In light of previous studies, we hypothesized that neurite outgrowth and SC migration would be maximized on nanofibers compared to on glass. Second, we predicted that neurites would precede migrating SC in all cases. Third, we predicted that reducing the number of SC via aphidicolin would reduce neurite outgrowth.

## 4.2 Experimental Procedure

All materials were purchased from Sigma–Aldrich (St. Louis, MO) except where otherwise specified.

### 4.2.1 Electrospinning

Electrospun nanofibers (Figure 4.1) were created as described in previous studies [28, 45, 157]. Briefly, nanofibers were electrospun from a 4 wt% solution of poly-L-lactic acid (PLLA) in chloroform onto poly-lactic-co-glycolic acid (PLGA) coated cover slips. The solution was pumped through a blunt 23ga tip by a syringe pump at a rate of 0.2 ml/hr. The grounded collector wheel was kept 10 cm away from the tip and rotated at 250-300 RPM. A DC voltage of 9 kV was maintained between the tip and the wheel. An SEM of resulting fibers is shown in Figure 4.1A.

### 4.2.2 Substrate preparation

Glass cover slips, used as a control substrate for culture, were cleaned first by sonicating in 20% methanol in water, and, following rinsing, were immersed in a piranha etch (7:3 v/v ratio of 70% sulfuric acid and 30% hydrogen peroxide). Nanofiber substrates were exposed to an air plasma for 2 minutes. In addition to cleaning, these processes served to make the surfaces more wettable. Substrates were coated with PLL (poly-L-lysine) at 10 µg/ml for 1-2 hr and then aspirated dry. The substrates were rinsed and dried three times before use.

### 4.2.3 Primary dorsal root ganglia (DRG) culture

Preparation of primary dorsal root ganglia (DRG) was performed as previously described [28, 45, 158]. Briefly, DRG were plucked from the spinal cords of embryonic day 15 (E15) Sprague-Dawley rats with fine dissection forceps. They were then placed manually on nanofibers or glass substrates in a minimal amount of media to promote

attachment and minimize floating. After one hour to allow for adhesion, more media was added to submerge the DRG explants and substrates completely. DRG were cultured at 37 °C and 5% $CO_2$ for 3 days. Media consisted of Neurobasal (Invitrogen) supplemented with 2% B27 (Invitrogen) with the following additives: 30 nM selenium, 10 nM hydrocortisone, 10 nM beta-estradiol, 10 mg/L apo-transferrin and 1X penicillin/streptomycin/neomycin. L-glutamine (2 µM) was added to culture media immediately before plating. In some cases, the antibiotic aphidicolin (7 µM) was added to prevent proliferation of Schwann cells.

### 4.2.4 Immunocytochemistry

DRG explants were fixed in 4% paraformaldehyde at 37°C for 30 minutes. A solution containing 1.25% bovine serum albumin and 1% normal goat serum was applied for 30 minutes to prevent non-specific antibody binding; the solution also contained 0.05% Triton X-100 to permeabilize cell membranes. Rabbit anti-neurofilament (NFL) (Chemicon, Temecula, CA) at 1:1000 and mouse anti-S-100 at 1:250 were diluted in the blocking and permeabilization solution and applied overnight at room temperature. Secondary antibodies were goat anti-mouse rhodamine at 1:200 for S-100 and goat anti-rabbit Oregon Green at 1:200 for NFL. Samples were incubated with the secondary antibody for 4 hours at room temperature. The samples were then mounted with Prolong Gold (Invitrogen) containing the nuclear counter stain DAPI.

### 4.2.5 Image acquisition and analysis

A Leica MXFL III stereo fluorescent microscope was used to obtain digital images of the stained DRG. Green images depicting neurites, red images depicting

Schwann cells, and blue images of nuclei were collected. Measurements were taken using the image analysis software MetaMorph® (Molecular Devices, Downingtown, PA). The longest neurite from each of 10 roughly equal sections around the circumference of each ganglion was chosen by visual inspection and measured. Each neurite was traced along its entire length from the perimeter of the ganglion to the end of its growth cone. The distance of Schwann cell migration was determined by measuring the distance between the perimeter of the ganglion to the Schwann cell nucleus farthest away from the ganglion along each measured neurite. At least seven ganglia were measured for every condition.

### 4.2.6 Schwann cell quantification

To count Schwann cells, images were imported into MATLAB (Mathworks, Natick, MA). Each image was cropped to contain only the ganglion with its extending neurites and Schwann cells and then separated by color channel. The blue channel image, which showed nuclei of cells that had migrated out from the ganglion (which correlated with the red s100-stained cells, identified as Schwann cells), was converted to binary and morphologically opened. (“Morphological opening” is an image processing term that describes processing of a binary image. It consists of “erosion” of that image followed by “dilation” of the eroded image, which essentially smoothes boundaries and reduces small outward bumps and small narrow openings.) The ganglion itself, and all the cell bodies it contained, were excluded from the count. Functions from the MATLAB image processing toolbox (bwlabel and regionprops) were then used to count the number of regions in the image, each one of which corresponded to an individual SC. A manual selection process was used to exclude artifacts and debris from the count.

Some samples were counted manually to verify the accuracy of the automated MATLAB counting algorithm.

### 4.2.7 Statistical Analysis

All statistical analysis was performed in Prism 5.0 (GraphPad, La Jolla, CA). Student's t-test was used to determine significance. P-values less than 0.01 were considered statistically significant.

## 4.3 Results

Dorsal root ganglia explants from E15 rats were grown on electrospun nanofibers [28] and flat glass substrates. The explants were cultured both in the absence and the presence of aphidicolin, a chemical known to impair SC proliferation. Representative examples of DRG grown with or without SC impairment on the substrates are shown in Figure 4.1.

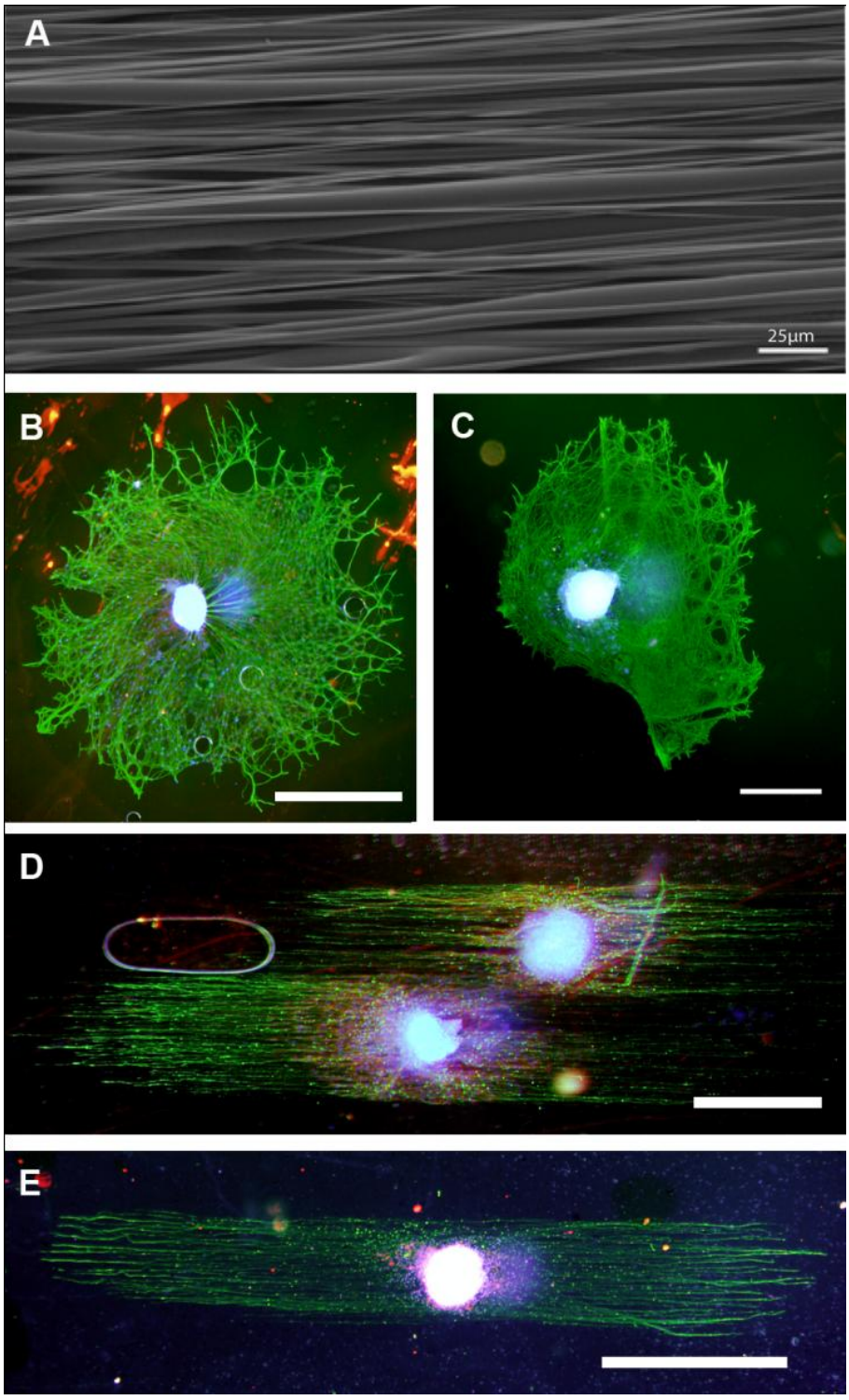


Figure 4.1. Nanofibers and DRG explants.
Nanofibers were produced by electrospinning, shown in a scanning electron micrograph (A). Dorsal root ganglia were grown on glass both without (B) and with (C) aphidicolin. DRG were also cultured on fibers without (D) and with (E) aphidicolin. Scale bars in B through E are 1mm.

### 4.3.1 DRG neurite length is equal on nanofibers and glass

We first compared the growth of DRG neurites on PLLA nanofibers to those on glass (Figure 4.2) under normal media conditions (without aphidicolin). Based on previous studies [45], we hypothesized that neurites would grow longer on nanofibers than on glass. Surprisingly, there was not a statistically significant difference in the lengths of neurites from DRG grown on nanofibers compared to glass.

### 4.3.2 DRG neurites are longer than the leading edge of Schwann cell migration on nanofibers and glass

In order to characterize the relationship between SC migration and neurite extension, we looked at Schwann cell migration in relation to neurite length on both glass and aligned PLLA nanofibers. We compared the distance of the SC that migrated the farthest along the same path of each measured neurite to the length of that neurite. In very few instances did a Schwann cell migrate farther than its corresponding neurite had grown. The mean neurite length and mean SC migration distance along each neurite is shown in Figure 4.3. Though neurites lead SC on both fibers and glass, SC migration did not differ statistically from neurite length on either substrate when grown in normal media.

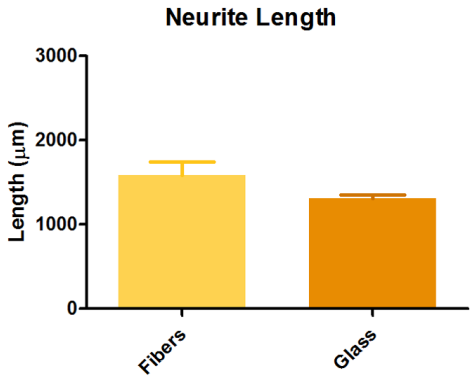


Figure 4.2. DRG neurites are equal on nanofibers and glass.
DRG were grown for 3 days in serum-free media on glass or aligned nanofibers. Each explant was divided into 10 regions and the longest neurite from each region was measured from the tip back to the body of the ganglion. There was no significant difference in neurite length between in the plus aphidicolin condition and the normal media condition (without aphidicolin). Error bars show standard error.

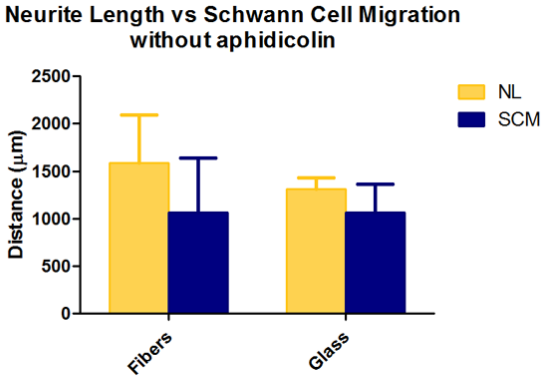


Figure 4.3. Elongating neurites lead Schwann cells on both fibers and glass.
The distances Schwann cells migrated along the neurites measured previously were traced and measured. On both glass and nanofibers, neurites were longer than the distance that Schwann cells migrated along them although this difference was not statistically significant in either case. Interestingly, the Schwann cell migration distances were nearly identical on nanofibers (1063 ± 166) and glass (1066 ± 100um).

### 4.3.3 Aphidicolin reduces the number of Schwann cells on nanofibers and on glass

To further examine the relationship between Schwann cell migration and neurite extension, we attempted to reduce SC number by adding aphidicolin to the media. Aphidicolin is an antibiotic that reversibly stops cell proliferation in S-phase [154, 156]. Both on glass and on nanofibers, aphidicolin significantly reduced the number of Schwann cells. The effect of aphidicolin on SC numbers can be seen in Figure 4.4.

### 4.3.4 Aphidicolin reduces the migration of Schwann cells on glass but not on nanofibers

We did not expect that using aphidicolin to decrease the number of Schwann cells would adversely affect the distance Schwann cells migrated. Aphidicolin significantly decreased the distance Schwann cells migrated on glass ($p<0.01$). Surprisingly, no such decrease was observed on nanofibers (Figure 4.5).

### 4.3.5 Aphidicolin does not reduce neurite length on glass or nanofibers

Because nanofibers exert a strong contact guidance cue on elongating neurites, we hypothesized that contact guidance from SC would be less necessary for neurite growth in the presence of nanofibers. Therefore, reducing the number of SC with aphidicolin should be less deleterious to neurite outgrowth on nanofibers than on glass, which lacks additional topographic guidance cues. However, we found that reducing Schwann cell number had no deleterious effects on neurite length (Figure 4.6).

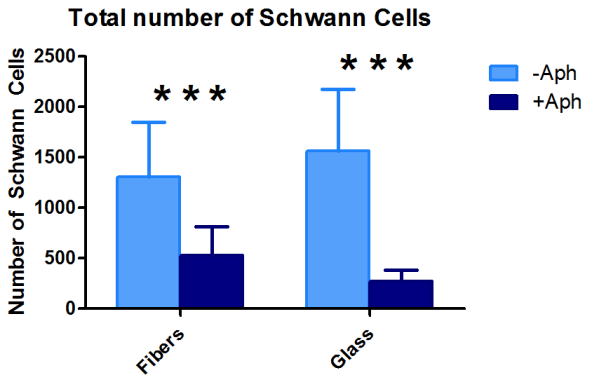


Figure 4.4. Aphidicolin reduces the number of Schwann cells.
DRG were grown on PLL coated glass or nanofibers in media with or without 7 µM aphidicolin. Dramatic reductions in the number of Schwann cells were observed upon addition of aphidicolin. The percent reduction in the number of Schwann cells on nanofibers was less than the reduction on glass (***p<0.001).

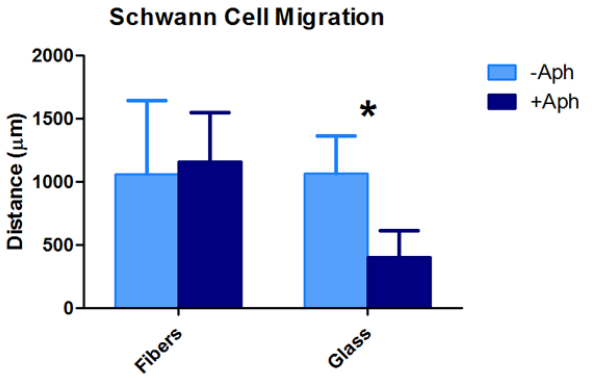


Figure 4.5. Aphidicolin reduces Schwann cell migration on glass.
Schwann cell migration distance was significantly reduced in aphidicolin on glass substrates, but not fibers.

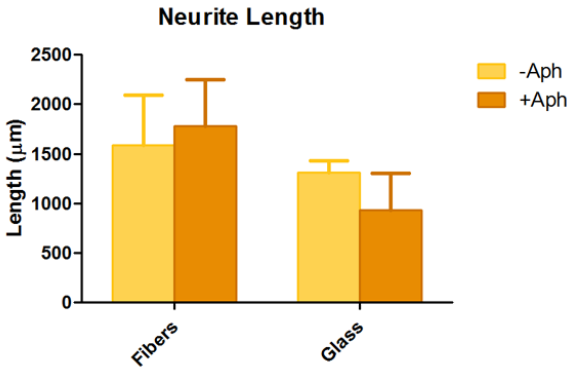


Figure 4.6. Aphidicolin reduces neurite outgrowth on glass but not on nanofibers.
However, no significance was seen in either condition.

## 4.4 Discussion

Aligned electrospun nanofibers clearly guide neurites in the direction of nanofiber alignment, both *in vitro* [28, 45, 47, 48, 81, 149, 151] and *in vivo* [47, 148]. The interactions between Schwann cells, neurites and nanofibers, however, need further study. The experiment presented here is an attempt to help answer several key questions suggested by previous studies. For the most part, the findings have been unexpected.

Because Schwann cells are so crucial to neurite extension in peripheral nerve regeneration, we asked how neurite length would be affected if the number of Schwann cells was reduced using the proliferation inhibitor aphidicolin. We found that, in addition to reducing Schwann cell number, aphidicolin reduced the migration of Schwann cells on glass. On nanofiber substrates however, Schwann cell migration was not reduced by aphidicolin.

### 4.4.1 Neurite outgrowth as a function of topography

We first considered the effect of topography on neurite outgrowth. Neurite outgrowth on glass was not statistically different than that on nanofibers. This was an unexpected result because we hypothesized the greater surface area of the nanofibers would stimulate greater neurite elongation. Wen and Tresco, working with microscale fibers, found that the smallest microfibers (5 µm in diameter) produced the best neurite outgrowth, which they postulated was due to the very high surface area of 5 µm fibers [147]. However, additional studies have indicated that there may be an optimal fiber diameter to promote neurite outgrowth and Schwann cell migration. Gilbert and

colleagues, working with nanoscale fibers, found that the largest nanofibers (1300 nm in diameter) produced neurite outgrowth superior to that on 800 nm or 300 nm diameter fibers. This suggests that fibers with diameters on the cell length scale promote the greatest outgrowth. In our study, the nanofibers were 600-700 nm in diameter. This may have been too small for optimal outgrowth. Fiber diameter is an important consideration for nerve regeneration scaffolds, given that scaffolds containing nanofibers have been found to be superior compared to those without [148, 159].

### 4.4.2 Neurites lead Schwann cells on glass and nanofibers

Another goal of these experiments was to determine the position of Schwann cells with respect to the leading edge of neurite growth as SC migrate away from the explants. We found that neurites migrated slightly ahead of Schwann cells on both glass and nanofibers though the differences were not statistically significant. Our results may be specific to sensory neurons on nanofibers in serum-free media. Published data have been conflicting. Wen and Tresco found that growth cones of regenerating neurites preceded migrating Schwann cells on microfibers (5 µm diameter) coated with extracellular matrix (ECM) proteins [147]. The experiments of Kim and colleagues using DRG explants on nanofibers in serum showed that Schwann cell migration preceded elongating neurites [47]. Both groups used serum in the growth media, which may have altered adhesion and growth of DRG neurites and migration of Schwann cells. Therefore, this limits comparisons of our results with those of Wen [147] and Kim [47].

### 4.4.3 Schwann cell and neurite behavior in aphidicolin

Aphidicolin clearly decreased the number of Schwann cells observed on both nanofibers and glass (Figure 4.4). This result was expected and is consistent with the effects of aphidicolin on Schwann cells reported in other studies [153, 160] as well as effects seen on other cell types [154, 155, 161-163]. Completely surprising was the effect of aphidicolin in decreasing the migration of SC on glass but not on nanofibers. A previous study found that aphidicolin had no effect on Schwann cell migration [164]. Only a few studies show that aphidicolin has an effect on the migration of other cells. Aphidicolin has been found to decrease cell movement during the formation of the primitive streak in chick embryos [153]. Hepatoma cells in an *in vitro* cancer cell assay migrate less when they are locked in S-phase by aphidicolin but increase their migration after it is withdrawn, suggesting that its effects on migration are cell-cycle dependent [154]. However, aphidicolin does not affect the migration of fibroblasts [161] or osteoblastic cells [162] *in vitro*. It also does not affect the migration of epithelial cell lines through porous membranes [163], the chain formation of neuronal precursor cells [155], or the migration of SC in embryos [160]. Aphidicolin may temporarily reduce SC motility until the mitosis cycle is complete. Whether aphidicolin somehow affects the cytoskeleton is unknown. The reduced SC migration may also have been a direct result of the decrease in SC number. Schwann cells migration in the presence of aphidicolin has not been previously studied. If the aphidicolin does, however, impair both proliferation and migration of SC, then it can be used to create a model for nerve regeneration in diabetes patients. These results indicate a need for further investigation into the actions of aphidicolin on Schwann cell proliferation and migration.

The decrease in Schwann cell migration observed on glass was not seen on nanofibers, despite the clear decrease in Schwann cell number on both substrates. The purpose of adding aphidicolin was to decrease Schwann cell number and examine whether neurites still elongated along the nanofibers. However, we did not observe any effects of aphidicolin on neurite length on either substrate. One potential explanation for the unaffected migration of SC on nanofibers is that changing the shape of cells using the topographical features of nanofibers can influence cell migration, as do the bands of Büngner. We have observed that SC are narrow on electrospun nanofibers compared to those on glass (data not shown). It has been shown that cells narrowed by the structure of the surrounding ECM migrate more than those that are not narrowed [165]. It has also been shown that while narrowed cells migrate, this migration ceases when they reach a wider area that no longer results in cell narrowing [166]. These results are consistent with the findings of Chen and colleagues that the shape of the ECM affects cell behavior [167]. These data suggest that narrowing SC on nanofibers may negate the deleterious effects of aphidicolin on Schwann cell migration.

It is important to consider that aphidicolin may have a variety of unknown effects on SC which may contribute to these results. The clustering of integrins has been shown to result in nuclear signaling events through c linkages of the cytoskeleton [168, 169]. The cell skeleton plays an integral role in both migration and the normal progression through the cell cycle. By arresting SC in S phase, aphidicolin may change the migration ability of SC. Since the cell skeleton is responsible for mechanotransduction, the arrest in S-phase likely diminishes gene expression and

thereby restricts the production of actin and other cytoskeletal proteins required for migration.

### 4.4.4 Conclusion

The ability to produce aligned polymer nanofibers that convey topographical contact guidance cues for nerve regeneration applications has been stimulating to both the materials science and clinical neuroscience communities, but their advantages and limits are not yet fully understood. The topographical arrangement of the fibers resembles the longitudinal arrangement of the endoneurium in autologous nerve grafts. Autologous nerve grafts work very successfully but also contain Schwann cells that secrete growth factors and laminin which may be critical to the success of peripheral nerve regeneration [66, 170]. Schwann cell-seeded scaffolds show promising results; however, the ability to obtain a high volume of autologous Schwann cells in a clinical situation is problematic and thus limits this approach. Our data suggest that nanofibers support SC migration even in the setting of reduced Schwann cell number. Although nanofibers do not increase neurite length, they may be an advantageous component of scaffolds for peripheral nerve regeneration. Incorporating aligned nanofibers into nerve regeneration scaffolds may help to abrogate a shortage of Schwann cells in certain clinical applications.

# Chapter 5. Chemically modified fibers: *In vitro* studies

Having developed and validated the suitability of an *in vitro* model of peripheral nerve regeneration, various candidate materials for an *in vivo* nerve guide were investigated. Fibers were modified with laminin, an extracellular matrix protein, or its bioactive peptides, to mimic the natural microenvironment of nerve *in vivo*. This chapter explores three methods of modifying electrospun PLLA fibers with laminin – adsorption, physical blending, and covalent binding of the laminin peptide fragment IKVAV. Physical blending was found to be an impractical method. When adsorbed to the surface, laminin did result in an increase in neurite extension compared to controls. However, the covalent modification of the fiber surface with the laminin peptide fragment IKVAV promoted much more extension due to the increase in surface density of IKVAV binding sites . Based on these *in vitro* results, IKVAV-bound PLLA fibers were selected as a candidate for further evaluation *in vivo* using a rat model of peripheral nerve injury (Chapter 6).

## 5.1 Introduction

Electrospun fibers have been repeatedly shown to direct the extension of regenerating neurites [32, 48, 81]. The alignment of electrospun fibers replicates the topographical guidance provided by Schwann cells (SC) in the bands of Büngner. However, SC provide chemical cues in addition to topographical guidance. In this study,

we evaluated the use of an extracellular matrix protein in conjunction with electrospun fibers for nerve regeneration. Laminin has been shown to be a potent stimulator of neurite outgrowth and is produced by SC in the distal stump following nerve injury. Typically, extracellular matrix proteins are adsorbed onto biomaterials. However, laminin is a large and complex protein, and there is concern that adsorption might change the tertiary structure of the protein, or that the laminin might desorb over time in *vivo*. Therefore, we compared fibers with adsorbed laminin to those spun with laminin physically mixed into the polymer solution before electrospinning. We also took one of the functional peptide sequences of laminin, IKVAV, and covalently bound it to the surface of electrospun fibers. These three methods of fiber modification with laminin were compared *in vitro* to determine which coating resulted in the most neurite outgrowth.

## 5.2 Materials and Methods

### 5.2.1 Electrospinning

Nanofibers were electrospun from a 4 wt% PLLA solution in 9:1 chloroform:DMF at a distance of 20 cm and 25 kV as described in Chapter 2. The fibers were spun onto solvent cast films of PCL on glass cover slips.

### 5.2.2 Cell culture

Motor neurons were isolated from E15 Sprague-Daley rats as previously described [28, 135, 158]. Briefly, timed-pregnant rats were obtained from Harlan, anesthetized with ketamine and euthanized via intracardiac injection of sodium

pentobarbital. Embryos were removed from the uterus and decapitated. Spinal cords were dissected from the embryos and stripped of all membranes. Cords were roughly chopped, then incubated with Trypsin for 20 minutes before manual trituration with a fire polished Pasteur pipette. Motor neurons were isolated by centrifuging the cell suspension over a 9% Optiprep gradient in L15 at 2000 RPM for 15 minutes. Cells were counted by Trypan blue exclusion and plated at a density of 5000 cells per substrate. Media consisted of Neurobasal supplemented with B-27 and various additives [81].

### 5.2.3 Adsorption

Electrospun fibers and glass controls were coated in protein prior to cell culture. The substrates were covered in an aqueous protein solution for at least one hour and then excess solution was aspirated until the substrates were dry. Protein coating solutions were PLL (poly-L-lysine) (100 µg/ mL) and laminin (25 µg/ mL). In the case of PLL coating, substrates were rinsed in sterile water and dried twice following the initial coating. Laminin samples were pre-coated with PLL to increase laminin adsorption.

### 5.2.4 Blending

Blended PLLA and laminin fibers were produced by dissolving 6 wt% PLLA and 0.024 wt% laminin in hexafluoropropanol (HFP). This solution was electrospun at a rate of 0.67 ml/hr at a distance of 25 cm and a voltage of 18 kV.

### 5.2.5 Covalent binding

The PLLA fibers were plasma etched with pure oxygen for 2 minutes at 90 watts. Amine reactive esters were then prepared as follows: Fibers were placed in a buffer

solution composed of 0.1M MES and 0.1M NaCl in distilled water (solution pH 5.5). EDC and NHS were then added to the buffer at a 2:1 molar ratio to a final concentration of 25 mM and 12.5 mM, respectively. The solution was gently stirred for 1 hr and then the fibers were washed to remove residual EDC and NHS. After washing, the fibers were placed in 1.5 ml of fresh buffer each and the pH was adjusted to 8 by dropwise addition of 1 M NaOH.

The laminin peptide IKVAV was then bound to the fibers. The peptide was added to the buffer solution for a total peptide weight of 40 ug per fiber sample. The fibers were incubated in the peptide solution for 18 hrs at 4°C with gentle shaking. They were then briefly rinsed with distilled water and placed in fresh buffer solution (pH 5.5) for 48 hrs at 4°C to allow any non-covalently bound peptide to desorb from the fiber surface. The buffer solution was changed once at 24 hrs.

### 5.2.6 Cell staining and analysis

Cells were fixed at 1 and 3 days post-plating for 30 minutes in 4% paraformaldehyde. The samples were then incubated for 30 minutes in a blocking and permeabilization solution consisting for 1.25% bovine serum albumin, 0.05% Triton X-100 and 2% normal goat serum. The samples were then incubated with anti-beta-tubulin overnight, then rinsed and incubated with secondary antibody for four hours. Cells were mounted using Prolong Gold containing the nuclear counterstain DAPI. The samples were then imaged on an EVOS fluorescent microscope at 20X. The images were then analyzed with MetaMorph imaging software as previously described [91] in Chapter 1.

### 5.2.7 X-ray photoelectron microscopy

X-ray photoelectron microscopy (XPS) was performed using a Kratos Axis Ultra XPS with a monochromatic Al x-ray source. A 900 x 900 μm area was analyzed. The surface ratios of N/C were then calculated.

## 5.3 Results

### 5.3.1 Blended PLLA/laminin fibers

The amount of laminin present on the surface of the blended fibers tended to vary considerably between trials (data not shown). This is likely due to non-uniform mixing in the electrospinning solution. In order to ensure a high surface concentration of laminin, the amount of protein blended into the solution would have to be greatly increased, which would negatively affect the ease of electrospinning the solution. In addition, such a drastic increase in laminin concentration was not economically justifiable. Thus, blended laminin fibers were excluded from further consideration.

### 5.3.2 Adsorption versus covalent binding

X-ray photoelectron spectroscopy confirmed that both physical adsorption of laminin and chemical binding of IKVAV were successful (Table 1). The nitrogen content of the fibers increased dramatically under both cases, indicating the presence of protein. While the concentration of nitrogen is less on the IKVAV-bound samples than on the adsorbed laminin samples, it should be noted that 40 μg of protein were applied in both cases. Whole laminin is a very large protein, with only one IKVAV sequence per protein.

Thus, the IKVAV-bound samples posses many more functional IKVAV binding sites per unit surface area, despite having a lower nitrogen concentration.

Even a cursory inspection of the morphology of motor neurons cultured on the two surfaces indicates that the IKVAV-bound fibers vastly outperform the adsorbed laminin Figure 5.1. Again, this is likely due to the increased surface density of functional sites on the IKVAV-bound fibers.

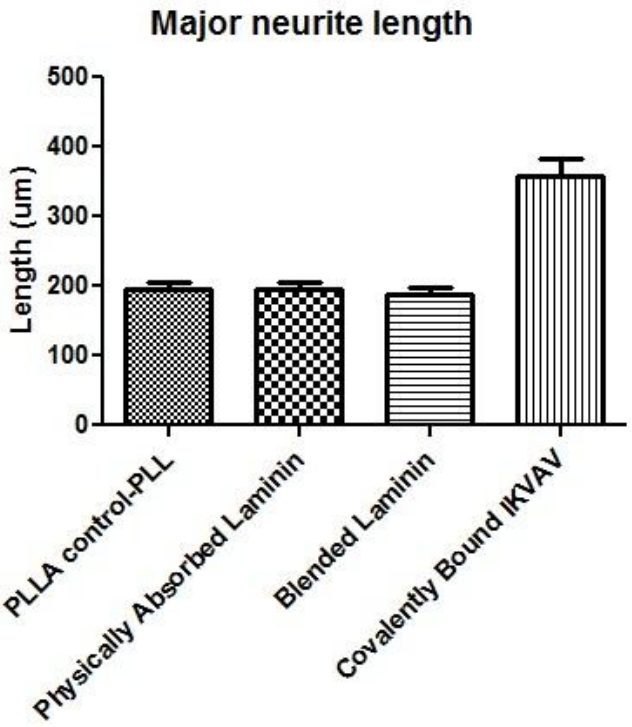


Figure 5.1. Major neurite length on fibers at 3 DIV.

Comparing the morphology of motor neurons cultured on IKVAV-bound fibers and films to poly-L-lysine (PLL) coated fibers and films further demonstrates the fact that the IKVAV-peptides are functionally intact following the covalent binding procedure (Figure 5.2). PLL is a protein which improves motor neuron adhesion but does not elicit an integrin response. The binding of IKVAV to cell surface integrins receptors is known to result in an increase in neurite outgrowth [68]

| Sample | Atomic concentration (%) | | |
|---|---|---|---|
| | Carbon | Oxygen | Nitrogen |
| PLLA fiber | 65.57 | 34.02 | 0.41 |
| PLLA fiber + plasma treatment | 63.45 | 36.30 | 0.25 |
| PLLA fiber + whole laminin | 56.92 | 37.63 | 5.45 |
| PLLA fiber + covalently bound IKVAV peptide | 54.49 | 41.79 | 3.72 |

Table 1. Nitrogen quantification by XPS indicates protein is present.

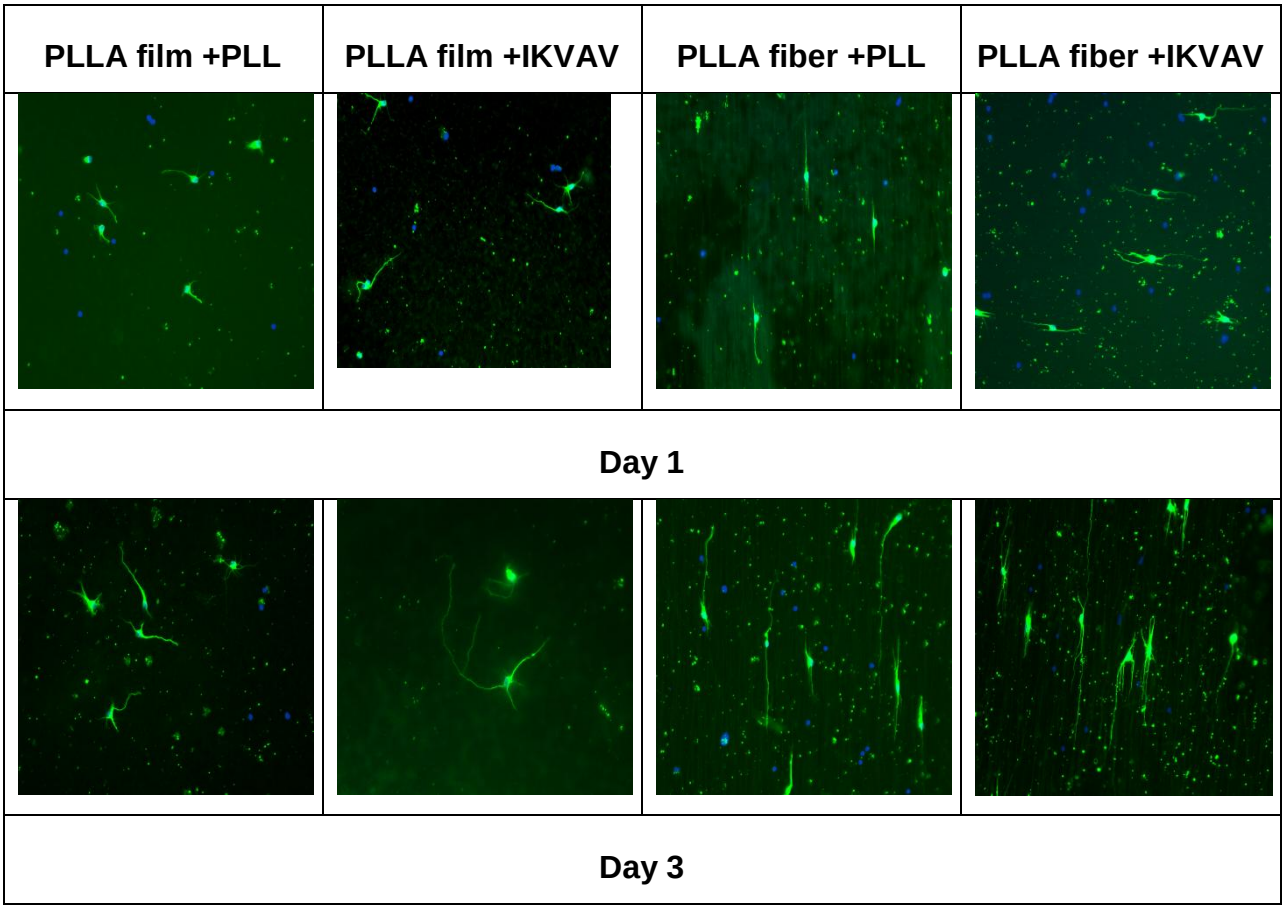


Figure 5.2. Representative motor neurons.
Motor neurons were cultured for 1 and 3 days on film and fiber PLLA substrates modified with IKVAV. PLL coated films and fibers served as controls. Significant lengthening of neurites is apparent on IKVAV-bound surfaces. This lengthening is more pronounced after three days in culture.

Additionally, the major neurites of motor neurons on IKVAV-bound fibers are longer than those on IKVAV-bound films at three days (Figure 5.3), as are the mean neurite lengths (Figure 5.4). This is expected given our previous experience that electrospun fibers not only orient neurites but result in faster motor neuron maturation than films [81].

The average number of neurites per cell is slightly decreased on fibers than on flat surfaces (Figure 5.5). This is also expected. Motor neurons on fiber surfaces tend to develop unipolar or bipolar morphologies, while those on flat surfaces are multipolar [81]. There is no difference in the number of neurites of the motor neurons on the PLL coated surfaces versus the IKVAV-bound surfaces at three days, which is also expected based on the literature [68]

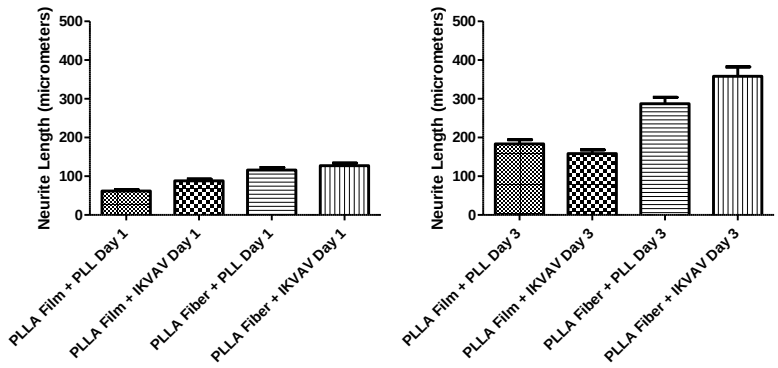


Figure 5.3. Major neurite length at 1 and 3 days.
Axons are longer on fibers than on films due to enhanced maturation on fibers. Also, IKVAV binding results in longer axons, which is most apparent after 3 days in culture.

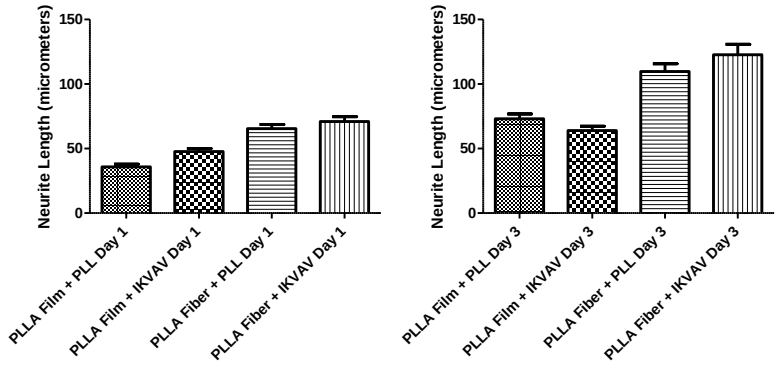


Figure 5.4. Mean neurite length at 1 and 3 days.
Mean neurite length is also increased on fibers and IKVAV samples versus films and PLL coated samples.

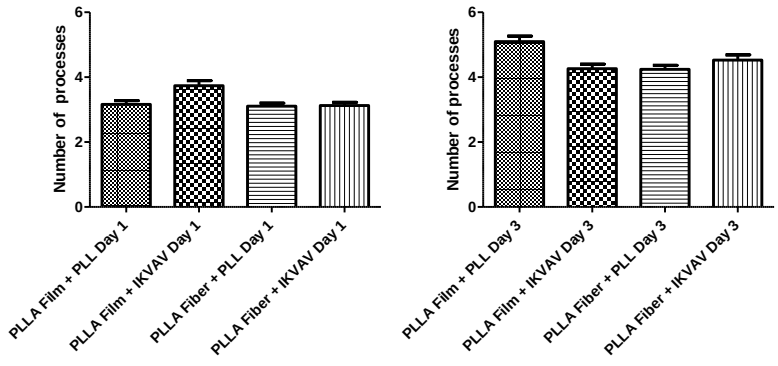


Figure 5.5. Mean number of processes per cell.
While number of processes is slightly decreased on fibers, these differences are gone after three days in culture. IKVAV does not affect number of processes.

## 5.4 Discussion and conclusions

Schwann cells are the key players in peripheral nerve regeneration. Following injury, SC remove axonal debris, express adhesion molecules, secrete growth factors, lay down laminin, and provide topographical guidance by arranging into the bands of Büngner. We have previously shown that electrospun nanofibers can provide the topographical guidance to regenerating neurites in lieu of SC. Here, we investigated three methods of modifying the electrospun fibers with laminin in an attempt to further replicate SC function within an artificial nerve conduit.

Of the three methods investigated, physical blending proved to be impractical. Adsorption is the current standard of practice in biomaterial coatings. However, adsorption of whole laminin presents several problems. Laminin is a large protein and is likely to suffer cleavage by proteases *in vivo* and may in fact desorb over time. By instead covalently binding a protein to the surface, desorption is prevented. By using a small peptide fragment, the action of proteases is limited. Additionally, the small size of the peptide fragment allows for a much higher surface density of active sites, which increases the number of integrins that each regenerating neurite has bound, in turn increasing the signal to the neuron. Indeed, motor neurons on IKVAV-PLLA nanofibers outperformed all other samples. Based on these results, we will move forward with *in vivo* testing of IKVAV-PLLA nanofibers in a small rodent model of peripheral nerve regeneration (Chapter 6).

# 6. Chemically modified fibers: *In vivo* studies

Aligned electrospun nanofibers are ideal components of artificial nerve guidance channels. To improve regeneration efficacy, these nanofibers should be coated in an extracellular matrix protein chosen to mimic the natural microenvironment of the nerve. During regeneration, Schwann cells proliferate and deposit laminin, which promotes regenerating neurite extension. In the previous chapter, three methods of incorporating laminin into electrospun fiber nerve conduits, physical adsorption, blending and covalent modification, were analyzed *in vitro*. The results demonstrated that PLLA fibers covalently modified with the laminin peptide IKVAV vastly outperformed the other methods. In this chapter, the IKVAV-PLLA fibers were placed in a polysulfone tube and implanted into a rat model of peripheral nerve injury. Unmodified PLLA fibers and empty polysulfone tube grafts served as negative controls. Autografts were performed as a positive control. Preliminary results indicate that IKVAV-PLLA fibers clearly outperform the negative controls, yet still vastly underperform autografts. Thus, there may be some limited clinical use for IKVAV-PLLA nanofiber conduits in situations where insufficient donor nerve is available for autograft.

## 6.1 Introduction

Peripheral nerve regeneration can be investigated in rats. Typically, a segment of sciatic nerve is removed from the leg and replaced with the material under investigation.

The sciatic nerve is of sufficient size to be easily handled by the surgeon (diameter 1.4 ± 0.35 mm [171]) and a 2 cm length of unbranched nerve is available. The animal is allowed to recover for 1 month to 1 year following surgery. During recovery, the extent of regeneration can be gauged by nerve conduction velocity tests or by examining the ability of the animal to walk a grid and/or maintain proper posture while walking. Following explantation, a variety of histological techniques are available to identify regenerated axons.

Some successes with nerve regeneration in rats have been reported. Bellamkonda bridged a 17 mm sciatic nerve gap with PAN-MA electrospun fibers [47]. Gelain showed successful regeneration across a 10 mm gap using PLGA/PCL electrospun fibers [172]. Ramakrishna also successfully bridged a 10 mm gap using electrospun PLGA fibers in five of eleven animals at one month post implantation [173]. However, these relatively short gaps are not a rigorous test of regeneration given the extreme length of nerve gaps in real clinical cases. There is still a need for an artificial nerve conduit that can support regeneration over long distances.

## 6.2 Materials and methods

### 6.2.6 Conduit preparation

Films were prepared by casting 6 wt% PCL in chloroform onto glass covers lips. The PCL films were allowed to dry at room temperature. PLLA fibers were then spun on the films and chemically modified with IKVAV as previously described in Chapter 5. The films bearing the fibers were then removed from the glass slides by brief immersion in ethanol and trimmed to a width of 1.5 mm and a length of 1.2 cm. Four of these fiber

sheets were stacked on top of one another. A polysulfone conduit with a 1.5 mm inner diameter and a molecular weight cut off of 50 kDa was cut to a length of 1.4 cm (slightly longer than the nerve gap size of 1.2 cm to allow the conduit to overlap the nerve stumps for secure suturing). The pore size of the conduit (50 kDa) was selected based on the findings of Aebischer and colleagues, who determined the optimal molecular weight cut off for peripheral nerve regeneration to be 50 kDa [174].Vacuum suction was applied gently to one end of the conduit as the stack of films was introduced to the other end. The films were sucked into the conduit and when released, separated slightly to fill the lumen of the conduit. No glue was applied – the conduit walls gripped the films sufficiently to prevent movement.

### 6.2.7 Surgery

All animal procedures were performed with the approval of the VA Animal Care and Ethics Committee and in accordance with the National Institutes of Health guidelines for animal survival surgery.

Adult male Lewis rats (200g minimum) were selected because this strain does not commonly self-mutilate following surgery. Anesthesia was induced with inhaled 3.5-4% isoflurane diluted in pure oxygen. Anesthesia was maintained with inhaled isoflurane at 2-2.5%. Animal body temperature was maintained at 37°C by a warming pad. Depth of anesthesia was monitored by observation of breath rate and response to toe-pinch. Peri-operative analgesia was administered via intramuscular injection of buprenorphine at 0.01-0.05 mg/kg to minimize post-operative pain. The animal’s eyes were covered with Perilube eye ointment to prevent drying. The surgical site was

prepared by shaving, washing in sterile water, repeated scrubbing with betadine and then sterilely draped.

An incision was made through the skin, beginning a finger width posterior to the femur head and ending distally a finger width posterior to the knee along the calf. The skin was then bluntly dissected away from the underlying musculature. Sterile gauze and saline irrigation was used to keep exposed tissues moist and to clear any obstructive bleeding. Next, the biceps femoris was divided along the fascial plane to expose the sciatic nerve. The muscle division was held open with a retractor and further enlarged until the entire length of the sciatic nerve between the pelvis and knee was exposed.

An operative microscope was used during the next steps of the surgery. The sciatic nerve was isolated and separated from the surrounding connective tissue using super fine tip microforceps. Great care was taken to minimize damage to the nerve, which was handled only by the epineurium. For the remainder of the surgery, the exposed nerve (Figure 6.1) was irrigated with sterile saline every 5 minutes to prevent it from drying out. The desired length of nerve to be removed was measured and marked with a surgical marker. The sciatic nerve was transected with Vannas scissors and removed. The conduit was situated between the nerve stumps and suture sites were marked at 0.5 mm from the ends of the nerve stumps. The conduit was also marked at 0.5 mm on each end. The conduit was first sutured to the proximal nerve stump and then to the distal nerve stump with 9-0 Ethilon suture. Sutures were placed through the epineurium and the polysulfone conduit wall so that the conduit overlapped the ends of the nerve stumps slightly. Only one suture was placed at each end, to minimize damage

to the nerve stumps. Sutures were tied with no more than two knots to prevent scar tissue formation and the ends of the suture were closely clipped. In the case of autograft, the segment of sciatic nerve removed was simply sutured back into place in reverse orientation. No conduit was used.

After sutures were in place, the implantation site was irrigated and the retractor removed. The overlaying gluteal musculature was replaced and secured with a running stitch using 4-0 silk suture. The skin was closed with 4-0 Ethilon suture. The exterior of the wound was washed with sterile saline. Fluids were administered sub-cutaneously and anesthesia was withdrawn. The animal was monitored on the warming pad until ambulatory and then returned to caging. Food was provided at floor level for the first day in case the animal was unwilling to lift itself to the cage ceiling feeder. Analgesia was provided for a minimum of three days post-operatively. Animals were monitored daily until sutures were removed (approximately 10 days). All animals survived the surgery.

### 6.2.8 Nerve conduction velocity

Initially, nerve conduction velocity (NCV) tests were conducted transdermally monthly following conduit implantation. However, this resulted in frequent infection at the electrode placement sites. Further NCV testing was limited to once per animal, under anesthesia during the explant procedure.

### 6.2.9 Histology

For the explantation procedure, the animal was placed under isoflurane anesthesia, a NCV reading was obtained and then the animal was perfused with 2%

paraformaldehyde. The nerve was then cut above and below the conduit and placed in 4% paraformaldehyde overnight. The explant was then dehydrated through a graded ethanol series and then through a paraffin tissue processor. The samples were then embedded in paraffin blocks and 5 μm microtome cross-sections were obtained. Sections were dewaxed with xylene and then rehydrated through a graded ethanol series. The polysulfone conduits survived the paraffin embedding process, but the electrospun fibers and support films did not, due to their solubility in xylene. Some sections were stained with hematoxyline and eosin (H&E) and examined with a Leica light microscope. Other sections were immunostained with anti-beta-tubulin and anti-S-100 and examined with an EVOS fluorescent microscope.

## 6.3 Results and discussion

### 6.3.1 Early complications

Initially, the study design called for nerve conduction velocity (NCV) recordings to occur monthly following implantation. However, we found that while the rats did not chew on their paralyzed leg, they did tend to lick it quite a lot. This led to constant infection in the wounds caused by the NCV recording electrodes in the ankle region. Antibiotic creams and ‘liquid skin’ products did not improve the situation. Eventually the infection would create an ulcer (Figure 6.2), and then spread into the calf muscle which would atrophy, leaving no target for the regenerating nerve. Rather than subject the rats to daily antibiotic administration, the decision was made to limit the NCV recordings to once, immediately prior to explantation, for future animals.

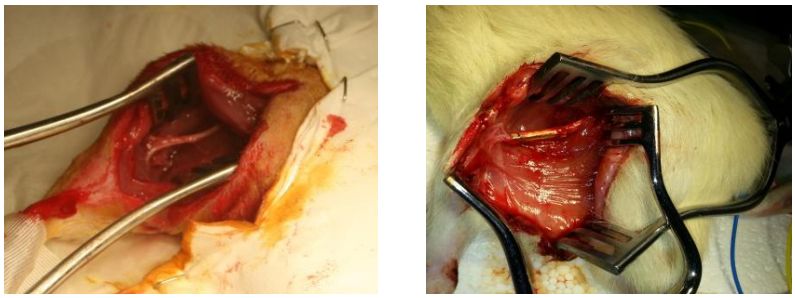

Figure 6.1. Sciatic nerve of rat.
Before (left) and after (right) conduit implantation.

Figure 6.2. Ulcer on rat heel.
Note the wasting of the musculature of the foot.

### 6.3.2 Late complications

Upon explantation, conduits were examined. Most were still spanning the gap between the two nerve stumps and the stumps were well secured by the sutures and overlapping conduit edge (Figure 6.1). However, complications were evident in a few animals. The distal nerve stump detached from the conduit in two cases, which were removed from the study at that point. The proximal nerve stump grew into adjacent muscle in one case, and was also removed from the study. These cases occurred in the beginning of the study and did not reoccur due to an increase in surgeon skill with practice.

### 6.3.3 Nerve conduction velocity

Nerve conduction velocities were never found on any of the animals that developed ulcers. Of those that remained ulcer-free, nerve conduction velocities were observed on two autografted animals at 3 and 8 months post-operatively (Table 2). Even after the reduction in NCV recording frequency, nerve conduction velocities were never obtained on animals with either an empty conduit or a conduit containing plain PLLA fibers. To date, one animal that received a PLLA+IKVAV fiber conduit has shown a nerve conduction velocity at one month post-operative. These findings are supported by the histological evidence. Additional animals and longer time points are currently awaiting explantation.

| Sample | Nerve conduction velocity (m/s) | | |
|---|---|---|---|
| | 1 mo | 3 mo | 8 mo |
| Autograft A | 0 | 18.2 | |
| Autograft B | 0 | 0 | 34.2 |
| Empty conduit | 0 | 0 | 0 |
| PLLA fibers | 0 | 0 | 0 |
| PLLA+IKVAV fibers | 5.8 | | |
| Control leg (avg.) | 61.6 | 56.9 | 59.6 |

Table 2. Nerve conduction recordings at various time points post-implantation.

### 6.3.4 Histology

The following figures are of hematoxyline and eosin stained cross section of sciatic nerve.

In native nerve, several fascicles are visible surrounded by layers of connective tissue (Figure 6.3). Upon higher magnification, many axons are present in the fascicles. Axons are identified based on morphology, and appear as white rings with dark centers and darker outlines. Blood vessels are also apparent in the fascicles.

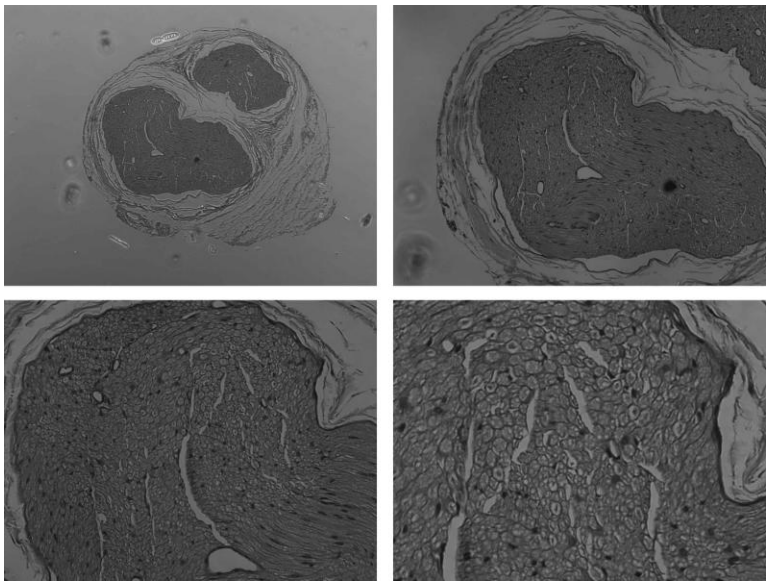

Figure 6.3. The structure of normal nerve at 4, 10, 20 and 40X.

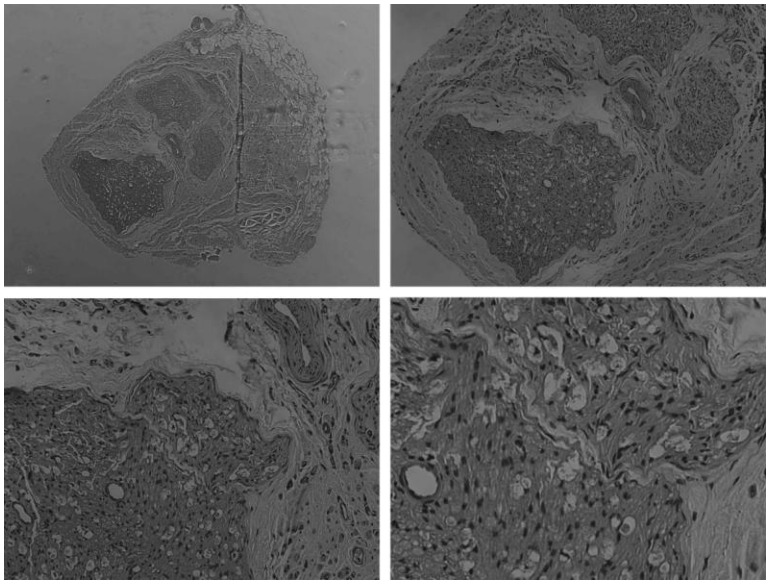

Figure 6.4. Regenerated nerve through an autograft at 4, 10, 20 and 40X.

Fascicles are also apparent in the cross sections of nerve repaired by autograft, although they are typically smaller in area and wrapped in more connective tissue than normal (Figure 6.4). Upon higher magnification, more nuclei are apparent, which is indicative of the normal proliferation of Schwann cells during regeneration. Some blood vessels are also present. Axons are clearly visible, though there are far less than the density seen in undamaged nerve. These findings were typical in every non-ulcerated case (N=4), although only two animals had detectable nerve conduction recordings at the time of explant.

Empty conduits supported no regenerating neurites. All of the empty conduits we observed were full of granulation tissue (Figure 6.5). No blood vessels, axons, or even nuclei were present. Empty conduits resulted in total regeneration failure in every case (N=7).

Conduits containing unmodified PLLA fibers also did not support regeneration (Figure 6.6). The films bearing the fibers were instead wrapped in layers of fibrous connective tissue. Macrophages were also present and contained intercellular components which stained yellow-brown after H&E staining – indicating iron containing blood debris. Few, if any, blood vessels were present. The fibrous capsule was surrounded by the same granulation tissue seen in the empty conduits. No axons were identified.

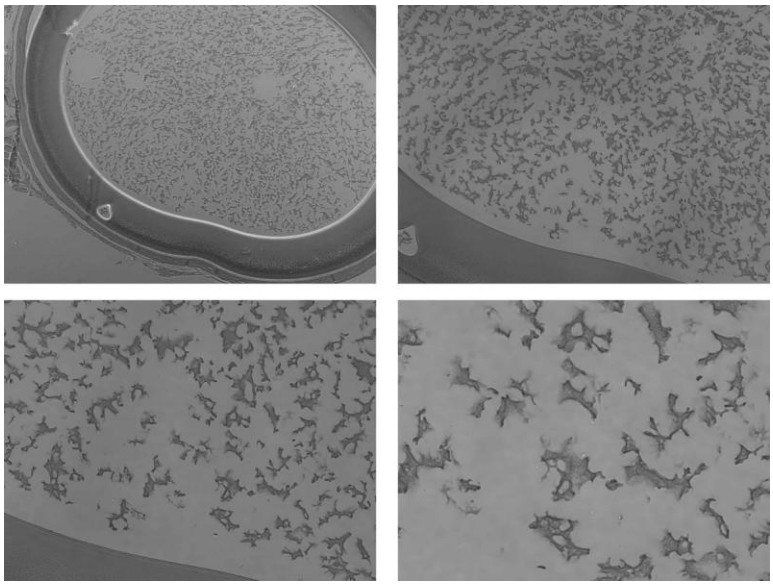

Figure 6.5. Empty tube conduit at 4, 10, 20 and 40X.

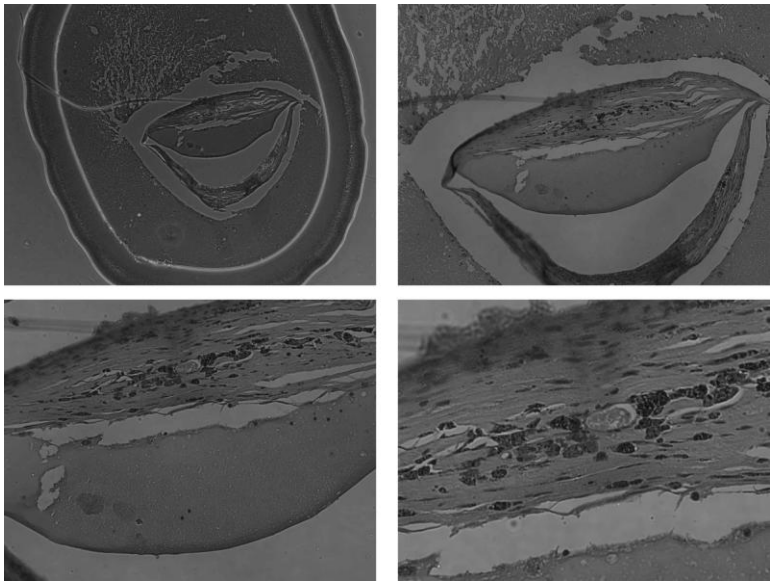

Figure 6.6. Conduit containing PLLA fibers at 4, 10, 20 and 40X.

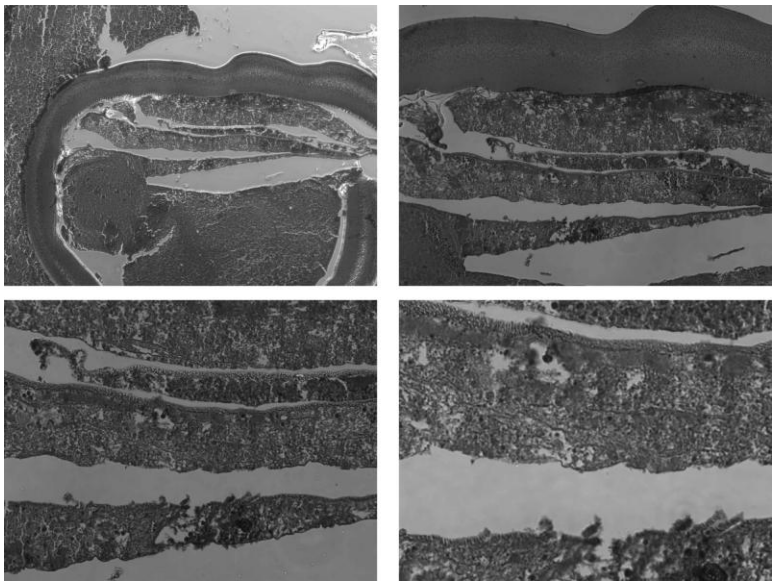

Figure 6.7. Conduit containing IKVAV-PLLA fibers at 4, 10, 20 and 40X.
This implant was explanted after 6 weeks *in vivo*. No nerve conduction velocity was recorded prior to explant on this particular animal although a very few axons can be identified.

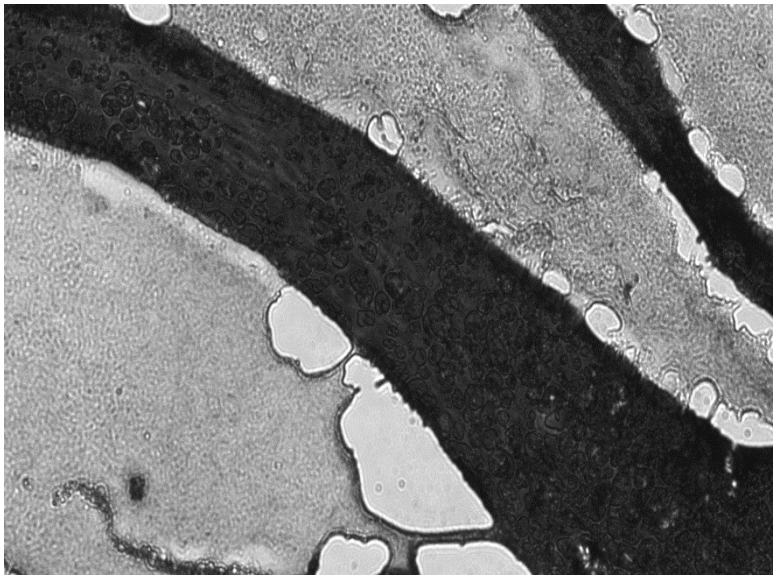

Figure 6.8. IKVAV-PLLA fiber conduit at 20X.
A nerve conduction velocity was recorded from this animal upon explant after 6 weeks. Note this figure was stained with toluidine blue.

In the case of the IKVAV-PLLA fiber conduits, results were more encouraging. Though the fibers themselves do not survive the histological processing, distinct layers of tissue were apparent in the spaces between the stacked layers of fibers. There was a small amount of connective tissue present at the fiber-tissue interface, but much less than observed in the unmodified PLLA fiber conduits. Above this connective tissue, regenerating nerve was apparent. Blood vessels and an abundance of Schwann cells were present. Some axons were clearly identifiable. The majority of the tissue seemed to be composed of small axons, although higher magnification images are needed to positively identify unmyelinated neurites. One animal to date has had detectable nerve conduction velocity upon explant following 6 weeks of implantation of a conduit containing IKVAV-PLLA fibers (Figure 6.8). We are currently conducting longer duration experiments. At only 6 weeks post-implantation, it is clear that regenerating neurites are present in small numbers across the whole length of the conduit. Given further time, these axons may increase in number and continue to migrate towards their innervation targets.

## 6.4 Conclusions

The results of this *in vivo* investigation were encouraging. Partial regeneration through the conduit with IKVAV-bound fibers was evident at six weeks and a preliminary nerve conduction velocity was recorded in one animal. Histological analysis revealed a few clear axons present in the conduit, migrating parallel to the fibers. The autograft control and the negative control conduits performed as expected. A nerve conduction velocity was observed on two autograft control animals, as were a large number of

axons. Neither the unbound fibers nor the empty conduit supported any regeneration, resulting only in fibrous scar tissue and granulation tissue, respectively.

While the IKVAV-bound fibers supported some regeneration, the number of regenerating axons was far lower than those in the autograft across a gap of the same size. However, the IKVAV-fibers vastly out-performed the non-bound fibers. So there may be some application for IKVAV-bound fiber nerve conduits in situations where there is insufficient donor nerve available for an autograft, as is the case with large gaps. There is also a need for longer duration experiments to better characterize the performance of the conduit, which are currently underway. The regeneration through the IKVAV-bound fiber conduit may more closely approximate the autograft if given more time.

# 7. Conclusions and future directions

## 7.1 Summary of conclusions

Injury to peripheral nerve can be devastating. Currently, autografting is the gold standard of repair. However, this method is limited by the amount of available donor nerve. Much work still needs to be done to address large gap injuries. Although a lot of research into peripheral nerve guidance conduits is taking place, no standard system of evaluation exists, which complicates comparisons between studies. In addition, some of the methods employed by others are not rigorous representations of in vivo conditions. Here we have presented a rigorous serum-free culture system, using primary motor and sensory neurons, to evaluate material candidates in vitro.

In Chapter 2, an electrospinning protocol was presented that reproducibly resulted in highly aligned PLLA fibers. The architecture of native nerve is extremely aligned. Artificial nerve guidance conduits attempt to replicate this alignment to minimize neurite wandering and direct regeneration. Electrospun fibers have been show numerous times to direct a variety of cell types. However, obtaining highly aligned nanofiber samples was difficult and time-consuming. We investigated the critical variables of the electrospinning process and determined a protocol that quickly produces extremely aligned fiber samples every time.

In Chapter 3, a protocol was presented that enabled high throughput computer aided analysis of neuronal morphology in vitro. A detailed analysis of neuronal development is necessary to determine cell response to experimental conditions. Morphological development is easy to observe but painstaking to analyze by hand. We have developed a procedure using MetaMorph and a custom Matlab script to obtain measurements of morphological characteristics of neurons and classify the neurons into developmental stages. These developmental stages are typical of all neurons, and simplify comparisons between studies. This method of analysis is robust yet simple to carry out. It has reduced the time necessary for analysis significantly.

In Chapter 4, the developed in vitro system was put through a rigorous validation test. Schwann cells are an essential component of the regeneration process in peripheral nerve. Normally, the distal stump has a very high number of SC following injury. In the case of gaps, however, nerve conduits represent a SC-free environment that regenerating neurites must traverse. (Loading these conduits with SC prior to implantation, while desirable, is not practical in humans.) Ideally, SC from the proximal stump would migrate quickly and populate the conduit to improve nerve regeneration. In order to simulate this environment, we cultured sensory neurons on electrospun fibers in the presence of aphidicolin, a SC inhibitor. Interestingly, on flat surfaces, aphidicolin resulted in a decrease in SC migration, while on electrospun fibers there was no change in the extent of SC migration. This is a promising indication that electrospun fibers may support SC in vivo, thus promoting better regeneration outcomes.

In Chapter 5, the validated experimental system was used to evaluate a number of material coatings. PLLA fibers with covalently bound IKVAV peptides resulted in the

greatest neurite extension. Thus, these fibers were packaged into polysulfone conduits and evaluated in vivo in Chapter 6. The in vivo investigation suffered from some early complications (heel ulcer) from the frequency of nerve conduction velocity recording. This problem has been remedied by reducing nerve conduction recording to once per animal, immediately prior to conduit explantation. The initial results from the in vivo investigation are encouraging. Controls are performing as expected. The IKVAV-PLLA fiber conduits show some limited regeneration at 6 weeks post implantation, though they vastly underperform autografts. Currently, more conduits have been implanted and will be analyzed at later time points.

In conclusion, this thesis undertook a logical next step in artificial nerve conduit design. The findings here support the use of peptide fragments in lieu of whole proteins in vivo. The regeneration seen in the IKVAV fiber conduits is encouraging and highlights the need for continued research in this area. Further refinement is necessary to investigate the translatability of this work to clinical use.

## 7.2 Recommendations for future research

The design of artificial nerve conduits must evolve as our understanding of peripheral nerve injury continues to grow. The vast majority of peripheral nerve regeneration research has focused on physically bridging gaps and neurite guidance. However, basic research is beginning to suggest that getting the neurites to the target is not the root of the problem. Given enough time, the vast majority of neurites will reach even the most distal of innervation targets. However, once there, they simply fail to reinnervate. Mackinnon and colleagues first demonstrated that once muscle had been

denervated for a sufficient period of time, it resisted reinnervation [175]. This phenomenon has been termed chronic denervation injury.

Our understanding of chronic denervation injury is limited. However, more recent work suggests that it is not changes in the muscle which prevent reinnervation, but the loss of an axon-supporting environment in the distal stump over time. This is thought to be due to changes undergone by chronically denervated Schwann cells [5, 176]. Immediately following injury, SC proliferate and lose their differentiated phenotype – beginning to resemble immature non-myelinating cells [11]. Various genes are up-regulated, including those for the neu receptors c-erbB2, c-erbB3 and c-erbB4 [11], as well as the low affinity nerve growth factor receptor protein p75 [10]. SC also begin to secrete the growth factors BDNF [9, 10], GDNF [9] and NGF [10]. If axonal contact is re-established quickly, SC will regain their differentiated phenotype [177]. However, if regeneration is delayed for several months, SC in the distal stump stop proliferating, atrophy [5] and no longer express c-erbB2, c-erbB3 or c-erbB4 [177, 178]. Li (1997) and Hall (1999) demonstrated that chronically denervated distal nerve stumps with reduced c-erbB expression were significantly less reinnervated than acutely denervated distal stumps with up-regulated c-erbB expression. Additionally, in cases of prolonged regeneration, axons in the proximal stump suffer from the lack of an established target; this has been termed chronic axotomy. Over time, these neurons lose their ability to support regenerating axons. The time course of this decline closes parallels the decline in neurotrophic support secreted from SC in the distal stump [9]. Furthermore, the effects of chronic axotomy can be eliminated by the application of exogenous growth factors, including BDNF and GDNF [9, 179]. These findings further support the

hypothesis that it is the loss of an axon-supporting microenvironment in the distal stump that precludes reinnervation of the most distal targets. In humans, these changes begin to take place after only three months of denervation. With an average speed of 1 mm/day of neurite extension, this is a very small window.

Clearly then time must become an important factor in the design of artificial nerve guides. Directional guidance alone will not solve the problem of regeneration across large gaps. Nor will further inclusion of growth factors – the time window is small and the fundamental speed of neurite extension is too slow. Future work should address either increasing the time window, by supporting SC in the distal stump, or dramatically increasing the speed of neurite extension. Increasing the time window is more likely to be addressed with future drug development, but there may be an engineering approach available to address increasing the speed of regeneration.

There is considerable evidence that applying mechanical tension can increase the speed of neurite extension. It has been demonstrated that while growth cones migrate at the rate of 1 mm/day, axons grow at much faster rates when stretched during the adolescent phases of development [180]. Recently, Smith and colleagues have demonstrated that sensory neurites from dorsal root ganglia (DRG) can be grown during mechanical stretch at up to 8 mm/day [180].These neurons grown under mechanical tension, termed “stretch-growth,” express sodium and potassium channels, fire action potentials [181], and can be grafted into peripheral nerve gaps [182]. This important and novel work, however, has only yet been conducted with sensory neurites from dorsal root ganglia (DRG), which cannot innervate muscle in and of themselves. Our

laboratory is moving forward with such experiments using motor neurons that might eventually be coaxed into innervating native muscle.

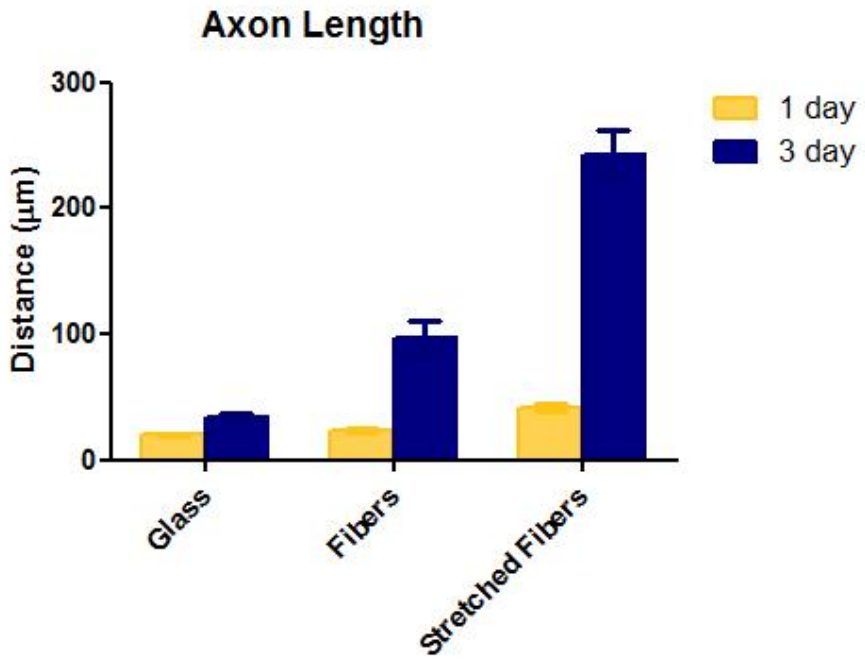


Figure 7.1. Stretch growth of motor neurons.
Motor neurons cultured on stretched fibers have dramatically longer major neurites after three days in culture. These samples were stretched with a 3 hr on/3 hr off stretching cycle.

Recently, we have demonstrated in the laboratory that mechanical tension increases the length of neurites from developing motor neurons dramatically (Figure 7.1). Further work is needed to optimize the stretching process, however, we feel stretch growth is a promising advancement in the field of peripheral nerve regeneration, that combined with the directional guidance offered by fibrous cues, may serve to promote clinically superior peripheral nerve regeneration.

## References


1. Noble, J., C. Munro, and V. Prasad, *Analysis of upper and lower extremity peripheral nerve injuries in a population of patients with multiple injuries.* J Traum, 1998. **45**(1): p. 116-122.
2. Bertelli, J.A.T., M., J.C. Mira, and M.F. Ghizoni, *The course of aberrant reinnervation following nerve repair with fresh or denatured muscle autografts.* J Peripher Nerv Syst. , 2005. **10**(4): p. 359-368.
3. Dunlop, S.A., et al., *Regenerating optic axons restore topography after incomplete nerve injury.* J Comp Neurol., 2007. **202**(1): p. 46-57.
4. Taha, J.M., J.M. Tew, and R.W. Keith, *Proximal-to-distal facial amplitude ratios as predictors of facial nerve function after acoustic neuroma excision.* J Neurosurg., 1995. **83**(6): p. 993-998.
5. Sulaiman, O.A.R. and T. Gordan, *Role of chronic Schwann cell denervation in poor functional recovery after nerve injuries and experimental strategies to combat it.* Neurosurgery, 2009. **65**: p. A105-A115.
6. Bruck, W., *The role of macrophages in Wallerian degeneration.* Brain Pathol. , 2008. **7**(2): p. 741-752.
7. Belkas, J.S., M.S. Shoichet, and R. Midha, *Peripheral nerve regeneration through guidance tubes.* Neurol Res., 2004. **26**(2): p. 151-160.
8. Funakoshi, H., et al., *Persson H. Differential expression of mRNAs for neurotrophins and their receptos after axotomy of the sciatic nerve.* J Cell Biol, 1993. **123**(2): p. 455-465.
9. Boyd, J.G. and T. Gorden, *Glial cell line-derived neurotrophic factor and brain-derived neurotrophic factor sustain the axonal regeneration of chronically axotomized motoneurons in vivo.* Exp Neurol., 2003. **183**(610-619).
10. Heuman, R., *Differential regulation of mRNA encoding nerve growth factor and its receptor in rat sciatic nerves during development, degeneration and regeneration. .* Proc Natl Acad Sci, 1987. **84**: p. 8735-8739.
11. Cohen, J.A., et al., *Expression of the neu proto-oncogene by Schwann cells during peripheral nerve development and Wallerian degeneration.* J Neurosci Res, 1992. **31**: p. 622-634.
12. Daniloff, J.K., et al., *Altered expression of neuronal cell adhesion molecules induced by nerve injury and repair.* J Cell Biol, 1986. **103**(3): p. 929.
13. Ribeiro-Resende, V.T., et al., *Strategies for inducing the formation of bands of Bunger in peripheral nerve regeneration.* Biomaterials, 2009. **30**: p. 5251-5259.
14. Fleur, M.L., et al., *Basement membrane and repair of injury to peripheral nerve.* J Exp Med., 1996. **184**(6): p. 2311.
15. Mackinnon, S.E., et al., *Clinical outcome following nerve allograft transplantation. .* Plast Reconstr Surg. , 2001. **107**(6): p. 1419-1429.
16. Kechele, P.R., et al., *THE MESH REPAIR: TENSION FREE ALTERNATIVE ON DEALING WITH NERVE GAPS-EXPERIMENTAL RESULTS.* Microsurgery, 2011. **31**(7): p. 551-558.
17. Hill, H.L., L.O. Vasconez, and M.J. Jurkiewicz, *Method for obtaining a sural nerve graft.* Plast Reconstr Surg., 1978. **61**(2): p. 177-179.

18. Hoke, A., et al., *Schwann Cells Express Motor and Sensory Phenotypes That Regulate Axon Regeneration.* J. Neurosci., 2006. **26**(38): p. 9646-9655.
19. Sondell, M., G. Lundborg, and M. Kanje, *Regeneration of rat sciatic nerve into allografts made acellular through chemical extraction.* Brain Res., 1998. **795**(1-2): p. 44-57.
20. Bader, B., J.M. Corey, Personal communication, 2008: Ann Arbor.
21. Hogikyan, N., J.M. Corey, Personal communication, 2008: Ann Arbor.
22. Telian, S., J.M. Corey, Personal communication, 2008: Ann Arbor.
23. Cataltepe, O., et al., *Arterial bridging for peripheral nerve graft: a comparative study.* Acta neurochir., 1993. **121**(3-4): p. 181-186.
24. Tseng, C.Y., et al., *Histological analysis of Schwann cell migration and peripheral nerve regeneration in the autogenous venous nerve conduit.* J Reconstr Microsurg., 2003. **19**(5): p. 331-339.
25. Varahao, A.S., et al., *Functional assessment of sciatic nerve recovery: biodegradable poly(DLLA-E-CL) nerve guide filled with fresh skeletal muscle. .* Microsurgery, 2003. **23**: p. 346-353.
26. Williams, L.R. and S. Varon, *Modification of fibrin matrix formation in situ enhances nerve regeneration in silicone chambers.* J Comp Neurol, 1985. **231**(2): p. 209-20.
27. Diaz-Flores, L., et al., *Contribution of the proximal and distal nerve stumps to peripheral nerve regeneration in silicone chambers.* Histol Histopathol. , 1995. **10**(4): p. 937-946.
28. Corey, J.M., et al., *The design of electrospun PLLA nanofiber scaffolds compatible with serum-free growth of primary motor and sensory neurons.* Acta Biomater, 2008. **4**(4): p. 863-75.
29. Weber, R.A., et al., *A randomized prospective study of polyglycolic acid conduits for digital nerve reconstruction. .* Plast Reconstr Surg., 2000. **106**(5): p. 1036 - 1045.
30. Schappacher, M., et al., *Study of a trimethylenecarbonate-co-e-caprolactone polymer. .* Biomaterials, 2001. **22**(22): p. 2951-2958.
31. Wang, X., et al., *Peroneal nerve regeneration using a unique bilayer polyurethane-collagen guide conduit. .* J Bioact Compat Pol., 2009. **24**: p. 109-123.
32. Koh, H.S., et al., *Enhancement of neurite outgrowth using nano-structured scaffolds coupled with laminin.* Biomaterials, 2008. **29**(26): p. 3574-82.
33. Yu, X. and R.V. Bellamkonda, *Tissue-engineered scaffolds are effective alternatives to autografts for bridging peripheral nerve gaps.* Tissue Eng, 2003. **9**(3): p. 421-30.
34. Rodriguez, F.J., et al., *Nerve guides seeded with autologous Schwann cells improve nerve regeneration.* Exp Neurol., 2000. **161**(2): p. 571-584.
35. Hayashi, A.M., A., et al., *Treatment modality affects allograft-derived Schwann cell phenotype and myelinating capacity.* Exp Neurol., 2008. **212**: p. 324-336.
36. Putnam, A.J. and D.J. Mooney, *Tissue engineering using synthetic extracellular matrices.* Nat Med, 1996. **2**(7): p. 824-6.
37. Hudson, T.W., G.R. Evans, and C.E. Schmidt, *Engineering strategies for peripheral nerve repair.* Orthop Clin North Am, 2000. **31**(3): p. 485-98.
38. Lee, A.C., et al., *Controlled release of nerve growth factor enhances sciatic nerve regeneration.* Exp Neurol, 2003. **184**(1): p. 295-303.
39. Lee, K.Y. and D.J. Mooney, *Hydrogels for tissue engineering.* Chem Rev, 2001. **101**(7): p. 1869-79.
40. O'Connor, S.M., et al., *Survival and neurite outgrowth of rat cortical neurons in three-dimensional agarose and collagen gel matrices.* Neurosci Lett, 2001. **304**(3): p. 189-93.
41. Rowley, J.A. and D.J. Mooney, *Alginate type and RGD density control myoblast phenotype.* J Biomed Mater Res, 2002. **60**(2): p. 217-23.
42. Eser Elcin, A., Y.M. Elcin, and G.D. Pappas, *Neural tissue engineering: adrenal chromaffin cell attachment and viability on chitosan scaffolds.* Neurol Res, 1998. **20**(7): p. 648-54.

43. Bellamkonda, R., J.P. Ranieri, and P. Aebischer, *Laminin oligopeptide derivatized agarose gels allow three-dimensional neurite extension in vitro.* J Neurosci Res, 1995. **41**(4): p. 501-9.
44. Harris, L.D., B.S. Kim, and D.J. Mooney, *Open pore biodegradable matrices formed with gas foaming.* J Biomed Mater Res, 1998. **42**(3): p. 396-402.
45. Corey, J.M., et al., *Aligned electrospun nanofibers specify the direction of dorsal root ganglia neurite growth.* J Biomed Mater Res A, 2007. **83**(3): p. 636-45.
46. Chew, S.Y., et al., *The effect of the alignment of electrospun fibrous scaffolds on Schwann cell maturation.* Biomaterials, 2008. **29**(6): p. 653-61.
47. Kim, Y.T., et al., *The role of aligned polymer fiber-based constructs in the bridging of long peripheral nerve gaps.* Biomaterials, 2008. **29**(21): p. 3117-27.
48. Wang, H.B., et al., *Creation of highly aligned electrospun poly-L-lactic acid fibers for nerve regeneration applications.* J Neural Eng, 2009. **6**(1): p. 1-15.
49. Hu, W., et al., *Polyglycolic acid filaments guide Schwann cell migration in vitro and in vivo. .* Biotechnol Lett., 2008. **30**: p. 1937-1942.
50. Kalbermatten, D.F., et al., *Fibrin matrix for suspension of regenerative cells in an artificial nerve conduit. .* J Palst Reconstr Aesthet Surg, 2008. **61**(6): p. 669-675.
51. Ceballos, D., et al., *Magnetically aligned collagen gel filling a collagen nerve guide improves peripheral nerve regeneration. .* Exp Neurol., 1999. **158**(2): p. 290-300.
52. Ghasemi-Mobarakeh, L., et al., *Electrospun poly(ε-caprolactone)/gelatin nanofibrous scaffolds for nerve tissue engineering.* Biomaterials, 2008. **29**(34): p. 4532-4539.
53. Subramanian, A., et al., *Preparation and evaluation of the electrospun chitosan/PEO fibers for potential applications in cartilage tissue engineering.* Journal of Biomaterials Science-Polymer Edition, 2005. **16**(7): p. 861-873.
54. Lee, C.H., et al., *Nanofiber alignment and direction of mechanical strain affect the ECM production of human ACL fibroblast.* Biomaterials, 2005. **26**(11): p. 1261-70.
55. Cooper, A., et al., *Aligned chitosan-based nanofibers for enhanced myogenesis.* Journal of Materials Chemistry, 2010. **20**(40): p. 8904-8911.
56. Uttayarat, P., et al., *Micropatterning of three-dimensional electrospun polyurethane vascular grafts.* Acta Biomaterialia, 2010. **6**(11): p. 4229-4237.
57. Wang, Y., et al., *The differential effects of aligned electrospun PHBHHx fibers on adipogenic and osteogenic potential of MSCs through the regulation of PPAR gamma signaling.* Biomaterials, 2012. **33**(2): p. 485-493.
58. Purcell, E.K., et al., *Combining Topographical and Genetic Cues to Promote Neuronal Fate Specification in Stem Cells.* Biomacromolecules, 2012. **13**(11): p. 3427-3438.
59. Peng, H.J., et al., *Electrospun biomimetic scaffold of hydroxyapatite/chitosan supports enhanced osteogenic differentiation of mMSCs.* Nanotechnology, 2012. **23**(48).
60. Cooper, A., M. Leung, and M.Q. Zhang, *Polymeric Fibrous Matrices for Substrate-Mediated Human Embryonic Stem Cell Lineage Differentiation.* Macromolecular Bioscience, 2012. **12**(7): p. 882-892.
61. Lee, S., et al., *A culture system to study oligodendrocyte myelination processes using engineered nanofibers.* Nature Methods, 2012. **9**(9): p. 917-+.
62. Goh, Y.F., I. Shakir, and R. Hussain, *Electrospun fibers for tissue engineering, drug delivery, and wound dressing.* Journal of Materials Science, 2013. **48**(8): p. 3027-3054.
63. Condic, M.L., *Neural development: axon regeneration derailed by dendrites.* Curr Biol, 2002. **12**(13): p. R455-7.
64. Letourneau, P.C., M.L. Condic, and D.M. Snow, *Interactions of developing neurons with the extracellular matrix.* J Neurosci, 1994. **14**(3 Pt 1): p. 915-28.

65. Powell, S.K. and H.K. Kleinman, *Neuronal laminins and their cellular receptors.* Int J Biochem Cell Biol, 1997. **29**(3): p. 401-14.
66. Ide, C., *Peripheral nerve regeneration.* Neurosci Res, 1996. **25**(2): p. 101-21.
67. Frostick, S.P., Q. Yin, and G.J. Kemp, *Schwann cells, neurotrophic factors, and peripheral nerve regeneration.* Microsurgery, 1998. **18**(7): p. 397-405.
68. Tashiro, K., et al., *A synthetic peptide containing the IKVAV sequence from the A chain of laminin mediates cell attachment, migration, and neurite outgrowth.* J Biol Chem, 1989. **264**(27): p. 16174-82.
69. Richard, B.L., et al., *Identification of synthetic peptides derived from laminin alpha1 and alpha2 chains with cell type specificity for neurite outgrowth.* Exp Cell Res, 1996. **228**(1): p. 98-105.
70. Kleinman, H.K., et al., *Laminin in neuronal development.* Ann N Y Acad Sci, 1990. **580**: p. 302-10.
71. Sephel, G.C., et al., *Laminin A chain synthetic peptide which supports neurite outgrowth.* Biochem Biophys Res Commun, 1989. **162**(2): p. 821-9.
72. Wildering, W.C., P.M. Hermann, and A.G. Bulloch, *Neurite outgrowth, RGD-dependent, and RGD-independent adhesion of identified molluscan motoneurons on selected substrates.* J Neurobiol, 1998. **35**(1): p. 37-52.
73. Guan, W., M.A. Puthenveedu, and M.L. Condic, *Sensory neuron subtypes have unique substratum preference and receptor expression before target innervation.* J Neurosci, 2003. **23**(5): p. 1781-91.
74. Manthorpe, M., et al., *Laminin promotes neuritic regeneration from cultured peripheral and central neurons.* J Cell Biol, 1983. **97**(6): p. 1882-90.
75. Gerardo-Nava, J., et al., *Human neural cell interactions with orientated electrospun nanofibers in vitro.* Nanomedicine, 2009. **4**(1): p. 11-30.
76. Mollers, S., et al., *Cytocompatibility of a Novel, Longitudinally Microstructured Collagen Scaffold Intended for Nerve Tissue Repair.* Tissue Engineering Part A, 2009. **15**(3): p. 461-472.
77. Kunzmann, A., et al., *Toxicology of engineered nanomaterials: Focus on biocompatibility, biodistribution and biodegradation.* Biochimica Et Biophysica Acta-General Subjects, 2011. **1810**(3): p. 361-373.
78. Geurtsen, W., et al., *Cytotoxicity of four root canal sealers in permanent 3T3 cells and primary human periodontal ligament fibroblast cultures.* Oral Surgery Oral Medicine Oral Pathology Oral Radiology and Endodontics, 1998. **85**(5): p. 592-597.
79. Craig, A.M. and G. Banker, *Neuronal polarity.* Annu Rev Neurosci, 1994. **17**: p. 267-310.
80. Yang, F., et al., *Electrospinning of nano/micro scale poly(L-lactic acid) aligned fibers and their potential in neural tissue engineering.* Biomaterials, 2005. **26**(15): p. 2603-10.
81. Gertz, C.C., et al., *Accelerated neuritogenesis and maturation of primary spinal motor neurons in response to nanofibers.* Dev Neurobiol, 2010. **70**(8): p. 589-603.
82. Madduri, S., M. Papaloizos, and B. Gander, *Trophically and topographically functionalized silk fibroin nerve conduits for guided peripheral nerve regeneration.* Biomaterials, 2010. **31**(8): p. 2323-2334.
83. Li, Y., et al., *Transforming growth factor-alpha: a major human serum factor that promotes human keratinocyte migration.* J Invest Dermatol, 2006. **126**(9): p. 2096-105.
84. Gu, Y., C. Wang, and A. Cohen, *Effect of IGF-1 on the balance between autophagy of dysfunctional mitochondria and apoptosis.* FEBS Lett, 2004. **577**(3): p. 357-60.
85. Boone, C.W., et al., *QUALITY-CONTROL STUDIES ON FETAL BOVINE SERUM USED IN TISSUE-CULTURE.* In Vitro-Journal of the Tissue Culture Association, 1971. **7**(3): p. 174-&.
86. Brewer, G.J., et al., *Optimized survival of hippocampal neurons in B27-supplemented Neurobasal, a new serum-free medium combination.* J Neurosci Res, 1993. **35**(5): p. 567-76.

87. Brewer, G.J., *Serum-free B27/neurobasal medium supports differentiated growth of neurons from the striatum, substantia nigra, septum, cerebral cortex, cerebellum, and dentate gyrus.* J Neurosci Res, 1995. **42**(5): p. 674-83.
88. Dotti, C.G., C.A. Sullivan, and G.A. Banker, *The establishment of polarity by hippocampal neurons in culture.* J Neurosci, 1988. **8**(4): p. 1454-68.
89. Fukata, Y., T. Kimura, and K. Kaibuchi, *Axon specification in hippocampal neurons.* Neuroscience Research, 2002. **43**(4): p. 305-315.
90. Tuck, S.J., et al., *Critical variables in the alignment of electrospun PLLA nanofibers.* Materials Science and Engineering: C, 2012. **32**(7): p. 1779-1784.
91. Leach, M.K., et al., *Stages of neuronal morphological development in vitro - an automated assay.* J Neurosci Meth., 2011.
92. Prabhakaran, M.P., J. Venugopal, and S. Ramakrishna, *Electrospun nanostructured scaffolds for bone tissue engineering.* Acta Biomaterialia, 2009. **5**(8): p. 2884-2893.
93. Schmidt, D., et al., *Minimally-Invasive Implantation of Living Tissue Engineered Heart Valves A Comprehensive Approach From Autologous Vascular Cells to Stem Cells.* Journal of the American College of Cardiology, 2010. **56**(6): p. 510-520.
94. Hashizume, R., et al., *Morphological and mechanical characteristics of the reconstructed rat abdominal wall following use of a wet electrospun biodegradable polyurethane elastomer scaffold.* Biomaterials, 2010. **31**(12): p. 3253-3265.
95. Marklein, R.A. and J.A. Burdick, *Controlling Stem Cell Fate with Material Design.* Advanced Materials, 2010. **22**(2): p. 175-189.
96. Yin, Z., et al., *The regulation of tendon stem cell differentiation by the alignment of nanofibers.* Biomaterials, 2010. **31**(8): p. 2163-2175.
97. Afifi, A.M., et al., *Fabrication of Aligned Poly(L-lactide) Fibers by Electrospinning and Drawing.* Macromolecular Materials and Engineering, 2009. **294**(10): p. 658-665.
98. Beachley, V. and X.J. Wen, *Effect of electrospinning parameters on the nanofiber diameter and length.* Materials Science & Engineering C-Biomimetic and Supramolecular Systems, 2009. **29**(3): p. 663-668.
99. Chanunpanich, N. and H. Byun, *Alignment of electrospun polystyrene with an electric field.* Journal of Applied Polymer Science, 2007. **106**(6): p. 3648-3652.
100. Bazbouz, M.B. and G.K. Stylios, *Alignment and optimization of nylon 6 nanofibers by electrospinning.* Journal of Applied Polymer Science, 2008. **107**(5): p. 3023-3032.
101. Stankus, J.J., J.J. Guan, and W.R. Wagner, *Fabrication of biodegradable elastomeric scaffolds with sub-micron morphologies.* Journal of Biomedical Materials Research Part A, 2004. **70A**(4): p. 603-614.
102. Traversa, E., et al., *Tuning hierarchical architecture of 3D polymeric scaffolds for cardiac tissue engineering.* Journal of Experimental Nanoscience, 2008. **3**(2): p. 97-110.
103. Buttafoco, L., et al., *Electrospinning of collagen and elastin for tissue engineering applications.* Biomaterials, 2006. **27**(5): p. 724-734.
104. Kimura, N., et al., *Molecular Orientation and Crystalline Structure of Aligned Electrospun Nylon 6 Nanofibers: Effect of Gap Size*, in *Silk: Inheritance and Innovation - Modern Silk Road*, L. Bai and G.Q. Chen, Editors. 2011. p. 333-336.
105. Buchko, C.J., et al., *Processing and microstructural characterization of porous biocompatible protein polymer thin films* Polymer, 1999. **40**(26): p. 7397-7407.
106. Theron, A., E. Zussman, and Y. AL, *Electrostatic field-assisted alignment of electrospun nanofibers.* Nanotech., 2001. **12**: p. 384-390.

107. Yang, Y., et al., *The effects of flow rate and the distance between the nozzle and the target on the operating conditions of electrospinning.* Journal of Polymer Engineering, 2008. **28**(1-2): p. 67-86.
108. Xu, C., et al., *Electrospinning of Poly(ethylene-co-vinyl alcohol) Nanofibres Encapsulated with Ag Nanoparticles for Skin Wound Healing.* Journal of Nanomaterials, 2011.
109. Wannatong, L., A. Sirivat, and P. Supaphol, *Effects of solvents on electrospun polymeric fibers: preliminary study on polystyrene.* Polymer International, 2004. **53**(11): p. 1851-1859.
110. Henriques, C., et al., *A Systematic Study of Solution and Processing Parameters on Nanofiber Morphology Using a New Electrospinning Apparatus.* J Nanosci Nanotechnol, 2009. **9**(6): p. 3535-3545.
111. Cui, X.J., et al., *Fabrication of Continuous Aligned Polyvinylpyrrolidone Fibers via Electrospinning by Elimination of the Jet Bending Instability.* Journal of Applied Polymer Science, 2010. **116**(6): p. 3676-3681.
112. De Vrieze, S., et al., *The effect of temperature and humidity on electrospinning.* Journal of Materials Science, 2009. **44**(5): p. 1357-1362.
113. Sundaray, B., et al., *Electrospinning of continuous aligned polymer fibers.* Applied Physics Letters, 2004. **84**(7): p. 1222-1224.
114. Deitzel, J.M., et al., *Controlled deposition of electrospun poly(ethylene oxide) fibers.* Polymer, 2001. **42**(19): p. 8163-8170.
115. Qin, X.H., et al., *Stretching of the steady jet in electrospinning: theoretical analysis and experimental verification.* Textile Research Journal, 2011. **81**(4): p. 388-397.
116. Da Silva, J.S. and C.G. Dotti, *Breaking the neuronal sphere: regulation of the actin cytoskeleton in neuritogenesis.* Nat Rev Neurosci, 2002. **3**(9): p. 694-704.
117. Gupton, S.L. and F.B. Gertler, *Integrin Signaling Switches the Cytoskeletal and Exocytic Machinery that Drives Neuritogenesis.* Developmental Cell, 2010. **18**(5): p. 725-736.
118. Budd, J.M.L., et al., *Neocortical Axon Arbors Trade-off Material and Conduction Delay Conservation.* Plos Computational Biology, 2010. **6**(3).
119. Ristanovic, D., et al., *Morphology and classification of large neurons in the adult human dentate nucleus: A qualitative and quantitative analysis of 2D images.* Neuroscience Research, 2010. **67**(1): p. 1-7.
120. Banker, G.A. and W.M. Cowan, *RAT HIPPOCAMPAL NEURONS IN DISPERSED CELL-CULTURE.* Brain Research, 1977. **126**(3): p. 397-425.
121. Krivosheya, D., et al., *ErbB4-Neuregulin Signaling Modulates Synapse Development and Dendritic Arborization through Distinct Mechanisms.* Journal of Biological Chemistry, 2008. **283**(47): p. 32944-32956.
122. Sutton, M.A. and E.M. Schuman, *Dendritic protein synthesis, synaptic plasticity, and memory.* Cell, 2006. **127**(1): p. 49-58.
123. Calderon de Anda, F., et al., *Pyramidal neuron polarity axis is defined at the bipolar stage.* J Cell Sci, 2008. **121**(Pt 2): p. 178-85.
124. Dertinger, S.K., et al., *Gradients of substrate-bound laminin orient axonal specification of neurons.* Proc Natl Acad Sci U S A, 2002. **99**(20): p. 12542-7.
125. Vogt, A.K., et al., *Impact of micropatterned surfaces on neuronal polarity.* J Neurosci Methods, 2004. **134**(2): p. 191-8.
126. Lanfer, B., et al., *Directed Growth of Adult Human White Matter Stem Cell-Derived Neurons on Aligned Fibrillar Collagen.* Tissue Engineering Part A, 2010. **16**(4): p. 1103-1113.
127. Vergano-Vera, E., et al., *Lack of adrenomedullin affects growth and differentiation of adult neural stem/progenitor cells.* Cell and Tissue Research, 2010. **340**(1): p. 1-11.

128. Johnson, P.J., S.R. Parker, and S.E. Sakiyama-Elbert, *Fibrin-based tissue engineering scaffolds enhance neural fiber sprouting and delay the accumulation of reactive astrocytes at the lesion in a subacute model of spinal cord injury.* Journal of Biomedical Materials Research Part A, 2010. **92A**(1): p. 152-163.
129. Meijering, E., *Neuron Tracing in Perspective.* Cytometry Part A, 2010. **77A**(7): p. 693-704.
130. Klimaschewski, L., et al., *Biolistic transfection and morphological analysis of cultured sympathetic neurons.* Journal of Neuroscience Methods, 2002. **113**(1): p. 63-71.
131. Narayan, P.J., et al., *High throughput quantification of cells with complex morphology in mixed cultures.* Journal of Neuroscience Methods, 2007. **164**(2): p. 339-349.
132. Myatt, D. and S. Nasuto, *Improved automatic midline tracing of neurites with Neuromantic.* BMC Neuroscience, 2008. **9**: p. P81.
133. Popko, J., et al., *Automated Analysis of NeuronJ Tracing Data.* Cytometry Part A, 2009. **75A**(4): p. 371-376.
134. Vallotton, P., et al., *Automated analysis of neurite branching in cultured cortical neurons using HCA-Vision.* Cytometry Part A, 2007. **71A**(10): p. 889-895.
135. Vincent, A.M., et al., *IGF-I prevents glutamate-induced motor neuron programmed cell death.* Neurobiol Dis, 2004. **16**(2): p. 407-16.
136. Russell, J.W., et al., *High glucose-induced oxidative stress and mitochondrial dysfunction in neurons.* Faseb J, 2002. **16**(13): p. 1738-48.
137. Donohue, D.E. and G.A. Ascoli, *Automated reconstruction of neuronal morphology: An overview.* Brain Research Reviews, 2011. **67**(1-2): p. 94-102.
138. Regan, T.M., et al., *Nanofibers promote Schwann cell migration when Schwann cell proliferation is impaired.* Minerva Biotechnologica. **in press**.
139. Thomas, P.K., *Invited review: focal nerve injury: guidance factors during axonal regeneration.* Muscle Nerve, 1989. **12**(10): p. 796-802.
140. Cajal, R.y., *Degeneration and regeneration in the nervous system*1928, London: Oxford University Press.
141. Politis, M.J., K. Ederle, and P.S. Spencer, *Tropism in nerve regeneration in vivo. Attraction of regenerating axons by diffusible factors derived from cells in distal nerve stumps of transected peripheral nerves.* Brain Res, 1982. **253**(1-2): p. 1-12.
142. Anderson, P.N., et al., *An ultrastructural study of the early stages of axonal regeneration through rat nerve grafts.* Neuropathol Appl Neurobiol, 1983. **9**(6): p. 455-66.
143. Hall, S.M., *The effect of inhibiting Schwann cell mitosis on the re-innervation of acellular autografts in the peripheral nervous system of the mouse.* Neuropathol Appl Neurobiol, 1986. **12**(4): p. 401-14.
144. Chew, S.Y., et al., *Sustained release of proteins from electrospun biodegradable fibers.* Biomacromolecules, 2005. **6**(4): p. 2017-24.
145. Lundborg, G., et al., *A new type of "bioartificial" nerve graft for bridging extended defects in nerves.* J Hand Surg [Br], 1997. **22**(3): p. 299-303.
146. Rangappa, N., et al., *Laminin-coated poly(L-lactide) filaments induce robust neurite growth while providing directional orientation.* J Biomed Mater Res, 2000. **51**(4): p. 625-34.
147. Wen, X. and P.A. Tresco, *Effect of filament diameter and extracellular matrix molecule precoating on neurite outgrowth and Schwann cell behavior on multifilament entubulation bridging device in vitro.* J Biomed Mater Res A, 2006. **76**(3): p. 626-37.
148. Chew, S.Y., et al., *Aligned Protein-Polymer Composite Fibers Enhance Nerve Regeneration: A Potential Tissue-Engineering Platform.* Adv Funct Mater, 2007. **17**(8): p. 1288-1296.

149. Schnell, E., et al., *Guidance of glial cell migration and axonal growth on electrospun nanofibers of poly-epsilon-caprolactone and a collagen/poly-epsilon-caprolactone blend.* Biomaterials, 2007. **28**(19): p. 3012-25.
150. Gomez, N., S. Chen, and C.E. Schmidt, *Polarization of hippocampal neurons with competitive surface stimuli: contact guidance cues are preferred over chemical ligands.* J R Soc Interface, 2007. **4**(13): p. 223-33.
151. Xie, J., et al., *The differentiation of embryonic stem cells seeded on electrospun nanofibers into neural lineages.* Biomaterials, 2009. **30**(3): p. 354-62.
152. Gumy, L.F., E.T. Bampton, and A.M. Tolkovsky, *Hyperglycaemia inhibits Schwann cell proliferation and migration and restricts regeneration of axons and Schwann cells from adult murine DRG.* Mol Cell Neurosci, 2008. **37**(2): p. 298-311.
153. Cui, C., et al., *Analysis of tissue flow patterns during primitive streak formation in the chick embryo.* Dev Biol, 2005. **284**(1): p. 37-47.
154. Iwasaki, T., et al., *Cell-cycle-dependent invasion in vitro by rat ascites hepatoma cells.* Int J Cancer, 1995. **63**(2): p. 282-7.
155. Jacques, T.S., et al., *Neural precursor cell chain migration and division are regulated through different beta1 integrins.* Development, 1998. **125**(16): p. 3167-77.
156. Spadari, S., F. Sala, and G. Pedrali-Noy, *Aphidicolin: a specific inhibitor of nuclear DNA replication in eukaryotes.* Trends Biochem Sci, 1982. **7**(1): p. 29-32.
157. Leach, M.K., et al., *Electrospinning fundamentals: optimizing solution and apparatus parameters.* J Vis Exp, 2011(47).
158. Leach, M.K., et al., *The culture of primary motor and sensory neurons in defined media on electrospun poly-L-lactide nanofiber scaffolds.* J Vis Exp, 2011(48).
159. Kim, B., C.M. van Golen, and E.L. Feldman, *Insulin-like growth factor-I signaling in human neuroblastoma cells.* Oncogene, 2004. **23**(1): p. 130-41.
160. Lyons, D.A., et al., *erbb3 and erbb2 are essential for schwann cell migration and myelination in zebrafish.* Curr Biol, 2005. **15**(6): p. 513-24.
161. Levi-Schaffer, F. and A. Kupietzky, *Mast cells enhance migration and proliferation of fibroblasts into an in vitro wound.* Exp Cell Res, 1990. **188**(1): p. 42-9.
162. Mehrotra, M., et al., *Differential regulation of platelet-derived growth factor stimulated migration and proliferation in osteoblastic cells.* J Cell Biochem, 2004. **93**(4): p. 741-52.
163. Muller, T., et al., *Regulation of epithelial cell migration and tumor formation by beta-catenin signaling.* Exp Cell Res, 2002. **280**(1): p. 119-33.
164. Afshari, F.T., et al., *Schwann Cell Migration is Integrin-Dependent and Inhibited by Astrocyte-Produced Aggrecan.* Glia, 2010. **58**: p. 857-869.
165. Li, S., et al., *Effects of morphological patterning on endothelial cell migration.* Biorheology, 2001. **38**(2-3): p. 101-108.
166. Corey, J.M., B.C. Wheeler, and G.J. Brewer, *Compliance of hippocampal neurons to patterned substrate networks.* J Neurosci Res, 1991. **30**(2): p. 300-7.
167. Chen, C.S., et al., *Geometric control of cell life and death.* Science, 1997. **276**(5317): p. 1425-8.
168. Maniotis, A.J., C.S. Chen, and D.E. Ingber, *Demonstration of mechanical connections between integrins cytoskeletal filaments, and nucleoplasm that stabilize nuclear structure.* Proceedings of the National Academy of Sciences of the United States of America, 1997. **94**(3): p. 849-854.
169. Ingber, D.E., *Mechanosensation through integrins: Cells act locally but think globally.* Proceedings of the National Academy of Sciences of the United States of America, 2003. **100**(4): p. 1472-1474.
170. Frostick, S., Q. Yin, and G. Kemp, *Schwann cells, neurotrophic factors, and peripheral nerve regeneration.* Microsurgery, 1998. **18**: p. 397-405.

171. Tyler, D.J. and D.M. Durand, *Chronic response of the rat sciatic nerve to the flat interface nerve electrode. .* Annals Biomed Engin, 2003. **31**(663-642).
172. Panseri, S., et al., *Electrospun micro- and nanofiber tubes for functional nervous regeneration in sciatic nerve transections.* BMC Biotechnol, 2008. **8**(1): p. 39.
173. Bini, T.B., et al., *Electrospun poly(L-lactide-co-glycolide) biodegradable polymer nanofibre tubes for peripheral nerve regeneration.* Nanotechnology, 2004. **15**(11): p. 1459-1464.
174. Aebischer, P., V. Guenard, and S. Brace, *Peripheral nerve regeneration through blind-ended semipermeable guidance channels: effect of the molecular weight cutoff.* J Neurosci, 1989. **9**(10): p. 3590-5.
175. Kobayashi, J., et al., *The effect of duration of muscle denervation on functional recovery in the rat model.* Muscle Nerve, 1997. **20**(7): p. 858-66.
176. Furey, M.J., et al., *Prolonged target deprivation reduces the capacity of injured motoneurons to regenerate. .* Neurosurgery, 2007. **60**: p. 723-733.
177. Hall, S.M., *The biology of chronically denervated Schwann cells.* Ann NY Acad Sci., 1999. **883**(215-233).
178. Li, H., G. Terenghi, and S.M. Hall, *Effects of delayed re-innervation on the expression of c-erbB receptors by chronically denervated Schwann cells in vivo.* Glia, 1997. **20**: p. 333-347.
179. Gordon, T., O. Sulaimain, and J.G. Boyd, *Experimental strategies to promote functional recovery after peripheral nerve injuries. .* J Peripher Nerv Syst., 2003. **8**(236-250).
180. Pfister, B.J., et al., *Extreme stretch growth of integrated axons.* J Neurosci, 2004. **24**(36): p. 7978-83.
181. Pfister, B.J., et al., *Stretch-grown axons retain the ability to transmit active electrical signals.* FEBS Letters, 2006. **580**: p. 3525-3531.
182. Iwata, A., et al., *Long-Term Survival and Outgrowth of Mechanically Engineered Nervous Tissue Constructs Implanted Into Spinal Cord Lesions.* Tissue Engineering, 2006. **12**(1): p. 101-110.